THE UNIVERSITY OF CHICAGO

QUANTUM MANY-BODY PHYSICS WITH PHOTONS

A DISSERTATION SUBMITTED TO
THE FACULTY OF THE DIVISION OF THE PHYSICAL SCIENCES
IN CANDIDACY FOR THE DEGREE OF
DOCTOR OF PHILOSOPHY

DEPARTMENT OF PHYSICS

BY
NINGYUAN JIA

CHICAGO, ILLINOIS
AUGUST 2018

To my parents

TABLE OF CONTENTS

LIST OF FIGURES vi

ACKNOWLEDGMENTS vii

ABSTRACT ix

1 INTRODUCTION 1
- 1.1 Synthetic Materials with Photons 2
- 1.2 Thesis Layout 3

2 EXPERIMENTAL SETUP 5
- 2.1 Vacuum System 6
- 2.2 Lasers and Locking 7
  - 2.2.1 Magneto-Optical Trap 7
  - 2.2.2 Optical Lattices 8
  - 2.2.3 Cavity Probe and Locking 9
  - 2.2.4 Rydberg Excitation Laser 9
- 2.3 Atomic Sample Preperation 10
- 2.4 The Optical Resonator 11
  - 2.4.1 Achieving a Small Waist 11
  - 2.4.2 Electric Field Control 13
- 2.5 Longitudinal Confinement of the Polaritons: Slicing 15

3 CAVITY RYDBERG POLARITONS 18
- 3.1 Dark Polaritons 19
  - 3.1.1 Hamiltonian and Dark State Solution 21
  - 3.1.2 Rotation Angle 22
  - 3.1.3 Spectroscopy of Polaritons 23
  - 3.1.4 Measuring the Dark-State Rotation Angle 26
- 3.2 Decoherence 29
  - 3.2.1 Homogeneous Decoherence 29
  - 3.2.2 Inhomogeneous Decoherence 30
- 3.3 Slow Dynamics 32

4 STRONGLY INTERACTING PHOTON 36
- 4.1 Figure of Merit of the Interaction 37
  - 4.1.1 Polariton-Confinement Collisions 37
  - 4.1.2 Polariton-Polariton Collisions 38
- 4.2 Cavity Details 40
- 4.3 Mean-Field Interaction 41
  - 4.3.1 Non-Linear Spectrum 44
- 4.4 Blockade Transmission 44

4.4.1 Strong Interaction and Photon Anti-Bunching . . . 44
4.4.2 Measuring the Photon Statistics . . . 46
4.4.3 Observation of Photon Anti-Bunching . . . 50
4.5 Time Dynamics . . . 52
4.5.1 Pulse Probe of the Cavity . . . 52
4.5.2 Rabi Oscillation of Dark Polariton . . . 54
4.5.3 Isolate the Dark Polariton Dynamics . . . 55

5 TOPOLOGICAL INSULATING CIRCUIT . . . 59
5.1 From Harper-Hofstadter to Lattice Spin-Hall . . . 60
5.1.1 The Harper-Hofstadter Model, and Breaking Time-Reversal Symmetry 60
5.1.2 Using Spin-Orbit coupling to recover Time-Reversal Symmetry . . . 62
5.2 Topological Band Theory of Circuits . . . 63
5.2.1 Dispersion Relation of 1D Transmission Line . . . 63
5.3 Braiding the Gauge Field . . . 66
5.3.1 Recap on Geometric Phase: Aharonov–Bohm effect . . . 66
5.3.2 Adding the Spin Degree of Freedom . . . 68
5.3.3 Braiding the Topology . . . 69
5.3.4 Band Structure . . . 70
5.4 Making and Probing the Metamaterial . . . 74
5.5 Characeterizing the Metamaterial . . . 76
5.5.1 Bulk and Edge excitation . . . 76
5.6 Topologically Protected Edge Propagation . . . 77
5.6.1 Spin Resolved Pulse Measurement . . . 77
5.6.2 Topologically Protected Edge Propagation . . . 77

6 BREAKING TIME REVERSAL SYMMETRY . . . 79
6.1 Symmetries in a Twisted Cavity . . . 80
6.2 A Narrow Band Optical Isolator . . . 82
6.2.1 Experimental Setup . . . 82
6.2.2 Optical Pumping . . . 82
6.2.3 Spectroscopty . . . 84
6.2.4 Figure of Merit of the Isolator . . . 88
6.3 TRS Breaking for Dark Polaritons . . . 90

REFERENCES . . . 94

LIST OF FIGURES

2.1 Vacuum System . . . 7
2.2 Electric Field Controlling . . . 14
2.3 Slice-Probe Sequence . . . 16

3.1 Relavent States for Cavity Rydberg EIT . . . 20
3.2 Spectrum of Cavity Rydberg Polaritons . . . 25
3.3 Spectroscopy of Cavity Rydberg Polaritons . . . 27
3.4 Collective Suppression of Decoherence . . . 33
3.5 Rydberg Polaritons in Two Cavity Modes . . . 34

4.1 Interaction Induced Loss . . . 38
4.2 Cavity Details . . . 42
4.3 Nonlinear Spectroscopy of a Polaritonic Quantum Dot . . . 43
4.4 Transport Blockade of Cavity Rydberg Polaritons . . . 51
4.5 Ringdown Count Arrival Histogram . . . 53
4.6 Dynamical Evolution of a Polaritonic Quantum Dot: Ring-up and Ring-down . . . 56

5.1 Hofstader's Butterfly and Chern Insulator . . . 61
5.2 Lumped Element Model for Transmission Line . . . 64
5.3 A 2D Symmetric Circuit . . . 67
5.4 Adding Spin Degrees of Freedom . . . 69
5.5 Circuit Topological Insulator . . . 71
5.6 Site-Resolved Measurement of Band-Structure and DOS . . . 72
5.7 Time-Resolved Transport Dynamics of the Edge Modes . . . 78

6.1 T-Breaking in Twisted Resonators Coupled to Atoms . . . 81
6.2 Optical Pumping . . . 83
6.3 Theory Spectrum of Time Reversal Breaking Cavity Transmission . . . 85
6.4 Spectroscopy of a Time Reversal Broken Twisted Optical Resonator . . . 87
6.5 Time Reversal Breaking in Cavity Rydberg EIT . . . 92

ACKNOWLEDGMENTS

There is a long list of people I would like to offer my great thankfulness for making the past few years a fantastic adventure in physics as well as a joyful journey to a physicist.

I would like to thank my research advisor, Prof. Jon Simon, without whom none of these works could have happened. Jon is a brilliant physicist, and it is always a great chance to gain intuition about physics by brainstorming with him. He is also a great mentor for the students. I cannot remember how many times he was willing to sit down and solve the problem with us at the early age of the lab, and through that process, I learned how to setup an experiment step by step. It has been a great honor to be working with him and motivated by his talent and enthusiasm to physics.

Ariel Sommer joined the lab as postdoctoral researcher since the first year of the new lab. Ariel has a very different style from Jon. Instead of being a quick speaker, Ariel tends to think very carefully before speak out his idea which is extremely deep and tremendous detailed. By working with him, I truly learned how to solve an hard theory or experiment problem from the very beginning, and gradually and systematically approach the answer through dealing with small parts.

Logan W. Clark join the lab in the last year of Ph.D. program. Though he never worked in a similar experiment, he catch the key ideas and experimental technique in a very short period and then quickly take the lead of Floquet polariton experiment. His ability of grasping the key physics in the experiment and asking deep questions set another great model of how a postdoctoral researcher.

Since we started with an empty lab and had to build the whole experiment from the ground, there would be no science without my lab mates. Alex Georgakopoulos is a very efficient person. He designed and built the vacuum system, and provided a lot of theoretical calculation which is crucial for explaining the experiment result. Albert Ryou is working in a quite a different style with a great carefulness. He is also extremely diligent, and it was

him who first push the boundaries of cavity design for studying Rydberg physics. It was a great pleasure to work with them and build this awesome machine.

Nathan Shcine joined the lab in the second year and quickly showed his talent by demonstrating exotic physics in the non-planar cavity. Further, he designed the second and third generation cavities for realizing the quantum dot and the future Laughlin state. The effort and intellectual ingenuity he put into those projects was truly impressive. Also, he is a great in communicating with other group members and come up with clever solutions. There were many times he helped me cleared my thought in a really chaotic situation.

I would also like to thank other group members, Clai Owens, Mark Stone, Aziza Suleymanzade, Claire Baum, and Tianxing Zheng. Clai kept working on the lattice model and improve the system so that it is now compatible with strong interaction for microwave photons. Mark and Aziza are working on a different project, but they always ask good questions during the group meeting. It is not uncommon that we came up with new ideas or gain more physical intuitions by answering those questions. Claire and Tianxing are the newly joined graduate students and already helping in building the new experiments.

Finally, I will thank my parents who their unconditioned support. Getting a Ph.D. is really a long journey, and sometimes I become depressed and begin to doubt my ability or choices, it was my parents who helped me rebuilding the confidence and regain the strong motivation. I would also like to thank my girlfriend Lu Chen for being so considerate and supportive.

ABSTRACT

Understanding and manipulating quantum materials is a long-sought goal in both the condensed matter and cold atom communities. Photons have recently emerged as a good candidate for studying quantum many-body states due to their fast dynamics and convenient manipulation. Tremendous efforts have been made to engineer single particle Hamiltonian with non-trivial topology. Having individual photons to strongly collide with each other and form an entangled many-body state remained as a challenge in optical domain.

In this thesis, I will first demonstrate how to engineer artificial magnetic field and non-trivial topology for microwave photons. In a classical lumped element circuit, we demonstrate the edge modes for microwave photons within the bulk band, and also show that these modes propagates with topological protection against the local lattice disorder. This work paves the way to synthesize correlated quantum materials in a lattice using microwave photons, combined with circuit QED technique.

Recently, Rydberg-Rydberg interaction has been broadly used in cold atom experiment to generate long-range inter-particle coupling for quantum information processing and quantum material simulation. We combine this technique with cavity electromagnetically induced transparency and create a robust quasi-particle, cavity Rydberg polaritons, which harness the power from both cavity photons with exotic topology and Rydberg atoms with strong interactions. We first demonstrate the interaction in the single quanta level in a quantum dot with single cavity mode and further expand it into multi-mode regime with modulated atomic states.

CHAPTER 1

INTRODUCTION

Throughout the history, physicists are trying to understand the macroscopic world by dividing it into smaller pieces with a simple but universal model. This approach has been a great success particularly with the discovery of the standard model that describes the properties of elementary particles with extremely high precision. Although we have learned that the whole world is built upon a few kinds of particles, explaining the fruitfulness of different phase of matter in the real world requires the knowledge beyond properties of its constituents, but rather how each individual particles interact with each other and form a matter in a collective way. The effect of interactions in forming ordered phases was first taken care of using the famous mean-field theory in which a coarse grained interaction is used to modify the free particle Hamiltonian. Furthermore, it is proposed by Landau that all phase transition can be associated with a symmetry-breaking process.

This picture holds for almost all the phase transition from solid-liquid to magnetic transition. However, the discovery of fractional quantum effect did not follow the nice pattern by preserving all symmetries we have ever known. It is later discovered that aside from the symmetry, solid state systems also have a global property that can only be describe by its topological structure. This triggers a lot of experimental and theoretical works trying to discover and explain different type of topological states. Despite its success in discovering the exotic states, it is found to be rather challenging for a solid state material to bridge the gap between the macroscopic properties and a proposed microscopic model due to the difficulty in probing individual electrons with high spatial and timing resolutions.

With the great technical advance of cold atom physics in recent years, simulating a condensed matter system with a cold atom counter part becomes realistic. In such a system, electrons in ionic lattice are mimicked by atoms in an optical lattice. Due to its large system size and particle mass, the dynamical speed is slowed down dramatically and imaging

with resolution comparable to the lattice spacing has been achieved, so that microscopic measurements have been performed for varies platforms.

1.1 Synthetic Materials with Photons

In this thesis, I will demonstrate anther approach to make a meta-material with topological order using photons. Before, photons are not considered as a candidate for forming a material since they are massless and thus cannot be trapped. However, high quality resonators in both optical and microwave frequencies provide a different view of cooling and trapping photon. In a cavity, the photons are still travelling at the speed of light but is confined spatially due to the boundary condition. This resonator based system can then be mapped on to the tight-binding model of a solid state system. Recent efforts in generating the artificial magnetic field in varies platforms also open the door for investigating the topological properties of photonic materials.

To date, even the single photon Hamiltonian has been engineered with great flexibility, the key ingredient for realizing a topological order state-strong interactions- is still missing. Classical optical non-linearity often relies on large number of photons, and such weak interactions are mostly described using a mean-field theory. To get a fully entangled system, the interaction energy is required to be much larger than the particle lifetime. This condition can be fulfilled in a a cold atoms system with a Bose-Einstein condensate (BEC) where the lifetime is on the order of seconds, and S-wave scattering ($\sim$100 Hz) or Feshbach interaction is large enough.

For photons, large non-linearity is hard since the intrinsic cross section of photons are negligible at the energy scale we consider. Hence we have to harness the power from atomic medium that is strongly couple to photons. To reach single photon level interaction, a general idea in quantum mechanics is to couple the photon field with a single two level emitter which saturates at one incoming photon. Even though the requirement of manipulating photons

and atoms on a single particle level, this effect was successfully demonstrated in Kimble's group [1], and spurred an outpouring of theoretical work exploring Hubbard physics in coupled nonlinear resonators [2–5], but the severe technical challenges associated with the deterministic preparation of individual atoms in resonator arrays remain.

In this thesis, I will show our pioneer work in a new approach combining Rydberg EIT and optical resonators [6], which benefits from the best aspects of each previous approach: the resonator enhances the light-matter coupling and allows us to work at substantially lower atomic densities while maintaining a high optical depth, while the Rydberg EIT allows the thermal cloud to be treated as a single two level "super atom".

1.2 Thesis Layout

Using photons to make material is a relatively new idea and efforts are made both in the optical domain as well as in the microwave domain. Quite different techniques are used to generate the two in gradients of a topological ordered phase: artificial magnetic (gauge) field, and strong interactions. This thesis will mainly focus on how to generate strong interaction between optical photons using Rydberg-Rydberg interaction.

Since strongly photon-photon interaction mediated by Rydberg atoms are new frontiers in the cold atom community, and its application with a cavity quantum electrodynamics (cQED) system has not been explored before, I will introduce our experiment setup in chapter 2 and try to explain some of the philosophy in making such system. Chapter 3 is some information about the general properties of a cavity Rydberg polariton, followed by chapter 4 in which we enter the strong interaction regime and demonstrate the ability of making a polaritonic quantum dot. I will also discuss the figure of merit of the dot which is crucial in using the dot for quantum information processing (QIP).

Microwave photons are also good candidate for investigating many-body physics in a lattice system. Generating synthetic magnetic field and interaction in such platform requires

a different technique. In chapter 5 I will discuss how to engineer the artificial gauge field in a lumped element circuit.

CHAPTER 2

EXPERIMENTAL SETUP

In this chapter, I will introduce our road map in building the experiment suitable for investigating topological quantum many-body physics with photons. In the previous chapter, I have introduced the idea of using non-planar cavity to create a flat transverse space with non-trivial topological structure for photons to live in and exhibit exotic properties. This already makes the design process of a cavity much more complicated even without considering the atoms. Furthermore, since the Rydberg atoms used to mediate strong repulsive interactions between photons are extremely fragile and sensitive to the external ambient environment, so extra constraints are needed to prevent the decohence of the quasi-particle.

Although making a cavity suitable for photonic many-body states is challenging, we do benefit from the fast dynamics speed of using photons as the constituents of our metamaterial. Comparing to the lifetime (seconds) and S-wave interaction energy ($\sim$100 Hz) of a neutral atoms in optical lattice, the lifetime of the Rydberg polaritons observed in this thesis is about 100 kHz with room to improve in the future, and the effective interaction energy [7] between two polaritons is in the MHz range. So the dynamics is happening within hundreds of nanoseconds, which is much shorter than the quasi-particle lifetime as well as the Doppler time scale of an atomic cloud even without a Bose-Einstein Condensate. As a result, we put a relatively low requirement for the vacuum level comparing to a quantum gas experiment, which reduces the complexity of vacuum chamber. Also, the sample preparation process can also be sped up since evaporative cooling is not mandatory. This dramatically increase the repetition rate of our experiment which is crucial in trying to detect few photons states.

The chapter will be split into five main parts: vacuum system, laser system, cavity, sample preparation, and longitudinal slicing. Among all the sub-systems, I will mainly focus on the design philosophy of the optical cavity and the longitudinal slicing process. Even though an optical cavities have been widely used in the cold atom community, particularly

the cavity QED experiments, having them couple to Rydberg excitation while maintaining strong coupling remains as an unexplored regime. We went through couple design iterations to overcome or bypass variety of challenges before the polariton behaving properly for strong interactions. The slicing technique is invented to shrink the size of the atomic cloud along the cavity axis. This could be done with a high resolution imaging system that is pretty common in quantum gas experiment. However, due to the chamber geometry, we do not have enough numerical aperture to achieve the resolution needed for the small size. Instead, we employ a super-resolution imaging scheme using the saturation effect, and successfully confine the cloud size well below the diffraction limit.

2.1 Vacuum System

Usually, an extremely high vacuum is required in quantum gas experiment since it the lifetime, which must be significantly larger than the inverse of interaction energy, strongly depends on the background pressure. In our experiment, the Rydberg mediated interaction between photons is much faster than the S-wave scattering of ground state atoms, and a typical experiment probe time ranges from 1 to 10 ms, in which hundreds of dynamic cycle could be finished. Hitherto we can tolerate a much higher background pressure with a rather simple vacuum system.

A schematic of the chamber is shown in Fig. 2.1. The main part of the chamber has two 12 inches windows for horizontal MOT beam and input/output beam of the optical cavity. Two diagonal MOT beams are sent in and retro-reflected through four 2 inch windows on the top(bottom)-right(left) of the chamber. Another two 2 inch windows in the vertical direction are used for the optical lattice and other lasers for manipulating the atoms in the resonator since the cavity is mounted higher than the middle of the chamber so optical access from the side is very limited. The remaining horizontal ports are connected to two crosses used as path to ion gauge/pump and gate valve, as well as feed-throughs for the electric wiring.

Figure 2.1: **Vacuum System**

Two 2 inch windows are used at the end of the two crosses so that we have a imaging path looking at the atoms at the MOT location.

In order to control the electric field condition of the Rydberg atoms, an active field control filter with 8 electrode is required, and thus we need a lot more electric connections than most of the experiments with neutral atoms. A custom order top flange with four external tubes welded to the neck is used for connecting to the cavity with 2 15 pins D-sub and 2 25 pins D-sub connectors. The wires are hooked up to a terminal block for easy assembling.

2.2 Lasers and Locking

2.2.1 Magneto-Optical Trap

The laser system of the magneto-optical trap (MOT) consists of three lasers and a tappered laser amplifier. The frequency reference laser (master) is made of a distributed feedback (DFB) laser diode with a home build mount with fast feedback capability. The laser is lock to an enriched Rubidium vapor cell on the $F = 2 \rightarrow 2'$ and $F = 2 \rightarrow 3'$ cross over point

using Doppler free spectroscopy. The MOT and repumper laser are then locked to the master laser using beat note locking technique. The local oscillator controlled by a direct digital synthesizer (DDS) is introduced to shift the locking frequency and quickly tune the laser during the experiment. The reason that a helical resonator (instead of a delay line) is used to do the frequency-to-voltage conversion is to compress the error signal in the frequency axis so that any drift in error offset would not result in a large frequency shift. However, this put a challenge for the fast tuning of the laser since a small movement in the locking frequency can unlock the laser. So the error signal, after properly filtered and amplified, is also directly injected into the laser diode current port to perform the fast changing of frequency. Most of the power coming out of the MOT laser is then sent into a fiber coupled tappered amplifier with a free space outputs of about 1 W. This high power beam is combined with the repumper laser on a 50:50 cube, and then fiber coupled into two single mode fibers used for the horizontal and diagonal beam for the MOT. Both the horizontal and diagonal beams, after the fiber, have a $1/e$ diameter of 1 inch.

2.2.2 Optical Lattices

The optical lattice is used to trap the atoms after the polarization gradient cooling (PGC) and later transport them into the waist of the optical resonator. Since the total experiment time is much shorter than a second and the total scattering of lattice photon off the cloud is not a big concern, we use laser that is 4 nm detuned from the Rubidium $D2$ line transition with $\sim$700 mW of power coming out of a tappered amplifier. The amplifier is seeded by a DFB laser locked to a stable cavity with Pound–Drever–Hall scheme. There are two main reasons that this far detuned laser needs to be locks: (1) Within the wavelength the laser can drift, there are multiple photo-association lines that will cause loss of atoms; (2) A DFB diode typically have a linewidth of $\sim$MHz which dramatically increase the parametric heating of the cloud, so a fast feedback is needed to electronically narrow the laser. In experiment,

we can observe factor of 2 increase in atom number after the laser is properly locked. Due to the high power, the beam is coupled into a photonic crystal fiber in order to prevent the non-linear effect, and a interference filter is used after the fiber to further clean the 780 nm photons generated by the fiber non-linearity. After going through the chamber, the beam is retro-reflected, forming a lattice.

2.2.3 Cavity Probe and Locking

The Rydberg polariton has a much longer lifetime and narrower spectral width than the cavity and the excited atoms, so to avoid induced decoherence by the probe light, the linewidth of laser is required to be much smaller. We start with a virtual ring cavity laser with 1560 nm which is seeding a NUFERN fiber amplifier to boost the power up to 10 W (2.5 W used in daily usage). A periodic-poled-Lithium-Niobate (PPLN) crystal is used in a single pass configuration to generate 780 nm photons through frequency doubling. Before coupled into the cavity, the beam is sent through a fiber coupled electro-optical modulator (EOM) with RF frequency controlled by a DDS channel to generate sideband at frequency range from 1 MHz to 2.5 GHz. The laser is locked to a ultra-stable cavity with a PDH setup. Sideband are also generated by using a EOM for the locking beam, and by locking the sideband to the cavity, the locking point can be tuned by changing the sideband frequency.

2.2.4 Rydberg Excitation Laser

To excite the atoms to a Rydberg state through a two photon transition, we use a TOPTICA TA-SHG-PRO 480 nm laser with 450 mW of output power to couple the excited state of the atom to a Rydberg state. The 960 nm beam before the second harmonic generation stage is also locked to the ultra-stable cavity using the same technique as the probe laser. A 200 MHz AOM is used to turn on/off the laser. The beam is then send into the cavity through the bottom mirror which has high transmission at 480 nm. The intensity profile of

the blue laser will generate inhomogeneous decoherence of the polariton, so the beam has a waist inside the cavity of $\sim$45 μm, much bigger than the cavity waist 12 μm.

To make sure the blue beam is counter propagating with the cavity mode, we initially align the beam with the leakage of cavity mode through the bottom mirror. Once the EIT signal shows up in the spectrum, the fine adjustment can be done by optimizing the EIT peak height. During the daily operation, we sometimes have to turn the wavelength of the blue laser in order to couple to different Rydberg state. A camera focusing at the cavity waist is then used to help us preserving the alignment at the atomic cloud.

2.3 Atomic Sample Preperation

Since a BEC is not required for the Rydberg poalriton experiment and an atomic cloud with temperature of $\sim$10 μK can then be considered as a frozen cloud within the time scale of polariton dynamics. A more detailed discussion on the residual Doppler can be found in [7]. The non-zero temperature mainly limits the probing time because of the expansion of the cloud reduce the peak atomic density, and this could be compensated by applying a magic wavelength trap. As a result, the sample preparation process is rather simple with a standard MOT followed by a PGC.

A standard six beam MOT (three retro-reflected 1 inch beams) is used in our experiment. The cooling lasers runs on the ^{87}Rb D_2 line $\left|5^2S_{1/2}\right\rangle \rightarrow \left|5^2P_{3/2}\right\rangle$ at 780nm. The cooling laser is 23 MHz red detuned from the $\left|F_g = 2\right\rangle \rightarrow |F_e = 3\rangle$ transition with a power of 1 mW. The detuning is optimized by maximizing the atom number in the optical resonator, and is larger than the twice the atmic linewidth (Γ=2π $\times$ 6MHz steck2001rubidium) due to the broad linewidth of the DFB diode. The atoms can off resonantly scatter from the $\left|F_g = 2\right\rangle \rightarrow |F_e = 2\rangle$ transition and fall into the $\left|F_g = 1\right\rangle$ ground state. Hence a repumper laser driving the $\left|F_g = 1\right\rangle \rightarrow |F_e = 2\rangle$ transition is combined with cooling laser before the fiber to repump the atoms back into the $\left|F_g = 2\right\rangle$ state. The atom number is insensitive to

the power and detuning of the repumper laser once it can repump all the atoms in the dark hyperfine state. Two in vacuum magnetic coils with anti-Helmholtz configuration produce a field gradient of 21.8 G/cm at the center of the MOT.

After the loading of the MOT, we turn off the magnetic coil and lasers and ramp the detuning of the cooling laser to ∼200 MHz to perform a polarization gradient cooling. Three pairs of bias coil is used to zero the magnetic field at the atomic cloud. After the frequency and magnetic field ramping, the cooling and repumping laser is kept on for another 10 μs, reducing the cloud temperature to about 15 μK.

A vertical optical lattice formed by retro-reflecting a 784 nm beam is kept on during the whole PGC process and about 30% of the atoms are loaded into the lattice after the cooling. The lattice has a beam size of ∼85 μm at the MOT and ∼70 μm at the cavity waist. To transport the atoms in to the cavity, two acoustic-optical modulators are used to shift the frequency of the reflecting beam with a cat's eye setup at the retro-reflection path. The atoms are moved up into the optical resonator by detuning the retro-reflected lattice beam by 10 MHz corresponding to a speed of 3.9 m/s with maximum acceleration of 100 g (∼1,000 m/s^2). A sample with ∼1000 atoms is prepared in the optical resonator after the transport with a RMS size of 40 μm.

2.4 The Optical Resonator

2.4.1 Achieving a Small Waist

In order to reach the strong interaction regime, the polaritons have to be confined within one blockade volume, i.e., the volume of the cross-section between the atomic cloud and the cavity mode must be less than ∼10^3 μm^3 in our experiment. The longitudinal and transverse confinement is realized through slicing (see section 2.5) and small cavity waist respectively. Designing a two mirror cavity with such a small waist is a somewhat challenge due to the

diffraction limit which then requires either a large mirror curvature or a long cavity with big mirrors. This can be seen by thinking of a 1:1 imaging system with two identical lenses: a short focal length does not require a aperture of the lens but a large curvature, while a long focal length mirror must have a bigger diameter in order to have the same numerical aperture.

The Rydberg atoms are extremely sensitive to stray electric field which can be created by electric charges built up on the dielectric surface of the mirrors. This effect might be compensated by carefully engineered cavity symmetry or active electric field control. However, both of them will have a great design constraint and also dramatically complicate the whole system. Here, we overcome this difficulty by employing a four mirror cavity with a bow-tie configuration where the two upper mirrors have almost flat curvature that allows the mode to expand and have a large mode waist at the lower mirrors. Having a longer upper arm, however, was unacceptable for two reasons: First, the resonator linewidth would decrease (at constant finesse), which proportionally decreases the data collection rate. Second, the resonator is loaded into our vacuum chamber through a 62 mm diameter tube, which therefore sets an absolute maximum exterior size. Both of these limitations could be avoided, however, by utilizing convex mirrors in the upper arm; the defocus that they create acts, for our purposes, equivalently to diffractive expansion.

With numerical modeling, we arrived at an acceptable configuration of the resonator given these constraints, providing a $\sim 13\ \mu m$ waist at least 12 mm away from the nearest surface. To provide passive electric field attenuation, the steel mounting structure fully encloses the locking piezo, which can be driven up to 1 kV, and the front surface of every mirror is covered except for small aperture at the mode location. The resonator's upper mirrors are plano-convex with a 50 mm radius of curvature while the lower mirrors are concave with a 25 mm radius of curvature. The two upper mirrors and the non-piezo lower mirror have a custom coating provided by Layertec GmbH, specified to have a 99.9% reflectivity at both

780 nm and 1560 nm, while having >95% transmission at 480 nm. The other lower mirror has a coating by Advanced Thin Films with much higher reflectivity of 99.995%. While the optimal finesse for this resonator would be $\sim$ 2100, contamination during resonator alignment resulted in additional loss and a cavity finesse of $F = 1480(50)$. The free spectral range is 2204.6 MHz, measured with an EOM sideband, and the polarization eigenmodes are approximately linear and split by 3.6 MHz.

2.4.2 Electric Field Control

Additional to the large sample-surface distance, eight screw-head electrodes provide active electric field control, and the two separate halves of the mounting structure may each be set to an arbitrary electric potential. In total, this provides ten degrees of freedom to control the eight independent electric field and electric field gradient components. Finite element analysis based on 3D CAD designs then provide the conversion matrix between applied electrostatic potentials and the electric field and gradients at the mode waist. Since the number of electrodes exceeds the number of controlled components, we calculate and use the 'optimal' conversion matrix which minimizes the applied electric potentials. The electrode voltage is controlled by analog card from National Instrument, and a 1 kHz low pass filter is applied between the card and the electrode, removing the voltage spikes between each output sample. In reality, because of large distance between the electrodes and the cavity waist, the voltage required to apply any electric field *gradient* is beyond the capability of the analog card. But this is a good indication that all the charges or patch potential from the cavity surfaces also do not affect the gradient condition at the atomic sample. In the experiment (Fig.2.2), we can tune the field strength in all three axis and observe the quadratic response of the EIT feature with respect to the field applied which shows a good agreement with our transfer matrix.

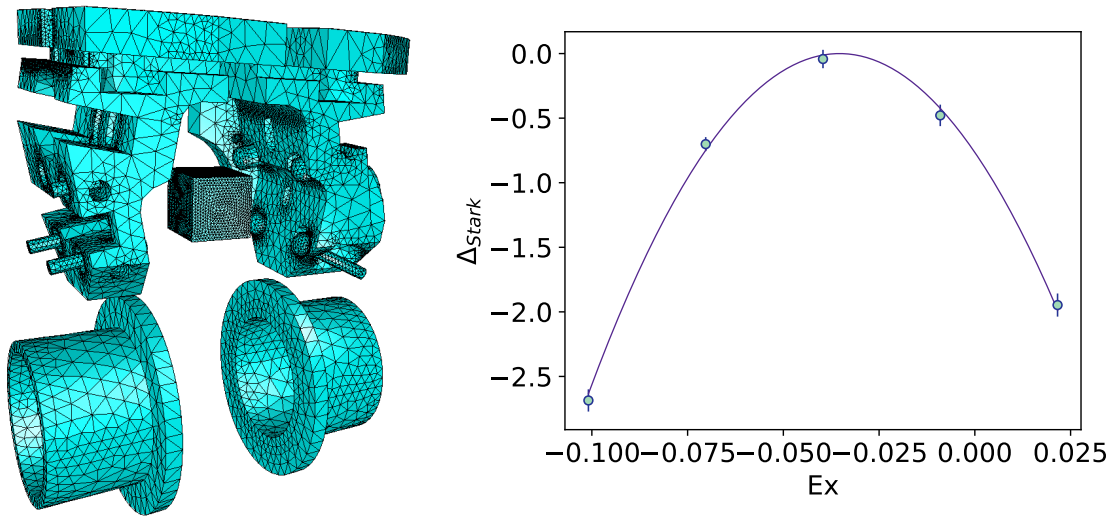

(a) (b)

Figure 2.2: **Electric Field Controlling. a** A 3D CAD .stl model generated in SolidWorks is imported into ElmerGUI finite element analysis package via the Salome mesh generation software. The steel mounting structure, eight electrodes with their macor spacers, high voltage piezo, and MOT coils are included in the model; an additional fictitious cube with a finer mesh is specified near the atom location in order to increase the precision of the result. Each insulator and conductor is assigned a permittivity or voltage boundary condition respectively, with a large bounding sphere enclosing the entire model (not shown) given an 'effective infinite' boundary condition. The electric field at the atom position is calculated with each metal body set to 0V except for one set to 1V, and a python script then iterates over which metal body is set to 1 V. The results provide a matrix converting electrode potentials to electric field at the atoms. This may then be inverted and used in the experimental control apparatus to convert a desired electric field (or gradient) into applied voltages. **b** We purposefully apply an electric field along specific axis defined by the cavity geometry using the transfer matrix, and observe the energy shift of the polariton due to the DC stark shift. By fitting the EIT peak with a Lorentzian function, we extract the amplitude of the shift vs electric field applied. The result shows a good agreement with quadratic form of DC stark effect (solid curve in **b**) up to an overall factor of the polarizability. The applied field does not increase the linewidth of the dark polariton, indicating a good orthogonality between field and field gradient control.

2.5 Longitudinal Confinement of the Polaritons: Slicing

The polaritons are further confined along the cavity axis by reducing the atomic sample size in the longitudinal direction through a spatial selective depump process. The original cloud moved into the cavity has dimensions of 35μm which is much larger than the Rydberg blockade radius. To reduce the longitudinal extent of the cloud, we first shine a large global depump beam (Fig. 2.3a) with a waist size of 500 μm. The laser is on resonance with the $|F = 2\rangle \rightarrow \left|F' = 2\right\rangle$ transition and depumps all of the atoms into the $|F = 1\rangle$ ground state. A vertical local repump beam (Fig. 2.3b) tuned to the $|F = 1\rangle \rightarrow \left|F' = 2\right\rangle$ transition is then switched on for 2 μs. The beam is narrow in the cavity axis in order to repump only the atoms in the center of the cloud. Finally, another slicing beam with a TEM_{10}-like beam profile (Fig. 2.3c) is turned on and tuned to $|F = 2\rangle \rightarrow \left|F' = 2\right\rangle$ transition. The node of the mode is aligned to the center of the cloud which coincides with the cavity waist. After the final slicing, the longitudinal size of the atomic cloud is reduced to $\sim$10 μm. The probe and control beams are then turned on after the slicing. To avoid creating shelved Rydberg atoms, a 10 μs gap time is set between the slicing and probing processes.

During the 1 ms probe time, 10 slice-probe cycles are implemented to maintain the confinement of the atomic cloud. The lattice is turned off throughout the process (primarily to avoid broadening of the Rydberg level), and thus the location and size of the cloud change due to gravity and finite temperature. The free fall limits the total probe time to less than 1.5 ms, during which time the cloud falls by 11.5 μm; within this same interval the cloud also expands to $\sim$100 μm, larger than the slicing beam. As such, a global depump is performed at the beginning of each slicing sequence to remove all of the atoms in the tails, as they would not be depumped effectively by the slicing beam. To maintain constant atom number in the sliced cloud over all 10 slicing cycles in spite of cloud expansion, we repump more weakly in first cycle, and increasingly strongly over subsequent cycles. In so doing we trade-in peak density for atom number uniformity.

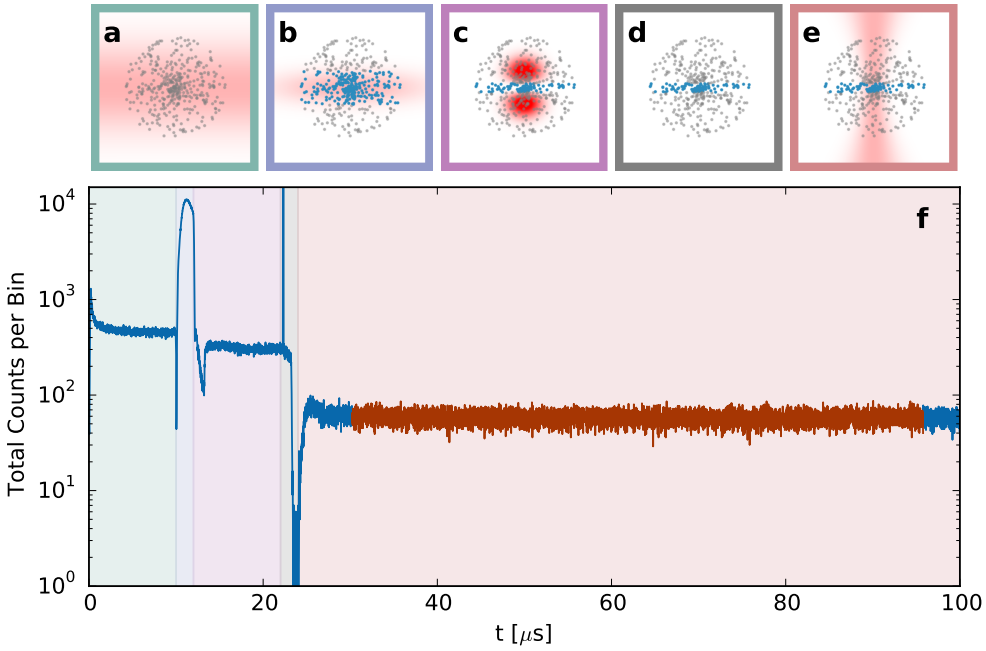

Figure 2.3: **Slice-probe sequence beam setup and histogram of single photon events for the g_2 measurement. (a-e)** shows the beam setup and the atomic state of one slice-probe cycle. The atoms color coded with blue are in the $|F = 2\rangle$ ground state, and those in gray are depumped to $|F = 1\rangle$ ground state. The histogram of photons detected by the single photon counter is shown in **f**. The events colored in red are used to obtain the time correlation. To obtain the ring down measurement, we turn on and off the probe beam 8 times during the probe stage (red background).

It bears mentioning that the magnetic field is zeroed at the cavity waist in order to minimize the dark-polariton linewidth, without necessitating optical pumping into a single Zeeman sublevel m_F. The $|F = 2\rangle \rightarrow \left|F' = 2\right\rangle$ beams will thus optically pump some of the atoms into a dark state before depumping them to the $|F = 1\rangle$ ground state. To remove this dark-state, the global depumping beam is sent through an electro-optical modulator (EOM) with the polarization 45° off of the EOM axis; the EOM is then driven at a frequency of $2\pi \times 390$kHz, producing polarization modulation of the output light. Unfortunately this method is inapplicable to the slicing beam, because it passes through a polarizing beam splitter downstream in the optical path. To rotate the atoms out of the dark state in the slicing process, a weak polarization scrambling beam on $|F = 2\rangle \rightarrow \left|F' = 3\right\rangle$ transition with linear polarization is applied along with the slicing beam.

The cavity mode overlaps with the lattice beam at three points (lower waist, upper waist, and the crossing point). If a fraction of the transported atomic cloud is improperly decelerated, it can transit the crossing point or the upper waist. This sub-sample will behave as an absorbing medium, broadening the EIT feature and destroying the blockade effect. To remove these residual atoms, a "blasting" beam from the side which is tuned to $|F = 2\rangle \rightarrow \left|F' = 3\right\rangle$ is aligned between the lower waist and the crossing point. The power of this beam is set to push the atoms away before they reach the crossing point.

CHAPTER 3

CAVITY RYDBERG POLARITONS

Polaritons, photon like quasi-particles, have became an appealing platform for studying both quantum information processing and many-body physics since it harnesses the power from both the fast dynamics from photon and non-linearity from atomic or dipole-carrying excitation. Examples ranges exciton polaritons in semiconductor microcavities [8–10], whose mass and trapping arise from a photonic component, and mean-field interactions from an excitonic component; magnon-polaritons [11–13], providing long-lived storage of quantum information in a collective atomic hyperfine excitation, and efficient transmission due to strong coupling to a quantized optical mode; and surface plasmon polaritons [14], where the photonic component provides tight confinement, and thus strong interactions due to hybridization with a single emitter.

Among all the platforms, the Rydberg polariton [15–25] is an emerging tool; its Rydberg component provides interactions that are strong at the single-quantum level, enabling single-photon transistors for quantum information processing [26–28], while its photonic component allows interfacing to quantum communication channels [29]. While these particles have been primarily studied in free-space, trapping the photonic component in an optical resonator enhances interactions between polaritons [20, 30], and promises exquisite control of the polariton dispersion [31] necessary to induce photonic BECs [32], emergent crystallinity [33–37], and the synthetic magnetic fields [33, 38–40] essential for topological fluids [33, 39–42].

In this chapter, we definitively observe the cavity Rydberg polariton, and then systematically study its coherence properties that apply to all cavity dark polaritons. We first explore the dark-polariton spectrum, demonstrating compression compared with that of the bare cavity field corresponding to a slowdown of dynamics; we investigate the available dynamical bandwidth for many-body physics or quantum information processing (QIP) as a function of atomic optical depth, finding an analogy to dark polaritons in free-space elec-

tromagnetically induced transparency (EIT); we then observe an unexpected robustness of cavity dark-polaritons to inhomogeneous broadening channels. Finally, we explore Rydberg-polariton physics in a multimode regime with an eye towards few-particle quantum material and QIP experiments.

The text of this chapter is based on the publication [43] which the author made the major contribution.

3.1 Dark Polaritons

Traditional cavity polaritons [44], comprised of cavity photons and atomic excitations, suffer from the high loss through the atomic channel that limits its application in quantum information processing. Lack of interaction between excited atoms also makes it less appealing candidate for studying many-body physics. In order to improve the lifetime of the quasi-particle, we need a both constituents of the polariton to be long lived while still maintaining the strong coupling between them. This can be achieved through the electromagnetically induced transparency (EIT). In Fig. 3.1a, we show the relevant atomic states for a typical two photon transition to the Rydberg state. The cavity is tuned to be near resonance with the ground to excited state transition: $\left|5S_{1/2}\right\rangle \rightarrow \left|5P_{3/2}\right\rangle$. A control laser will couple the low laying excited state to a highly excited Rydberg state, and when the two photon resonance condition is fulfilled, the two transition path will destructively interfere with each other, cancelling the population in the lossy intermediate state. The eigen-vectors for this 3-level Hamiltonian is plotted in Fig. 3.1b. Of the three eigen-states, the one with zero energy is purely made of a cavity photon and a Rydberg excitation and is called the dark polariton. The other two branchess are mainly consist of the cavity photon and excited state atoms, and behaves in a similar way as the vacuum Rabi peaks in a two-level Hamiltonian.

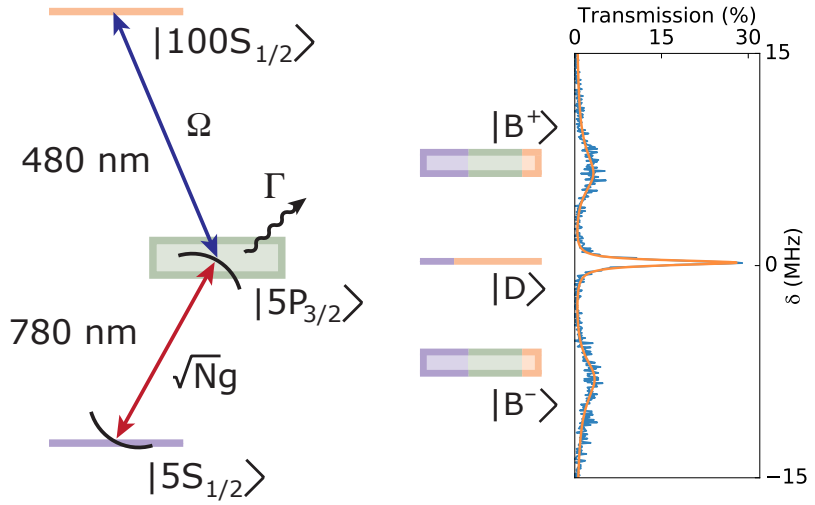

(a) (b)

Figure 3.1: **Relavent States for Cavity Rydberg EIT. (a)** Because photons do not naturally interact with one another, we employ atoms to mediate interactions.An optical resonator couples 780 nm photons (red) to a sample of $N \approx 150$ ^{87}Rb atoms, creating a collective $\sqrt{N}g$ enhancement in the single atom-photon Rabi frequency, g. A 480 nm "control" laser (blue) coherently couples excited atoms to the $n = 100$ Rydberg state with Rabi frequency Ω. Rydberg atoms interact strongly with one another, and the light-matter coupling imprints these interactions on the 780 nm photons. **(b)** When we probe the spectrum of this strongly-coupled light-matter system, we observe three distinct peaks corresponding to the three quasi-particle eigenstates, called polaritons: two broad "bright" polaritons, with a linewidth set by the excited state spontaneous decay rate Γ, and one narrow, tall "dark" polariton in the middle, with a loss rate γ_D independent of Γ. The dark polariton is the longest-lived and most Rydberg-like quasi-particle, so it provides the best platform for mediating interactions between photons.

3.1.1 Hamiltonian and Dark State Solution

The cavity photons are hybridized with the Rydberg excitation through a two-photon transition in which a cavity photon is on resonance with the ground to excitation state transition and another control field couples the atoms to the Rydberg state. The Hamiltonian for a single excitation in the cavity can be written as

$$H = H_C + H_A + H_{int}, \tag{3.1}$$

with

$$H_C = (\delta_C - i\frac{\kappa}{2}) \left|C\right\rangle \left\langle C\right| \tag{3.2}$$

$$H_A = -i\frac{\Gamma}{2} \left|E\right\rangle \left\langle E\right| + (\delta_R - i\frac{\gamma_R}{2}) \left|R\right\rangle \left\langle R\right| \tag{3.3}$$

$$H_{int} = \frac{G}{2} \left|E\right\rangle \left\langle C\right| + \frac{\Omega}{2} \left|R\right\rangle \left\langle E\right| + H.C. \tag{3.4}$$

where the three states considered here $|C\rangle$, $|E\rangle$, and $|R\rangle$ are the one cavity photon with all atoms in the ground state, no photon with collectively excited atoms, and the collective Rydberg state. The collective coupling strength between the atomic cloud and a single cavity photon is then defined as

$$G = \frac{1}{\sqrt{N_A}} \sqrt{\sum g_n^2} = \sqrt{N_A} g \tag{3.5}$$

with the assumption that all the atoms are couple to the cavity mode with uniform strength g. The square root of atom number represents the collective enhancement of the atom photon coupling. However, the second transition involves the excited state and the Rydberg state does not benefit from this collective enhancement any more since the control laser can only couple the atom in the excited state, and the density of states of the two excitation manifold are identical. One way to understand this is to use the Fermi's golden rule: the matrix elements here is well defined by the coupling between single atom and a photon, but the

density of *final* states for the ground to excitate state transition is large due to many atoms by which the photon can be absorbed, while the blue photon can only be absorbed by one atom that is in the excited state. So even there are many collective Rydberg states, each one of them is only associated with a particular excited state.

Having established the Hamiltonian, we can do a direct diagonalization and find the eigenstate for a lossless system where κ, Γ and γ_R are set to be 0. To further simplify the problem, we first consider the case with zero single photon detuning, that is $\delta_C = \delta_R = 0$. The three eigen-vectors can be written as

$$|D\rangle = \frac{\Omega}{\sqrt{\Omega^2 + G^2}} |C\rangle - \frac{G}{\sqrt{\Omega^2 + G^2}} |R\rangle \tag{3.6}$$

$$|B\pm\rangle = \frac{1}{\sqrt{2}} \left(\frac{\Omega}{\sqrt{\Omega^2 + G^2}} |C\rangle + \frac{G}{\sqrt{\Omega^2 + G^2}} |R\rangle \right) \pm \frac{1}{\sqrt{2}} |E\rangle . \tag{3.7}$$

Of the three solutions, one eigen-state, which is called the dark polariton, does not have any population in the excited state $|E\rangle$, and thus has a much longer lifetime than the other states (bright polaritons). Even though the photons are hybridized with the Rydberg excitation in all three eigen-states, the strong decoherence in the intermediate state is the dominating energy scale and prevent the particles from entangling with each other through the interaction.

3.1.2 Rotation Angle

For the rest of this thesis, we can mainly focus on the dark polariton manifold since neither the interaction energy nor the decoherence can couple the dark state to a bright one if they are energetically well resolved. This approximation is not strictly speaking true, and we will discuss the effect of the cross coupling in the later chapter. Since only the cavity photon and Rydber state are involved in the wave function, the dark polariton can be efectively

portraited as an two-level system without phase degree of freedom

$$|D\rangle = \cos\theta\,|C\rangle - \sin\theta\,|R\rangle\,, \tag{3.8}$$

where $\theta \equiv \arctan G/\Omega$ is the *dark state rotation angle* [45]. Like a typical cavity QED system described by a Jaynes-Cummings Hamiltonian, the quasi-particle can be make either more photon-like which has faster dynamics or Rydberg-like which interact with each other stronger. However, this is *not* done by detune the cavity from the two-level emitters, instead, the relative ratio of the two constituents is decided by the rotation angle which is defined with the relative coupling strength between the two transition path. Furthermore, since the excited state is adiabatically eliminated from the dark state together with the linear susceptibility, the energy of the dark polariton does not change as long as the two photon transition is maintained on resonance. The properties, for example the decoherence and resonent frequency, of the quasi-particles can also be projected from the cavity photon and the Rydberg atoms by directly applying Eq. 3.8.

3.1.3 Spectroscopy of Polaritons

Experiment Sequence

The experiment starts with the atomic sample preparation and transport described in section 2.3. After the cloud is moved into the cavity waist, we turn on the probe and blue control beam simultaneously. A DDS controlled EOM is used to create the sideband, which is tuned to be on resonance with the cavity, and the DDS frequency is swept during the probe to obtain the spectrum. A fiber coupled single-photon-counting-module (SPCM) is used to detect the photons leaking out of the cavity and the TTL signal output by the SPCM is then send into a FPGA (field programmable gate array) for recording the number of photons detected within a time bin. During the probe time, the lattice beam is turned off to avoid

inhomogeneous broadening coming from the trapping potential. For a typical spectrum probe cycle, we scan the probing sideband for about 30 to 60 MHz in a millisecond. The main limiting factor for the probe time is the thermal expansion of the cloud which reduces the atom number and thus the collective G.

Spectrum of Cavity Rydberg Polaritons

To isolate the single polariton physics, we first work with the Rydberg state at low principle quantum number ($|R\rangle = \left|40S_{1/2}\right\rangle$) where the interaction is negligible due to the small blockade volume. Fig. 3.2 shows the cavity Rydberg EIT transmission (red) normalized to the empty cavity.

The two broad peaks at approximately ± 10 MHz are the bright polaritons, and the tall narrow peak at zero detuning is the dark polariton resonance. The blue line in Fig.3.2 shows the empty cavity transmission, and since linear dispersion is cancelled, the dark polariton resonance should always be coincide the bare cavity frequency. This is actually an important criteria for deciding whether the polariton is on dark polariton resonance in the sense that the bright polaritons could be dressed by near by atomic transition (for example other hyperfine states), and the dark polariton does not necessarily reside in the middle of the two bright polariton resonances.

Also, since the polaritons now contains Rydberg excitation which has a longer lifetime than the cavity photons, its linewidth (1.3 MHz) is smaller than the empty cavity (1.8 MHz). The total transmission at the peak is also shorter due to the fact that some of the excitation is decaying through the Rydberg atoms and thus cannot be detected via a photon in the cavity mode. By decreasing the blue power, we can change the rotation angle and make the polariton less photon like, showing a even narrower linewidth and lower transmission.

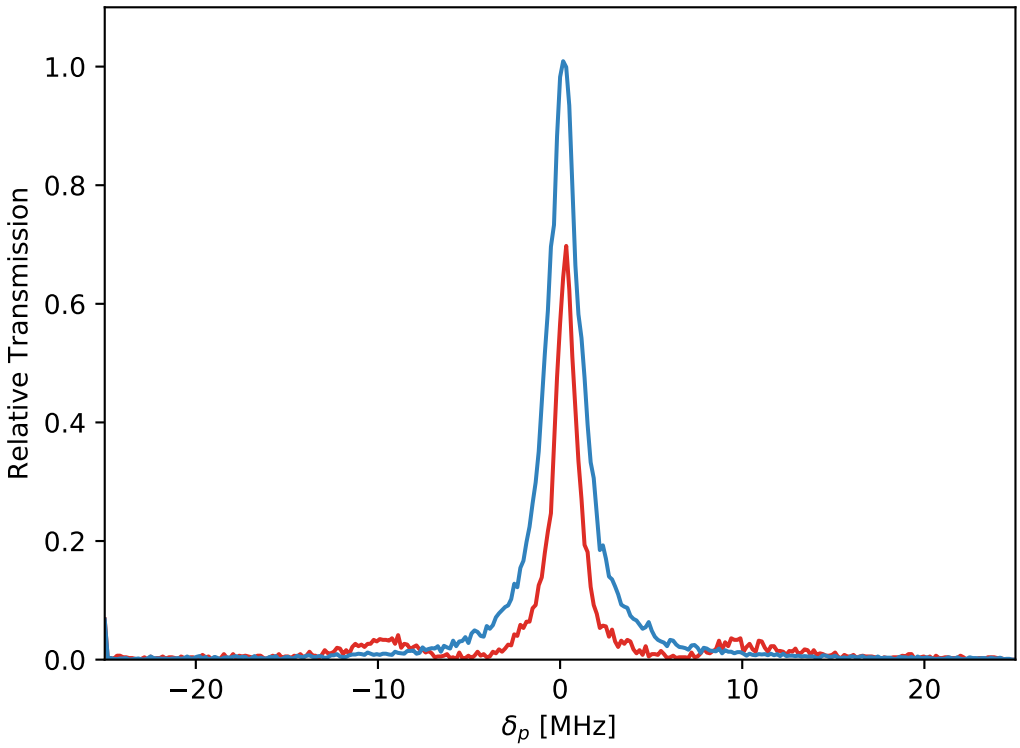

Figure 3.2: **Spectrum of Cavity Rydberg Polaritons.** The cavity transmission exhibits a EIT spectrum (red) when the atoms are moved into the waist with the control beam on. The two bright polariton peak at $\sim \pm 10$ MHz indicates the strong coupling between cavity photons and atoms. Since the linear susceptibility is cancelled by the two transition path, the dark polariton shows up at the same frequency as empty cavity peak (blue). The Rydberg excitations with longer lifetime than cavity photons are mixed with the photon, so the dark polaritons have a narrower linewidth than the bare cavity transmission. The lower transmission of the dark polariton is a result of loss throught the decay of Rydberg atoms into the vacuum.

3.1.4 Measuring the Dark-State Rotation Angle

The rotation angle can be calculated from the measured collective atom-photon coupling constant G and the control beam power Ω. We can also measure this quantity thoroughly using the resonator spectrum at different cavity detunings. According to Eq. 3.8, the energy of the dark polariton δ_D, to the lowest order, will follow the cavity detuning but at a slower rate

$$\delta_D \approx \delta_C \cos^2\theta + \delta_R \sin^\theta . \tag{3.9}$$

In Fig. 3.3, we plot the cavity transmission in the probe/cavity detuning plane (δ_p, δ_C). When the control field is turned off, the cavity-atom system is governed by the Jaynes-Cummings Hamiltonian, and the Rabi splitting appears when the cavity cross the atomic transition frequency. With the pressece of the blue laser, a EIT peak shows up at the center, and near zero cavity detuning, the energy of the dark polariton energy increase of decrease accordingly, but at an angle of $\theta/2$, not 45° representing the photon energy. We make the same measurement at several different rotation angle by changing the blue laser power in Fig. 3.3(a). For each setting, we fit the central peak with a Lorentzian and extract the peak location, the slope of the dark polariton energy is then calculated for the peaks near the zero cavity detuning. We compare the measured slope with the dark state rotation angle calculated from G and Ω, the result is plotted in Fig. 3.3(c) and shows a good agreement with theoretical prediction (solid line). At large cavity detuning, the polariton energy rolls because Eq. 3.9 fails and the polaritons are no longer "dark" any more. An intuitive picture of why the "dark" polariton energy rolls over is at sufficiently large detuning, the strongly couple manifold is the excited and Rydberg states, and when the cavity photon is on resonance with $|E\rangle \pm |R\rangle$, avoid crossing shows up at $\pm\omega/2$.

Experiments begin with a laser-cooled ^{87}Rb atomic sample that we optically transport into the waist of a running-wave bow-tie optical cavity. The cavity is tuned near the atomic D_2 transition (780 nm) from the $g = 5S_{1/2}$(F=2) ground state to the $e = 5P_{3/2}$(F=3)

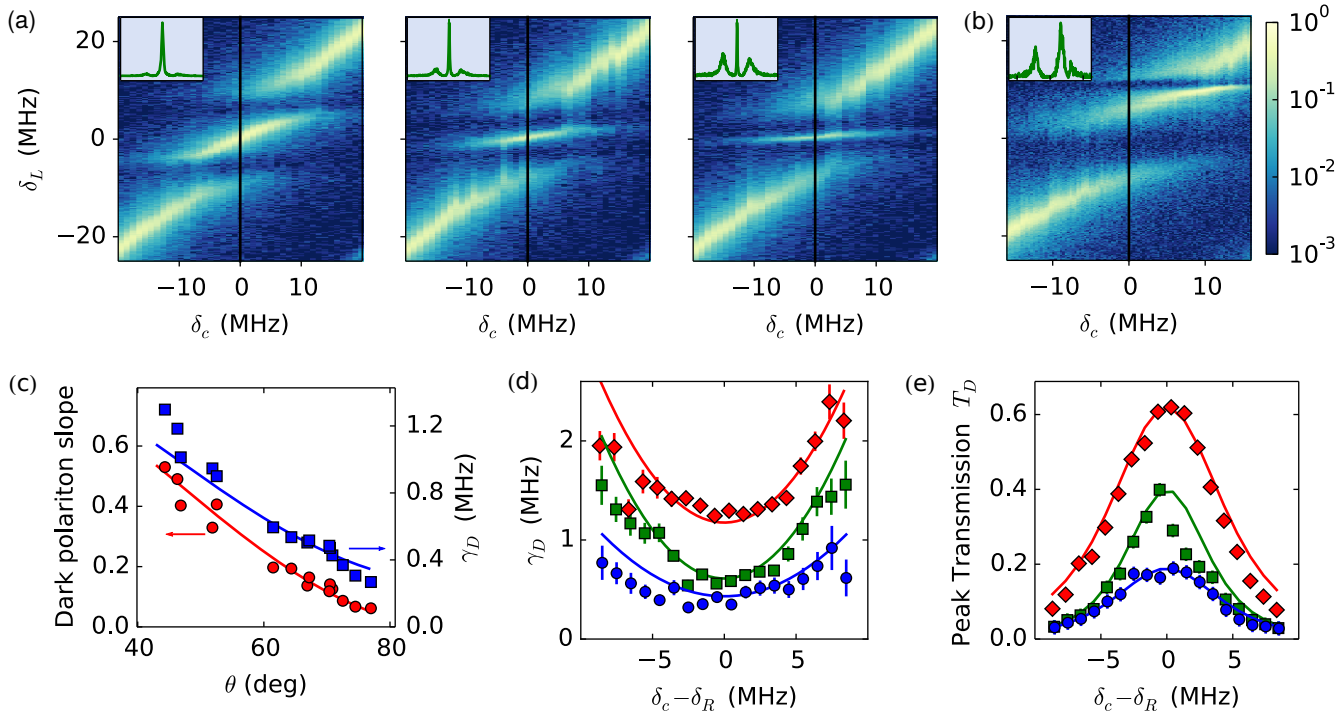

Figure 3.3: **Spectroscopy of Cavity Rydberg Polaritons.** (a) Cavity transmission spectra as a function of cavity detuning δ_C for several values of the control laser power. From left to right, (deg)=43, 62, 72; $\Omega/(2\pi)$= 13.1(1), 6.9(1), 4.9(1) MHz; $G/(2\pi) = 12.3(2)$, 13.0(1), 14.7(1) MHz. Here $|\delta_R| < 1$ MHz. Insets in (a) and (b): spectra along the vertical line at $\delta_C = 0$. Color scale for (a) and (b): cavity transmission as a fraction of the empty-cavity peak transmission. (b) Transmission spectrum at non-zero control laser detuning $\delta_R = 9.8(4)$ MHz. Here $\Omega = 2\pi\times$ 8.2(6) MHz, $G = 2\pi\times$ 16.8(3) MHz. (c) Energy and lifetime versus dark state rotation angle. Red circles (left): dark polariton slope $d\delta_D/d\delta_C$. Blue squares (right): dark polariton inverse lifetime γ_R. Solid lines: theoretical predictions, using Ω obtained from the calibrated control laser power and G obtained from fitting to the transmission spectrum. (d) and (e) show the effect of detuning the cavity from EIT resonance using the data in (a). Correspondence to (a): left–diamonds (red), middle–squares (green), right–circles (blue).(d) γ_R versus cavity detuning from EIT resonance. Solid lines: second-order prediction (3.12), using γ_R and G obtained from the transmission spectrum at $\delta_R - \delta_C$=0. (e) Height T_D of the dark polariton peak versus cavity detuning. Solid lines: theoretical prediction using (3.14) plus higher order corrections that are only significant for the lower (blue) curve.

excited state. The control laser (wavelength 480 nm, waist 29 μm) that couples to the $r = nS_{1/2}$ Rydberg level counter-propagates through the sample. Here we use primarily $n = 40$. At 780 nm, the cavity has a TEM_{00} mode waist of 12 μm $\times$ 11 μm ($1/e^2$ intensity radii) between the lower mirrors, and a finesse of 2500 (1.8 MHz FWHM linewidth). We obtain transmission spectra by sweeping the detuning δ_L of a probe laser (laser frequency minus the atomic transition frequency) linearly over 1 ms and detecting the transmitted light with a single-photon counter; the broad peaks are the lossy bright-polariton resonances, while the narrow central feature is the cavity Rydberg polariton dark resonance.

Because the polariton spends much of its time as a collective atomic excitation rather than a resonator photon, polariton dynamics are expected to be proportionally slower than those of their photonic constituent [46, 47]. We explore this effect thoroughly in Figure 3.3a,c, where we measure the resonator spectrum as a function of cavity frequency (within each frame of (a)), for various dark rotation angles (different frames of (a)). It is apparent that the energy of the dark polariton tunes *more slowly* than the cavity itself by a factor set by the dark-state rotation angle, as shown in Figure 3.3c, in quantitative agreement with a simple model:

$$\delta_D \approx \delta_C \cos^2\theta + \delta_R \sin^2\theta. \tag{3.10}$$

In the linear regime, the primary loss-channel for dark-polaritons is loss of their photonic component at a rate given by the cavity linewidth; the overall polariton loss is suppressed due to dark state-rotation:

$$\gamma_D \approx \kappa \cos^2\theta + \gamma_R \sin^2\theta. \tag{3.11}$$

The right axis in Fig. 3.3(c) shows the inverse lifetime γ_D obtained from the full-width at half-maximum of a Lorentzian fit to the dark polariton peak with the cavity at EIT resonance, compared to parameter free theory; it reaches a minimum of 0.26(1) MHz, significantly less than the bare cavity linewidth of 1.8 MHz.

3.2 Decoherence

The utility of polaritons strongly depends on their lifetime: realizing a strong single-photon nonlinearity with Rydberg polaritons in a single cavity mode requires an interaction energy [33] greater than the width of the polariton resonance, and photonic materials require stable polaritons to allow well-resolved many-body states [42]. Apart from the photonic loss discussed in the previous section, extra loss can also be induced by breaking the EIT resonance. This can happen because of energy shift from the Rydberg-Rydberg interaction at higher photon number state or weak harmonic trap that slightly break the degeneracy ground state. So it is crucial to understand how the polariton bandwidth relates to the two photon detuning.

Other inhomogeneous broadening can also affact the polariton performance. First, since the cloud has a finite temperature, and control field and cavity photon have different $\mathbf{k}$ vector, so Doppler effect can destroy the collective state by breaking the phase matching condition. Second, and more importantly, the Rydberg atoms with electrons highly excited are extremely sensitive to the ambient electric field gradient. However, we will show that the inhomogeneous broadening can be quadratically suppressed with higher control laser power through collective effect.

3.2.1 Homogeneous Decoherence

Polariton interactions, as well as spatial dynamics in a multimode cavity, would lead to a detuning from EIT resonance. This will slightly break the EIT condition and mix the excited state into the dark polariton, introducing an extra loss channel. Such effect has not been. A quantitative expression can be obtained by expanding the the eigen-value of the Hamiltonian to the next leading order terms:

$$\gamma_D \approx \kappa \cos^2\theta + \gamma \sin^2\theta + a(\delta_C - \delta_R)^2, \tag{3.12}$$

where $a = 4\Omega^2 G^2 \Gamma/(\Omega^2 + G^2)^3$ is the amplitude for the quadratic term. Fig. 3.3(d) shows the dependence of the polariton linewidth on detuning from EIT resonance, in quantitative agreement with this simple model.

One interesting question is how the linewidth of the dark polariton relates to the EIT window in a free space configuration. To see that, we can ask how much detuning from the EIT transition is required to double the linewidth of the dark polariton. In the limit of $\gamma_R \ll \kappa$, the detuning for the lifetime of the dark polariton will decrease by half can be written as

$$\delta_C - \delta_R = \Delta = \frac{1}{2}\frac{\Gamma}{\sqrt{OD}}\frac{1}{\cos^2\theta} \tag{3.13}$$

where $OD = \frac{Ng^2}{\kappa\Gamma}$ is the collective optical depth of the cloud. When the cavity is detuned by Δ, the dark polariton shifts by $\Delta\cos^2\theta = \frac{1}{2}\frac{\Omega^2\Gamma}{\sqrt{OD}}$, which is identical to the free space EIT linewidth. Another way to see this relation is to look at the EIT transmission with respect to the cavity detuning. We explore this behavior in Fig. 3.3(e), and observe that the peak transimission follows a squared Lorentzian,

$$T_D \propto \left[\frac{\frac{\Gamma_w}{2}}{(\delta_C - \delta_R)^2 + (\frac{\Gamma_w}{2})^2}\right]^2 \tag{3.14}$$

with $\Gamma_w \approx 2\Delta$ as defined above.

3.2.2 Inhomogeneous Decoherence

Comparing to a cavity that couples to a single atom, a Rydberg polariton is defined as a collective comprised of hundreds of atoms extended over a finite space. Thus the collective raising and lowering operator will have a phase factor associated with it depending on the location of the atoms. So in order to couple a collective state to the cavity mode, we need to match the amplitude as well as the longitudinal phase of the excitation. The ballistic movement of the atoms is able to smear out the phase and rotate the dark polation to

some collective Rydberg states that do not couple to cavity anymore. In this subsection, I will first recap the definition of a collective state with extended atomic sample, and further discuss two major decoherence mechanism of a dark polariton: Doppler effect and electric field gradient.

Doppler Decoherence

In the real experiment, our atomic sample has a size of ∼10 μm, which is much larger than the wavelength of a cavity photon (780 nm) and the blue laser (480 nm). The counter propagating beam setup reduces the susceptibility to Doppler decoherence since the two two k vectors cancels each other. But unlike the ground state EIT, the mismatch between the wavelength of a cavity photon and blue laser means the Doppler effect cannot be completely eliminated. With $\left|100S_{1/2}\right\rangle$, $\delta k = k_{Cavity} - k_{Blue} = 2\pi \times 1.24\mu$m means the dark state will have more than 2π of phase across a 10 μm long cloud. The size of the scatterer which is now the whole cloud then have a well defined momentum, and thus cannot backscatter the cavity photon which is crucial for making a Laughlin state. I will revisit this topic in chapter 6.

Since the cloud still has a finite temperature, the atoms are still moving in random directions and smear out the phase information of the dark polariton. It can easily be seen that the collective with a smaller k vector will be more resistive to this effect because the it requires the atoms to move a longer distance to cover a significant fraction of 2π. In this sense, the cavity Rydberg EIT, though still not as good as a ground state EIT, is much less susceptible to Doppler effect than the excited state polaritons. As a rough estimation, a cloud with 15 μK, the average time to move by π phase is ∼25μs, or 40 kHz broadening.

Stray Electric Field

We explore the dephasing due to an electric field gradient where have direct control over single-particle broadening by changing principle quantum number n of the Rydberg state,

and thereby the Rydberg polarizability α_n. Fig. 3.4(a) shows the loss rate γ_R of $|R_c\rangle$ versus α_n, obtained by fitting the measured spectra. For spectroscopy of completely independent atoms, γ_R would vary in proportion to the inhomogeneous broadening $\gamma_b \propto \alpha_n$ of the Rydberg level. However, the data in Fig. 3.4(a) vary quadratically with α_n. This suppression of decoherence arises because dephasing couples the collective Rydberg state $|r_c\rangle$ to a bath of collective excitations [48] of the hybridized and $|e\rangle$ levels, that, in turn, have no coupling to the cavity mode. In the rotating frame, these states are detuned by $\pm\Omega/2$ relative to the dark polariton (Fig. 3.4); For $\gamma_b < \Gamma, \Omega$, this detuning leads to a suppressed loss rate of $s_b\gamma_b^2\Gamma/\Omega^2$ from $|r_c\rangle$; numerical simulations reveal that $s_b \approx 4$, for a normal distribution of Stark shifts with standard deviation γ_b. The simulations confirm that Doppler decoherence is similarly suppressed, and that while inhomogeneous control-field coupling does renormalize $|r_c\rangle$, a dark state exists which is negligibly broadened by the inhomogeneous coupling.

This novel suppression of inhomogeneous broadening should be contrasted with the unsuppressed inhomogeneous decoherence of spin-waves *in the dark*, observed in numerous DLCZ-style single-photon source experiments [11–13]. The presence of the control field allows the spin-wave to continuously refresh itself, suppressing the decoherence that would otherwise be present; indeed, we predict a parameter regime in which the spin-wave *lives longer* in the presence of the read-out field.

3.3 Slow Dynamics

To employ cavity polaritons in quantum materials, it is essential to harness multiple cavity modes simultaneously. The different cavity modes correspond to the single polariton eigenstates resulting from motional dynamics in harmonic traps or photonic Landau levels [31, 33, 38]. For quantum information processing, the different modes can be used to implement one [49] or more [50] qubits. Here we demonstrate, for the first time, Rydberg EIT in two cavity modes.

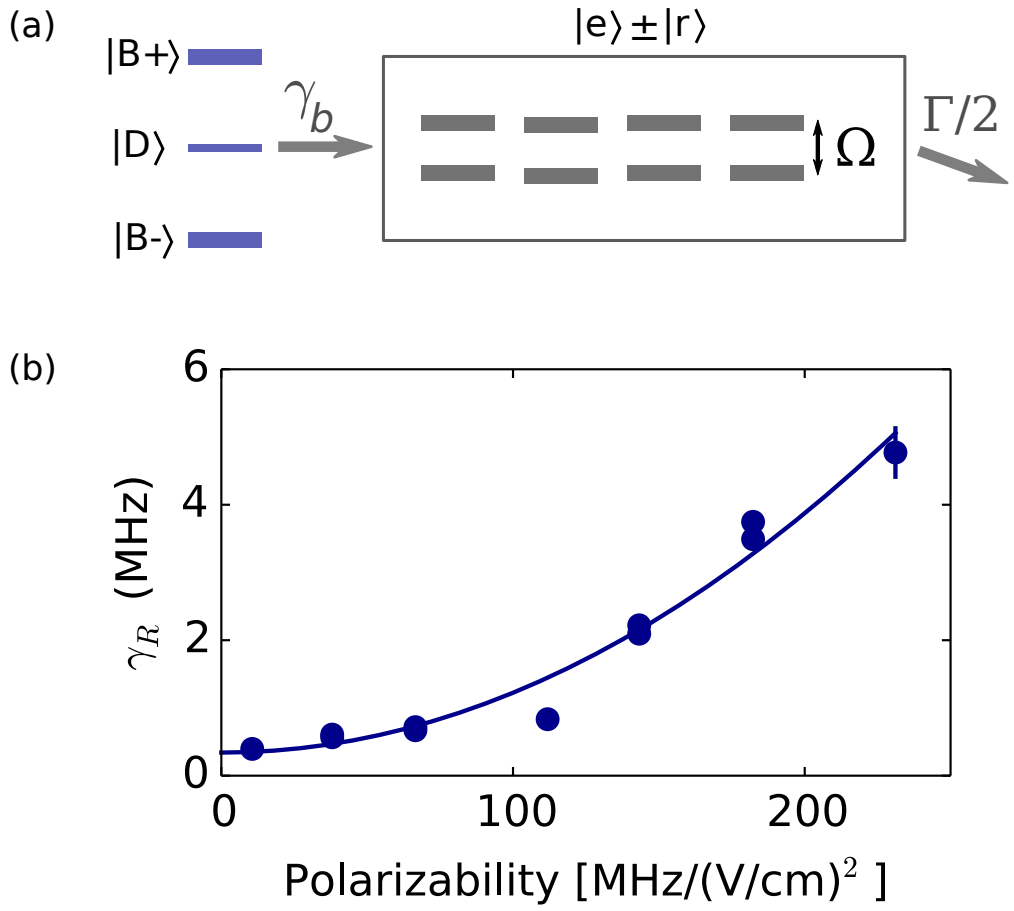

Figure 3.4: **Collective Suppression of Decoherence.** (a) Inhomogeneous broadening couples the dark polariton to a bath of states orthogonal to the cavity mode. The splitting from the control laser detunes these states from the dark state, suppressing the lossy channel. (b) Effective decay rate γ_R of the collective Rydberg state for varying principle quantum number n versus the polarizability of the Rydberg state. Here n=40, 48, 52, 56, 58, 60, and 62. Ω (MHz)=7.8(5), G (MHz) = 12(2), average and std. dev. over the data sets. Solid line: quadratic fit.

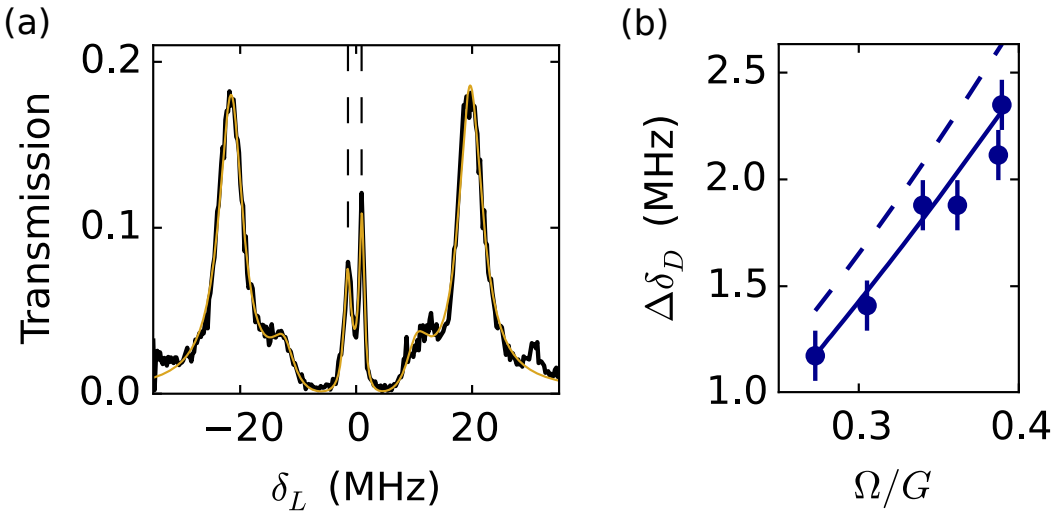

Figure 3.5: **Rydberg Polaritons in Two Cavity Modes.** The TEM_{02} and TEM_{10} modes are tuned to ±10 MHz from EIT resonance. (a) Transmission spectrum for Ω/G=0.39, with $G = 27$ MHz. The dark polariton resonances (dashed lines) are separated by $\Delta\delta_b = 2.3$ MHz. Curve: fit to theoretical model for two orthogonal collective states. (b) Adjusting the control laser power varies the photonic component of the dark polariton states, tuning $\Delta\delta_D$. Dashed curve: first-order prediction (3.15). Solid curve: numerical solution.

Our experimental cavity is designed such that the TEM_{02} and TEM_{10} modes are nearly degenerate, with a separation of 20 MHz, while the TEM_{00} mode is isolated. This mode spectrum allows us to switch seemlessly between single-mode EIT physics in the TEM_{00} mode and multimode physics in the TEM_{02} and TEM_{10} manifold by tuning the cavity length through the cavity lock. To demonstrate dark polaritons in two modes, we tune the TEM_{02} and TEM_{10} modes to either side of the atomic resonance. We align our probe beam to couple to both modes, and collect the transmitted light in a multimode fiber. Fig. 3.5 shows a measured transmission spectrum for two-mode cavity Rydberg EIT. The two central peaks are dark polaritons in the two modes and are separated by much less than 20 MHz due to strong light-matter mixing.

Fig. 3.5 shows that the splitting between the two dark polariton peaks can be tuned by varying the laser couplings. The separation between the two dark polariton peaks, $\Delta\delta_D$, is

given approximately by:

$$\Delta\delta_D \approx \Delta\delta_c \cos^2 \tag{3.15}$$

with $\Delta\delta_c = 20$ MHz, plus higher order corrections in $\Delta\delta_c$. The compression of the dark polariton spectrum relative to the bare cavity spectrum is analogous to the slowing of the group velocity in free space EIT [45], and indicates that the transverse polariton dynamics in a multimode resonator follow those of bare cavity photons, slowed by a factor of $\cos^2\theta_D$. This implies that dark polaritons are imbued with the mass, trapping frequency, and effective magnetic field of their photonic constituents [31, 33, 38].

CHAPTER 4

STRONGLY INTERACTING PHOTON

In this chapter, I will introduce our work in generating and probing the photon-photon interaction down to the single particle level using the cavity Rydberg polariton technique. Due to the large blockade volume of a Rydberg atom at principle quantum number ($n = 100$ in this chapter), the entire thermal gas can act as a single "super atom" with an enhanced cross section. The use of an optical resonator also greatly improve the optical depth per blockade volume (OD_B), a crucial quantity that governs the number of collisions per polariton lifetime in a synthetic material and the gate fidelity in a photonic quantum information processor [51]. The isolated cavity mode also allows us to treat the whole cavity-atom complex as a quantum dot which is comprised of many particles but only possess one mode due to the tight confinement. This makes it a better candidate for being operated as a quantum gate comparing to the free space experiment.

I will first discuss the figure of merit of the photon-photon interaction. With the understanding of detuning induced loss from chapter 3, it can be shown that the OD_B is indeed the quantity that describes the quality of the quantum dot. Interaction between polaritons at high principle quantum number can then be observed in the non-linear spectroscopy. To demonstrate the interaction is happening at the single photon level, we study the blockaded cavity transmission and show a non-classical photon statistics. Finally, we investigate the dimentionality of the cavity-atom system by measuring the Rabi oscillation of the dark polaritons hopping into and out of the cavity, the behaviour only in a two-level system.

The text of this chapter is based on the publication [52] which the author made the major contribution.

4.1 Figure of Merit of the Interaction

In this section we will attempt to understand how well a polaritonic quasi-particle "holds together" in the face of forces on its photonic and and material components, with the former coming from an applied external potential and the latter from polariton-polariton collisions. We will find that, under optimal conditions, the polariton can undergo $\sim \sqrt{OD_B}$ collisions within its lifetime; this is an intuitively satisfying result because it says that our intuition that OD_B characterizes the "strength" of the coupling between the light and matter is correct.

4.1.1 Polariton-Confinement Collisions

The simpler story to understand is the interaction of a single polariton with a confining potential. We consider two photonic modes; a spatially even mode, and a spatially odd mode, with energy splitting Δ, and prepare our polariton in a superposition of these two modes. We would like to know how many oscillation cycles the polariton undergoes before it decays. Larger Δ means that the polariton oscillates more quickly, but will also eventually reduce its lifetime by driving one component of the superposition state out of the EIT window.

To quantitatively understand this problem, we compute the dependence of polariton linewidth and shift upon Δ, the energy of the odd-component of the polariton. We follow the derivation in [43, 53], and find:

$$E_{pol} \approx i\frac{2\kappa\Omega^2}{4G^2+\kappa\Gamma+4\Omega^2} + \Delta\frac{16\Omega^2(G^2+\Omega^2)}{(4G^2+\kappa\Gamma+4\Omega^2)^2} + i\Delta^2\frac{32\Omega^2\Gamma(G^2+\Omega^2)}{(4G^2+\kappa\Gamma+4\Omega^2)^3} \tag{4.1}$$

Here the imaginary part of E_{pol} reflect its linewidth, and the real part its energy shift; it is thus apparent that $N_{coll} \approx \frac{Re(E_{pol})}{Im(E_{pol})}$. Writing $E_{pol} = i(\alpha+\beta\Delta^2)+\gamma\Delta$ and optimizing over Δ one finds a maximum of $N_{coll} = \frac{1}{2}\sqrt{\frac{\gamma^2}{\alpha\beta}}$ for $\Delta = \sqrt{\frac{\alpha}{\beta}}$. Substituting the full expressions for α, β and γ yields $N_{coll} = \sqrt{\frac{G^2}{\kappa\Gamma}} = \frac{1}{2}\sqrt{OD_B}$ (in the limit $\Omega \ll G$, where polaritons interact

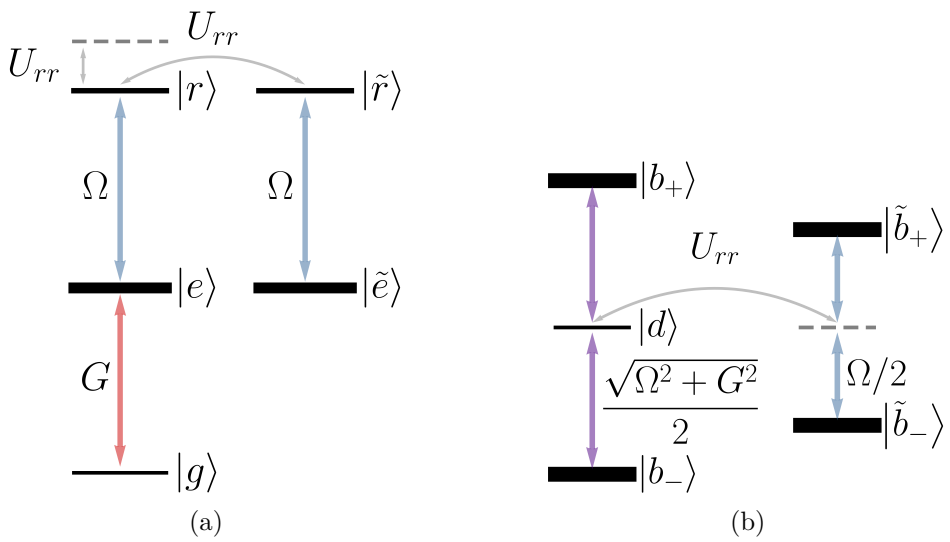

Figure 4.1: **(a)** Three-level system with coupling (αU_{rr}) to another manifold of collective Rydberg $|\tilde{r}\rangle$ and excited states $|\tilde{e}\rangle$ that are uncoupled from the resonator. The Rydberg-Rydberg interaction detunes the Rydberg state and also couples the two manifolds. The extra states are coupled by the blue laser with Rabi frequency Ω. **(b)** The same system expressed in the polariton basis. The bright polaritons $|b_-\rangle$ and $|b_+\rangle$ are no longer at the same energy as the dark polariton $|d\rangle$ due to the probe and control field couplings. Similarly, the lossy manifold splits in energy because of the control field.

strongly and the quadratic expression for E_{pol} is valid).

4.1.2 Polariton-Polariton Collisions

Here we suppose that there is no limit upon the available interaction strength between Rydberg atoms, and attempt to compute how many "collisions" (how many 2π of interaction-phase) we can accumulate between a pair of polaritons within their lifetimes. At first glance, it appears that in the limit $\frac{\Omega}{g} \to 0$, $N_{coll} \to \infty$; the reasoning is that in the limit of no control field ($\Omega \to 0$), the polariton becomes infinitely long-lived (cavity leakage is reduced to nothing), with finite interaction strength. The problem with this argument is that the (infinitesimal) remaining photonic component will be unable to follow the rapidly evolving spatial mode of the Rydberg components.

Put another way, imagine a single mode optical cavity akin to the one employed in

our experiments; the Rydberg-Rydberg interactions will provide an pairwise separation-dependent energy shift which rotates the two-polariton state out of the spatial mode of the cavity, thereby acting at least in part as a *decoherence* channel in the polariton basis!

To quantify this effect, we compute the perturbative impact of interactions between two dark polaritons: The "average" atomic interaction U_{rr} can be mapped onto the polariton-polariton interaction U_{DP} through the relation

$$U_{DP} = U_{rr} \sin^4 \theta \tag{4.2}$$

where $\theta = \arctan G/\Omega$ is the dark state rotation angle.

Aside from the single polariton loss $\kappa \cos^2 \theta + \gamma_r \sin^2 \theta$ (note that we will assume $\gamma_r = 0$ for the remainder of this SI), the interaction introduces two sources of decoherence: tuning of the individual polaritons out of the EIT window, and coupling to collective Rydberg/excited states that do not couple to the cavity mode. The extra loss caused by detuning is given by [43]:

$$\gamma_\Delta = \frac{2\Gamma U_{rr}^2 \sin^2 \theta}{(G^2 + \Omega^2)} \tag{4.3}$$

The interaction also couples the collective Rydberg state $|rr\rangle$ to another collective Rydberg state $|\tilde{r}\tilde{r}\rangle$ with a different Rydberg distribution (Fig. 4.1a). The control beam will then couple $|\tilde{r}\tilde{r}\rangle$ to a collective excited state $|\tilde{e}\tilde{e}\rangle$ that will not couple to the cavity mode due to symmetry. In the polariton basis (Fig. 4.1b), the Rydberg-Rydberg interaction couples the dark polariton state to the loss states detuned by Ω, and the interaction induced polariton loss can be calculated using the methods employed for collective Doppler decoherence suppression [43] as:

$$\gamma_{int} = \alpha \frac{U_{rr}^2}{\Omega^2} \Gamma \tag{4.4}$$

where α is the geometric factor of order unity reflecting the precise form of the interactions and the cavity mode.

The number of collision within a polariton lifetime can then be calculated as:

$$N_{coll} \approx \frac{U_{DP}}{\gamma_{DP}} \tag{4.5}$$

with:

$$U_{DP} = U_{rr} \sin^4 \theta \tag{4.6}$$

$$\gamma_{DP} = \kappa \cos^2 \theta + \gamma_\Delta + \gamma_{int}. \tag{4.7}$$

The optimal number of collisions is obtained by maximizing N_{coll} with respect to U_{rr} and Ω, and is given by

$$N_{max} = \sqrt{\frac{OD_B}{4\alpha}} \tag{4.8}$$

where $OD_B = N\eta = N\frac{G^2}{\kappa\Gamma}$ is the optical depth per blockade volume. This optimum occurs as the control field intensity vanishes $\Omega \to 0$, so long as the intrinsic decoherence of a single collective Rydberg excitation is ignorable $\gamma_r \approx 0$. Here we have used the fact that in our experiment all the atoms are distributed within a blockade volume.

4.2 Cavity Details

Our four mirror running wave resonator is arranged in a bow-tie configuration comprised of two convex mirrors and two concave mirrors in order to satisfy several opposing design constraints. To force cavity Rydberg polaritons to interact, the atomic sample size must be suitably small. The participating atomic region may be defined in two dimensions by the resonator mode cross-section, so the mode waist must be small (or radial slicing of the atomic cloud must be performed); we targeted 10-15 μm. The simplest technique for creating a stable resonator with a small waist is to use short focal length mirrors relatively close together. However, from our experience with a previous experimental cavity and its

electric field filter [43], we found that any material close to Rydberg atoms, either dielectric or metallic, will build up charges or dipoles (from Rb adsorbates), the electric fields from which unacceptably broaden Rydberg lines above $n \sim 60$. This necessitates using longer focal length mirrors so that they may be placed further apart. Then, the only way to produce a small waist is a large mode size on the surface of these mirrors. For this reason, bow-tie resonators often have a longer upper arm with relatively flat mirrors so that the beam may expand due to diffraction, thereby increasing the beam size at the lower mirrors and so reducing the waist size. Having a longer upper arm, however, was unacceptable for two reasons: First, the resonator linewidth would decrease (at constant finesse), which proportionally decreases the data collection rate, (and the autocorrelation-data rate goes as the square of this rate). Second, the resonator is loaded into our vacuum chamber through a 62 mm diameter tube, which therefore sets an absolute maximum exterior size. Both of these limitations could be avoided, however, by utilizing convex mirrors in the upper arm; the defocus that they create acts, for our purposes, equivalently to diffractive expansion.

4.3 Mean-Field Interaction

The polariton-polariton interaction can first be observed in a non-linear spectroscopy even without the slicing process described in section 2.5. The polaritons are already well confined in the transverse plane by the small cavity waist, but due to the large overlapping between the cavity mode and atomic cloud in the longitudinal direction allows the cavity to support more than one polaritons. However, the interaction between each photon pair induces excessive loss, and when many photons are populated inside the cavity it can be observed as a mean-field interaction and suppress the dark polariton transmission.

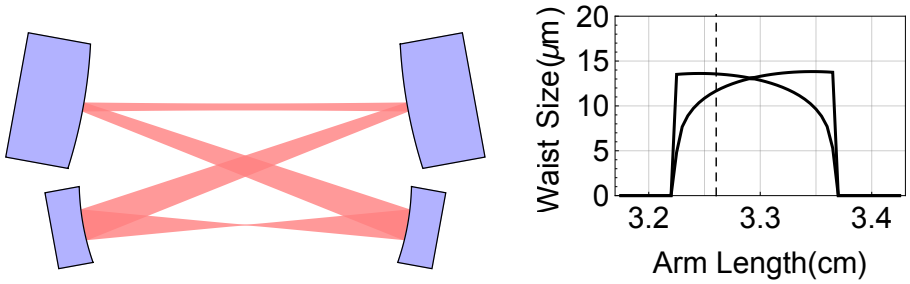

(a)

(b)

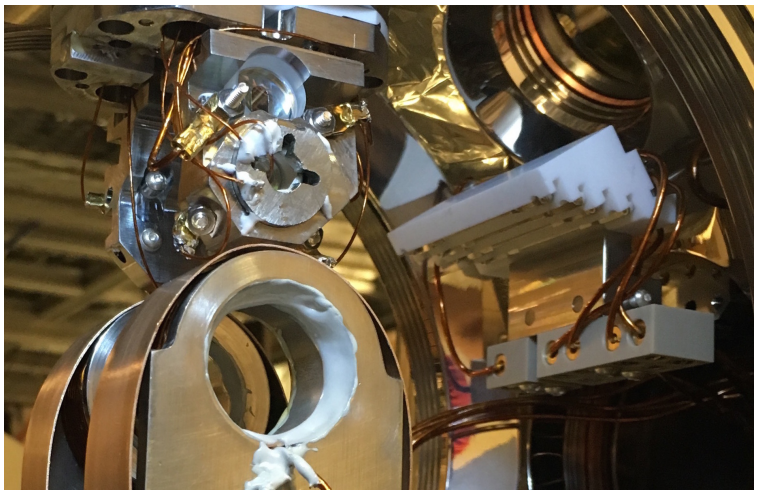

(c)

Figure 4.2: **(a)** A schematic of the resonator. The transverse size of the mode reflects the results of numerical calculation given the resonator geometry and is represented to scale but for a factor of 10 magnification compared to the mirror dimensions and locations. **(b)** The numerically calculated mode waist sizes are plotted as the resonator length is increased with constant aspect ratio. The cavity is stable over a 1.5 mm range, although near the edges of that range, it becomes significantly astigmatic. We set out to build the resonator at the middle where the modes waists are equal; however, assembly imperfections resulted in a somewhat shorter actual length, indicated by the dashed line. **(c)** A photograph of the in-vacuum experimental apparatus showing the resonator (top), the MOT coils (bottom), and Rubidium dispensers in their macor mount (right). The lower resonator mirror is mounted on a piezo tube which is glued to the lower circular steel disk on the resonator structure. Through the upper mirror, a narrow slot may be seen. Such slots are the only opening to the front of the mirrors and serve as a passive electric field filter to reduce the effect of charges that may build up on the mirrors' dielectric surfaces. Six out of the eight electrodes are visible: four from the outside showing their attachment to wires via gold plated crimps, and two on the inner surface of the cavity. The heads of the screws form the surface of the electrode.

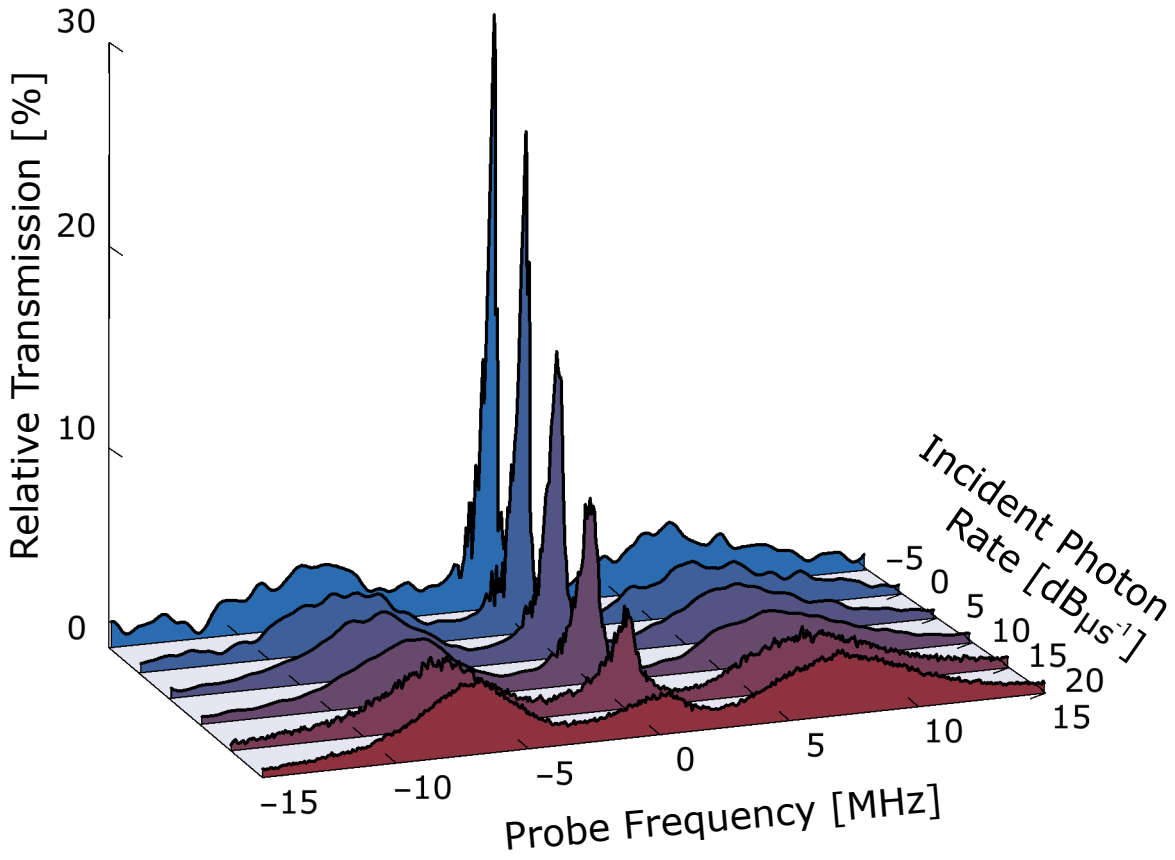

Figure 4.3: **Nonlinear Spectroscopy of a Polaritonic Quantum Dot.** The quantum dot's transmission versus probe frequency is plotted for increasing incident photon rates. Here, the sample is unsliced and thus contains several (~ 3) blockade volumes, resulting in weak, nearly mean-field interactions. We thus observe smooth broadening and transmission suppression of the dark polariton peak (at $\delta = 0$ MHz). The bright polariton resonances at $\delta = \pm 7$ MHz are not suppressed at high probe rate, because bright polaritons have little Rydberg admixture and are thus essentially non-interacting. The data for the three lowest powers are Gaussian filtered (with $\sigma_{filter} = 481$ kHz) outside of the interval (-1.5 MHz, 1.5 MHz); all data are normalized to the bare cavity transmission.

4.3.1 Non-Linear Spectrum

Fig. 4.3 shows the spectrum of different probe power normalized to the empty cavity. At the lowest probe power, the transmission exhibits a typical EIT spectrum with a narrow dark polariton peak at zero detuning. With increasing power, the relative transmission of the dark polariton drops, indicating a repulsive interaction between the polaritons. As a reference, the two bright polariton resonances have the same relative transmission for all the probe power since they have a much larger loss and less Rydberg portion.

4.4 Blockade Transmission

To enter the strong interaction limit, we further confine the polariton by slicing the cloud to approximately 12 μm which is comparable to the blockade volume of $n = 100$ Rydberg state. The strong Rydberg-Rydberg interaction shifts and broadens the energy of the two photon manifold and thus prevents later photons from tunneling into the cavity with presence of a existing polariton. One can make analogy between the cavity-atom system and a electronic quantum dot where the electrons are deeply confined in a microcavity and the second electron is blockaded by the repulsive Coulomb interaction. inn a electronic quantum dot, the number of electrons in the dot can only be implied by the quantized gate voltage, and a direct measurement of statistics of individual electron turns out to be technically hard. In a cavity QED system, however, counting individual quanta can be done with single photon counting module and the statistics of the transmitted photon, which is a strong evidence of the quantum nature of the system, can be obtained through the temporal correlation functions.

4.4.1 Strong Interaction and Photon Anti-Bunching

One of the main purpose in this section is to demonstrate by hybridizing the photons with Rydberg excitation, we can achieve strong interaction between individual photons. As dis-

cussed in section4.1, in order to create a entangled state, the interaction required must be much stronger than the lifetime of the quasi-particles. This also suggests that the dynamics of two photon state is drastically different from the single photon one, which then calls for a non-classical description of the photons.

To experimentally show the non-classical character of the cavity photon, we probe the temporal auto-correlation function of the transmitted photons defined as

$$g_2(\tau) = \frac{\left\langle : a^\dagger(t)a^\dagger(t+\tau)a(t)a(t+\tau) : \right\rangle}{\left\langle a^\dagger(t)a(t)\right\rangle \left\langle a^\dagger(t+\tau)a(t+\tau)\right\rangle}, \tag{4.9}$$

where the colons represents the normal ordering the the raising and lowering operators. For a classical light, for example a coherent state or thermal state, it can be proven (cite Jon's thesis) that

$$g_2(0) \geq 1 \tag{4.10a}$$

$$g_2(\tau) \leq g_2(0). \tag{4.10b}$$

We will focus primarily on the former equation. Classically, this equation says that when a classical beam is split on a beam-splitter, fluctuations above the mean on one output port will be accompanied by fluctuations above the mean on the other output port. This is to be contrasted with a source of single photons: when a single photon impinges upon a beam-splitter it must chooses to go one way or the other, and so the two output ports will be anti-correlated. Practically, it turns out that assuming that $\hat{n}(t)$ is a non-negative real valued function $\hat{n}(t) \in \mathbb{R}$ is sufficient to prove the above inequalities: this says that any violation comes explicitly from the quantized nature of the electromagnetic field.

4.4.2 Measuring the Photon Statistics

Unlike its electronic counter part where detecting single electron is technically hard, a optical quantum dot provides a ideal platform for measuring the arrival time of each individual photon and from that extract the auto-correlation function of the transmitted photon fields.

Optical Setup

After the normal sample preparation and transport procedure detailed in section 2.3 which is the same as the spectrum measurement, one slicing cycle is performed in order to reduce the atomic size along the cavity axis before the probe beam is turned on. Since we are trying to study the dark polariton only, the frequency of the probe laser is fixed to the dark polariton resonance extracted from the spectrum. Since the cloud size is small ($\sim$10 μm), the ballistic expansion would quickly increase faster in terms of relative size:

$$\frac{\sigma(t)}{\sigma(0)} = \sqrt{1 + \frac{k_B T}{\sigma(0)^2 m_{Rb}} t^2}. \tag{4.11}$$

Since the strong coupling relies on the blockade volume to be comparable or bigger than the atomic thickness, the probe length has to be shorter than the time for the cloud to expand to twice of its original size. In our experiment, we use a 100 μs slicing-probe cycle in which 25 μs is used for slicing and then probe for 75 μs. During the probe time, the lattice beam is turned off to avoid in-homogeneous broadening, and the cloud is going through a free fall as well as thermal expansion. The time scale for both process is much longer than one slicing-probe cycle. So to increase the total probing time per sample, we perform 10 cycles during the 1 ms total probe time. This number is basically limited by the decreasing central density, which decides the number of atoms after the slicing, due to the expansion. A magic lattice of even a optical dipole trap can significantly increase the total probe time by confining the cloud in the transverse direction.

The output photons are sent throught a 50:50 beam splitter and two single photon count-

ing modules (SPCM) are aligned to the two output ports of the cube to record the photon arrival time. Once a photon hit the detector, the SPCM will output a 5 V TTL pulse which then triggers a FPGA channel for registering the time.

Photon Detector

The photo detector we use has a time resolution of 50 ns and a dark count rate of 50 Hz. In the real experiment, we found the measured count rate with the probe beam off is about 500 Hz. Part of the counts are coming from the electronic path after turning the gate from off to on at the beginning of the probe, and this problem can be easily fixed by turning the SPCM on 10 ms before the actual probe. Also, in the presence of the 480 nm control field, we experience 200 Hz of additional counts even with interference filters (blocking 300-1200 nm, save a $\pm \sim$1 nm interval around 780 nm) placed in the 480nm path immediately before the vacuum chamber.

The source of this background is either fluorescence or spontaneous parametric down-conversion of 480 nm photons *within the resonator mirrors and vacuum chamber windows* to 780 nm; this effect is not observable with single-mode fibers in the detection path, as both fluorescence and SPDC are highly multi-mode and are thus filtered out. The down-conversion almost certainly occurs within the resonator mirrors: because the control beam is focused to a tight spot at the resonator waist, the intensity of the beam in the resonator mirrors is much higher than in any other piece of glass.

Time Recording

The photons blockade each other within the polariton lifetime about few microseconds, requiring the time resolution of the photon register to be higher than $\sim$10 MHz. A field programmable gate array (FPGA) board with a clock speed of 125 MHZ is used to recording the time of TTL signals generated by the SPCMs. The FPGA uses a different trigger than the SPCM such that it only record events during the 1 ms probe time. Since the FPGA

records photon during both the probe time and the slicing process, we need to calibrate the absolute timing of the actual experiment sequence and extra delay caused by the cable length difference between the two channels. To measure the real time in FPGA clock cycles, we send the TTL controlling the probe laser AOM directly into two channels of the FPGA and record the time of the rising edge of the pulse.

Extract g_2 from Photon Arrival Time

The data we record is the time of each detected photon, while the g_2 is defined using the probablity of one and two photon events. Here, I will briefly work out the math to convert the real data to the auto-correlation function. The denominator is probability of the single photon events and is straight forward to calculate. Since there are ten slicing-probe cycles per experiment run and the SPCMs are recording the photons scattered from both the slicing and probe duty. Hence we have to chop the data before counting the total number events of both detectors N_A and N_B. To obtain the detection probablity, we have to divide those numbers with the *total* probe time:

$$t_{probe} = N_{exp} \times N_{slice} \times N_{clk} \times t_{clk} \tag{4.12}$$

where N_{exp}, N_{slice}, and N_{clk} are the number of total experiment run, slicing-probe cycle, and clock cycles per cycle. t_{clk} is the absolute time of one FPGA clock cycle.

The two photon event list $N_{AB}(\tau)$ is calculated by looping over each event in A and B detectors and build the histogram of the two photon events for every available time difference $\tau = t_A - t_B$. It is worth noting that the $N_{AB}(\tau)$ already has the unit of $1/$ since we have taken an integration using the loop. So to have the two-photon probability P_{AB}, we only

have to divide $N_{AB}(\tau)$ with t_{probe}. The auto-correlation function can then be written as

$$\begin{aligned} g_2(\tau) &= \frac{P_{AB}}{P_A \times P_B} \\ &= \frac{t_{clk} N_{exp} N_{slice} N_{AB}}{N_A N_B} \end{aligned} \tag{4.13}$$

This expression is valid if only the time scale we are interested in is much smaller than the probe time per slice since the probability of detecting two photons at large τ is smaller due to the finite probe time. The correlation function at large time delay which is predicted to be a coherent state is needed to compare with $g_2(0)$, so to compensate this effect, we apply another normalization factor based on τ and total probe time $t_cyl = N_{clk} t_{clk}$

$$A(\tau) = \tau / t_{clk}. \tag{4.14}$$

Another factor that limits the data quality is the dark counts from the photon detector. The absolute number can be measured by performing the same experiment but without the probe laser. The total measured dark counts is about 300 Hz per detector, and this can be subtracted from the g_2 equation by using

$$\tilde{N}_{AB} = N_{AB} - D_A N_B - D_B N_A - D_A D_B \tag{4.15}$$

$$\tilde{N}_A = N_A - D_B * N_A \tag{4.16}$$

$$\tilde{N}_B = N_B - D_A * N_B \tag{4.17}$$

$$\tag{4.18}$$

4.4.3 Observation of Photon Anti-Bunching

After slicing the cloud so that it can hold only a single polariton at a time, we observe almost complete suppression ($g_2(0) = 0.27(8)$) of simultaneous tunneling through the dot, indicative of transport blockade due to strong interactions (Fig. 4.4a). Indeed, strong anti-bunching at zero-time separation validates a model where a single intra-cavity polariton shifts and broadens the energy for the injection of the next polariton by more than the polariton linewidth, strongly suppressing its tunneling into the resonator until the first polariton tunnels out. The observed $g_2(\tau)$ is consistent with a master-equation effective theory bootstrapped by a full model of interacting 3-level atoms coupled to a single resonator mode. Note that the linear growth of $g_2(\tau)$ near zero delay, as opposed to the quadratic growth anticipated from a single-mode theory, arises from virtual excitation of bright polaritons.

We verify that the observed transport blockade results from strongly interacting polaritons by comparing to transport with weaker interactions. First we test the unsliced cloud (gray curve in Fig. 4.4a), which exhibits only weak suppression of g_2 near $\tau = 0$ because the cloud is large enough to hold multiple polaritons along the resonator axis simultaneously. Similarly, a sliced sample with Rydberg atoms in the smaller $85S$ state can fit multiple excitations transversely and also exhibits weak suppression of g_2 (blue curve in Fig. 4.4b). Furthermore, we find that transport of bright polaritons is not blockaded at all (orange curve in Fig. 4.4b), as these polaritons are essentially non-interacting [54]. The blockade of the dark polaritons can even be "reversed" by detuning from the atomic 5P state to make the polariton-polariton scattering more elastic and probing transport on the two-polariton resonance (Fig. 4.4c). In this case we observe photon bunching, $g_2 > 1$, reflecting the preferential transit of photon pairs [55].

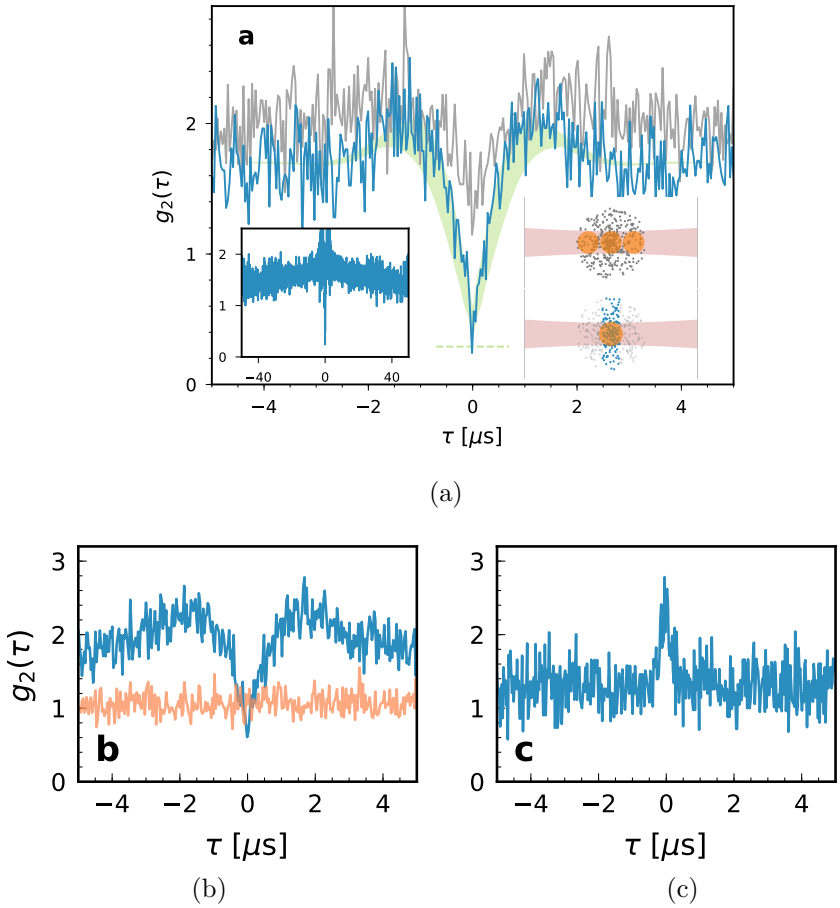

(a)

(b) (c)

Figure 4.4: **Transport Blockade of Cavity Rydberg Polaritons. (a)** A smoking gun of strong interactions in a quantum dot is blockade: the suppression of near-simultaneous particle transmission. The temporal intensity autocorrelation function $g_2(\tau)$ on the dark polariton resonance with a sliced atomic cloud reveals strong blockade: a ∼5x suppression of two-photon events relative to the long-time value shown in the inset (blue curve, $g_2 = 0.27(8)$ near $\tau = 0$ compared to $g_2 = 1.3$ at long times). The green dashed line and band are the theoretically predicted minimum value and time-dynamics, respectively The unsliced cloud contains numerous blockade volumes; accordingly it provides a weaker suppression of g_2 near $\tau = 0$ (gray). In the inset, the time-bins for $|\tau| > 0.8$ μs are larger by a factor 4 to reveal large τ trends. **(b)** On the dark polariton resonance of the $85S_{1/2}$ Rydberg state (blue), the suppression of g_2 is reduced because multiple blockade volumes fit in the transverse plane. On the bright polariton resonance at 100S with a sliced cloud (orange), polaritons are very weakly interacting, resulting in uncorrelated transmission. **(c)** We observe bunching ($g_2(0) > 0$) when probing near a two-polariton resonance, achieved by shifting the cavity resonance by −5 MHz, increasing the control frequency by 5 MHz and probing −1 MHz from the single-polariton resonance. In each panel, the large-τ value of g_2 exceeds 1 due to atom number fluctuations, which lead to a variation in the on-resonance transmission.

4.5 Time Dynamics

The whole cavity-atom system can now be effectively understood as a quantum dot or single emitter without extra degrees of freedom for photons. However, the transport blockade effect does not provide information about the dimensionality along the transport direction. A quantum wire experiment also exhibits a sub-Poissonian statistics of the transmitted photon. So in order to investigate the dimensionality of the polaritonic dot, we probe the cavity with pulses of substantially higher intensity and observe the transmitted light as the intracavity field rings up and then down. A zero-dimensional system may be coherently excited and then *de-excited* by the drive field, exhibiting Rabi oscillations, while in a one dimensional system the excitation would propagate away before it can be removed.

4.5.1 Pulse Probe of the Cavity

By measuring the linewidth of the dark polariton, we can get a rough estimation of its decoherence time $\sim$3 μs which is much shorter than the 75 μs probing time per slice cycle. To further increase our data rate, we use a function generator triggered by digital card to modulate the probe laser with a frequnecy of 100 kHz. As a result, we perform about 10 measurements per slicing-probe cycle or 100 measurements per sample. The transmission is then calculate by simply taking the sum of each modulation cycles. We vary the probe intensity by changing the probe laser AOM RF power level. In Fig. 4.5, we show the summed cavity transmission of (a) completely unfolded data, (b) folded data for re-slicing (red in (a)), and (c) second folding for probe modulation (blue in (b)). The fact that all three curves laying on top of each other shows a good consistency through out the whole 1 ms probe.

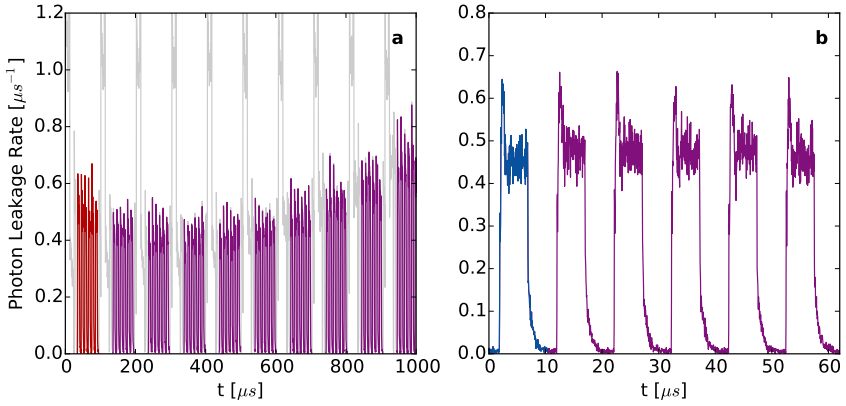

(a)

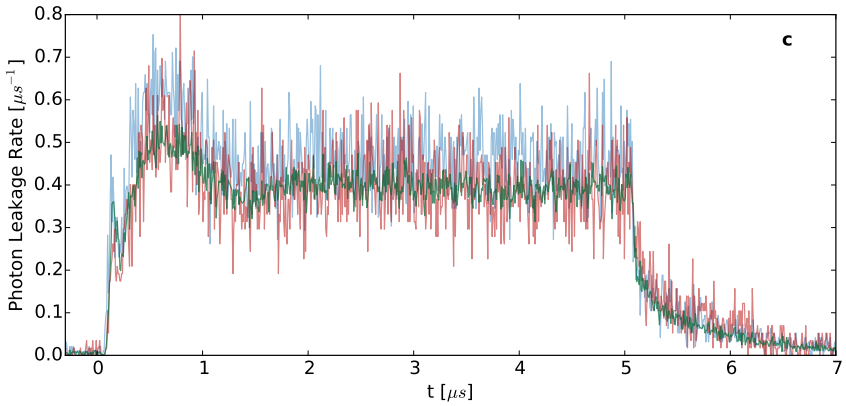

(b)

Figure 4.5: **Ringdown Count Arrival Histogram. (a)** The entirely unfolded ringdown histogram of photon arrival times (data from Fig. 4.6, highest power) is built up over 16,000 individual runs of the experiment. Ten 'reslicing' intervals are apparent, with the data used highlighted in purple, and the first reslicing interval in orange. The smooth and relatively minor fluctuation in the transmission rate over the course of the 1 ms total probe time indicates successful reslicing with constant atom number and the lack of shelved Rydbergs which would reduce the transmission. **(b)** The same data are folded over each reslicing interval, with the excess depump and repump photons as well as the first and last probe cycles cut out. This leaves six 10 μs probe cycles, the first of which is highlighted in blue. When all six are folded on top of each other, they yield data for Fig. 4.6. The steady transmission is constant over these cycles indicating that Rydbergs are not being shelved. **(c)** To investigate the possible buildup of stray Rydberg atoms, we plot the folded data of the first reslicing interval in orange, the folded data of the first probe cycle from all reslicing intervals in blue, the entire folded dataset (same as Fig. 4.6, highest power) in green. If stray Rydbergs were developing during each 1 ms run or within each reslicing interval, either the orange or blue curves should saturate to a significantly higher leakage rate.

4.5.2 Rabi Oscillation of Dark Polariton

We perform the pulse measurement with different probe power settings. In Fig. 4.6a, we show the ring-up and down dynamics of the dark polaritons at multiple probe strength. The total transmission increases with higher probe power. Oscillations gradually emerge during the ring-up process also with increasing freuqnecy as we turn up the probe power.

To extract the measured Rabi oscillation frequency between zero and one polaritons from the highest probe power data in Fig. 4.6, we fit the ring-up curve with the solution of the optical Bloch equation starting with $\rho(t=0) = |0\rangle\langle 0|$:

$$\rho_{ee}(t) = \frac{1}{2} - \frac{\gamma^2}{\gamma^2 + 8\omega^2}\left[1 + \frac{4\omega^2}{\gamma^2} e^{-3\gamma t}\left(\cos\chi t + \frac{3\gamma}{\chi}\sin\chi t\right)\right]. \tag{4.19}$$

Here $\chi \equiv 2\sqrt{\omega^2 - \gamma^2/4}$; the fit to the data yields $\omega = 2\pi \times 245$ kHz, corresponding to the observed π-pulse time of approximately 0.65μs, corrected for the rapid decay $\gamma = 2\pi \times 325$ kHz.

This ω should be compared to the Rabi frequency Ω_p predicted based on the cavity driving, which we extract from the incident photon rate, R_{inc}:

$$\Omega_p = \sqrt{\frac{R_{inc}}{4\tau}\sqrt{T_{EIT}/T_{CAV}}}. \tag{4.20}$$

At the highest power, $R_{inc} = 21$ MHz, yielding $\Omega_p = 2\pi \times 261(40)$ kHz, within $\sim 2\sigma$ of the measured value above.

Fig.4.6a shows the detuning dependence of the ring-up process, exhibiting rapid, detuned Rabi oscillations away from the dark-polariton resonance, and slower oscillations on-resonance. Fig. 4.6b shows the ring-up dynamics on the dark polariton resonance for various probe intensities. We observe Rabi oscillations between zero and one dark polaritons at the highest intensities, indicative of a strongly blockaded, zero-dimensional dot interacting with many photons within the polariton lifetime. The dark polariton oscillations exhibit a Rabi

frequency of $\Omega_{polariton} = 2\pi \times$ 245 kHz, in agreement with a first-principles calculation based upon the probe power . Note that the fast ∼100 ns oscillations arise from off-resonant excitation of non-interacting bright polaritons.

4.5.3 Isolate the Dark Polariton Dynamics

Strong interactions should cause the number of dark polaritons in the dot to saturate at large probe powers. However, the steady state transmission does not show a saturation effect in Fig. 4.6b plotting the transmitted photon rate before turning off the probe laser. The reason for the high steady-state leakage rate is that the transmitted photons are comprised of both dark polariton and off-resonantly excited bright polaritons. At high probe power, since the dark polariton transmission should be saturated, so the detected photons are overwhelmed by the bright polariton branch.

To see this is indeed the situation, we turn to look at the ring-down dynamics of the transmitted field shown in Fig. 4.6b. After the probe laser is turned off, instead of having a single exponentially decaying transmission, a sharp count rate drop at the begining of the ring-down can be observed in the high power traces. The transmission for all power settings then show a slow exponential decay, and the ones for the high probe power seems to be overlapping with each other. The fast decay is coming from the bright polaritons leaking out of the cavity, while the slow one portraying the dynamics of the dark polariton.

In Fig. 4.6c, we plot the ring-down part in log scale and normalize the transmission with the empty cavity transmission for each probe power. It is clear that all the dark polariton decay shares the same time scale which is much slower than the empty cavity decay represented by the solid gray line. Since the slow decay purely reflects the dynamics of dark polariton, we can thus use this effect to extrapolate the zero-time *dark* polariton numbers.

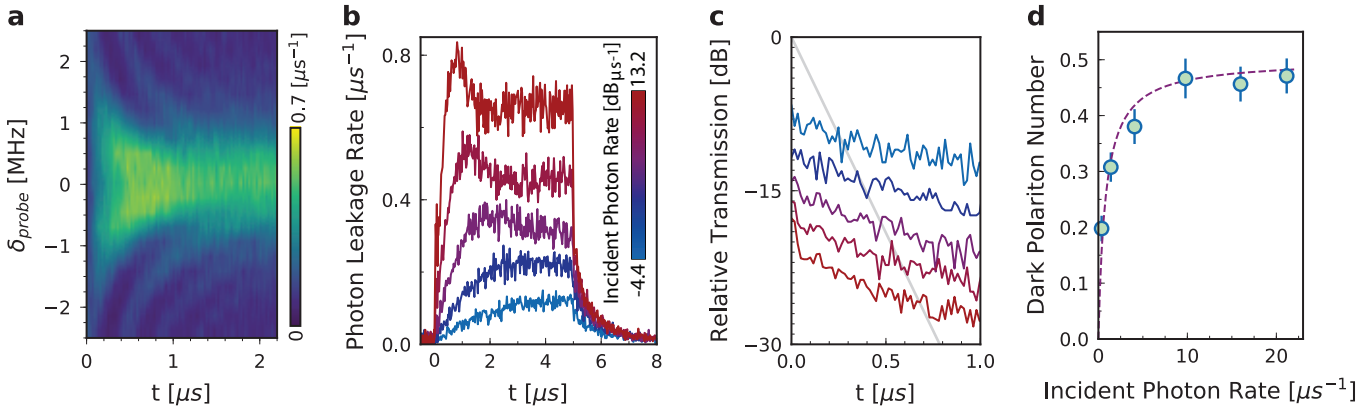

(a)

Figure 4.6: **Dynamical Evolution of a Polaritonic Quantum Dot: Ring-up and Ring-down.** When the dot is simultaneously excited with many photons within the dark polariton lifetime, these photons stimulate coherent tunneling of a polariton into and out-of the dot until the dot finally equilibrates. **(a)** We drive the resonator near the dark polariton resonance for 2.5 μs and record the transmitted intensity during the equilibration process. As probe frequency is tuned away from the resonance, the oscillation frequency increases and the visibility decreases, resulting in a "chevron" of damped Rabi oscillations. **(b)** With increasing probe strength, the overall transmitted power increases as well as the frequency of the occupation oscillation. The slow dynamics ($\sim$ μs timescale) reflect the tunneling oscillations between zero and one dark polaritons, while the fast dynamics (on a $\sim$ 100 ns timescale) reflect off-resonant excitation of the broad bright polaritons. Bright polaritons are weakly interacting and do not saturate with increasing probe power. Accordingly, they produce a dominant background at the highest probe powers (nearly 50% of the observed signal). **(c)** To isolate the physics of the dark polariton saturation from the bright polariton background, we explore the ring-down of the polaritons once the probe field is removed. The first $\sim$ 100 ns of ringdown is dominated by the fast decay of bright polaritons. At later times, the cavity leakage is dominated entirely by the dark polaritons, with a lifetime substantially longer than the bare resonator (gray curve). The color-code is the same as panel **b**; the relative transmission drops as the incident photon rate increases due to the blockade. **(d)** We extract the steady-state dark polariton number by extrapolating the slow decay of cavity emission to the beginning of the ring-down. The dark polariton number saturates strongly at the highest probe power to $n_D = 0.47(3)$

Calculation of Dark Polariton Number

In the ring-up and ring-down of the dot, the contributions of dark and bright polaritons mix in the observed resonator transmission. This is because the Rydberg-like dark polariton is only weakly coupled to the resonator field, so the resonator drive-power necessary to excite it will off-resonantly excite bright polaritons, which are then much more likely to emit into the resonator due to their light-like nature. This effect can be suppressed by increasing the control field intensity, thereby making the dark polariton more light-like and thus more efficiently generated and read-out, increasing the atom number, to increase the bright-polariton detuning, or by detecting the dark polaritons directly through blockade-enhanced imaging [56].

In the present situation, to extract the dark polariton number we first isolate the dark- and bright- polariton contributions to the cavity leakage field by harnessing the fact that the bright polariton decays more rapidly. We thus wait for the bright polaritons to decay away, and fit the remaining long-time cavity ring down tail to a decaying exponential:

$$R_P(t) = R_P(0)e^{-t/\tau_D} \tag{4.21}$$

where $R_P(0)$ is the extrapolated zero-time photon leakage rate and τ_D is the lifetime of the dark polariton. With an arbitrarily narrow Rydberg state, the dark polariton can only decay through the photon channel, and the EIT transmission should be 100% of the empty cavity transmission. However, in a real experiment, the Rydberg state has a finite lifetime which allows the dark polariton to decay without emitting a cavity photon. This results in the reduction of EIT transmission. We can then convert the photon leakage rate to polariton decay rate using

$$R_D = \frac{R_P}{\sqrt{T_{EIT}/T_{CAV}}} \tag{4.22}$$

where T_{EIT} and T_{CAV} are the EIT and empty cavity transmission at the same probe power.

The steady state dark polariton number is then obtained using

$$n_D(0) = R_D(0) \times \tau_D. \tag{4.23}$$

Note that the long-time tail would not reflect the simultaneous presence of multiple dark polaritons in the cavity, which would have already decayed rapidly due to their interactions . However, the steady state number we calculate remains valid because multiple occupation is strongly suppressed by blockade.

A second way to calculate the dark polariton number is to calculate the extrapolated zero-time *photon* number and map it onto the dark polariton number via the dark state rotation angle.

$$n_D = \frac{R_P}{\kappa \cos^2(\theta)} \tag{4.24}$$

where R_P is the steady state rate of photons emitted from dark polaritons obtained from Fig. 4(c), $\kappa = 2\pi \times 1.55$ MHz is the cavity linewidth, and $\cos^2(\theta) = \frac{\Omega^2}{G^2+\Omega^2}$ is photonic fraction of the dark polariton. However, the dark state rotation angle θ is obtained by fitting the EIT spectrum with a ideal three level system with only homogeneous broadening. The two EIT resonant peaks (see SI indicates that our system is more complicated than the simple three-level and thus the fitted rotation angle is oversimplified for calculating the dark polariton number.

CHAPTER 5

TOPOLOGICAL INSULATING CIRCUIT

Global topological features arise in a variety of contexts from knotted vortices in classical fluids [57] and superfluids [58] to anyons [59] in quantum wires [60], topological insulators [61], and 2DEGs [62]. In a condensed matter context, such "topologically protected" properties include single-particle features of the band-structure and many-particle ground-state degeneracies, with the latter typically emerging from the former in conjunction with strong interactions. To explore the nature of topologically-derived material properties, it is desirable to develop materials that not only support conserved topological quantities, but which may be precisely produced, manipulated, and probed. The aim, then, is to realize material test-beds that marry favorable coherence properties, strong interactions, and topologically non-trivial single-particle dynamics.

Meta-materials, where interaction strengths and length scales can be engineered, are a promising avenue for studying topological physics. Efforts are ongoing to produce the requisite topological single-particle dynamics in ultracold atomic gases [63–69], gyrotropic metamaterials [70, 71], and photonic systems [70, 72–79].

In cold atomic gases, gauge fields are generated either through spatially dependent Raman-coupling of internal atomic states [63, 67], or time- and space- periodic modulation of lattice tunneling rates [68, 80, 81]. In the optical domain, synthetic magnetic fields were realized via strain of a honeycomb lattice [82]. A Floquet topological insulator [83, 84] was realized under a space-to-time mapping of an array of tunnel-coupled waveguides modulated along their propagation direction [74]. A photonic topological circuit was realized through an array of off-resonantly coupled silicon optical ring resonators [75, 76, 79], similar to a proposal to couple Bragg stacks [72]. Time-reversal broken topological metamaterials have been realized in the microwave domain via a lattice of chiral magnetic (gyrotropic) resonators [70, 71]. Recently, topological invariants have been measured for an individual [85,

86] and pair of [86] superconducting qubits, as well as a two-site RF network with periodic boundary conditions [87].

In this work, we present and experimentally characterize the first RF circuit exhibiting a time-reversal symmetric topologically non-trivial band-structure. Our approach shares features with a number of the aforementioned proposals and experiments. Uniquely, the gauge field is realized through permuted couplings rather than phase shifts. Furthermore, we are able to temporally- and spatially- resolve the spin-filtered dynamics at the single-lattice-site level, and employ non-local couplings to realize a Möbius topology.

Our lattice may be viewed as a spin- dependent gauge field for RF photons in a network of capacitively-coupled inductors, where the spin state is encoded in two equivalent inductors on each lattice site. The simplicity of the approach points the way to straight-forward implementations of spin-orbit coupled quantum wires, fractional quantum hall systems, and proximity-coupled TI-superconductors, all within the circuit QED framework [88].

The text of this chapter is based on the publication [89] which the author made the major contribution.

5.1 From Harper-Hofstadter to Lattice Spin-Hall

5.1.1 The Harper-Hofstadter Model, and Breaking Time-Reversal Symmetry

When a massive particle is placed in a periodic 2D potential (lattice), its energy-momentum dispersion is modified by the lattice, forming bands of allowed and forbidden energies. Similarly, when a massive charged particle is placed in a uniform magnetic field, flat bands of allowed and disallowed energies, called Landau-levels, are formed. When both a lattice and a magnetic field are applied to a massive charged particle, the bands induced by the magnetic field and lattice compete- the resulting fractal band structure, as a function of magnetic field

Figure 5.1: (a) Hofstadter's butterfly: This figure shows the spectrum of allowed energies (vertical axis) versus magnetic flux per plaquette (horizontal axis), for a square lattice with uniform flux. (b) A particular gauge-choice for the Harper-Hofstadter model at a flux per plaquette of 1/4, corresponding to a geometric phase of $\pi/2$ acquired for tunneling counter-clockwise around a single plaquette. In the chosen gauge, all vertical tunneling has phase zero, and horizontal tunneling accrues of phase of $j\pi/2$, where j is the row. Because this phase is periodic every four sites, the new expanded unit cell, shown in red, is four sites tall.

strength and energy, is known as the Hofstadter butterfly, and is shown in (Fig. 5.1). The basic story is that if the magnetic field induces free-space cyclotron orbits whose area is a fully reduced rational P/Q lattice cells, then the band structure exhibits Q distinct bands (Fig. 5.1). Equivalently, in the presence of a magnetic field, the system becomes periodic every Q unit cells [90]. This may be seen by writing out the tight-binding Hamiltonian, using the Peierl's substitution [90]:

$$H_{\text{Hofstadter}} = -t \sum_{m,n} a_{n,m} \left(a^{\dagger}_{n,m+1} + a^{\dagger}_{n,m-1} + a^{\dagger}_{n-1,m} e^{im\phi} + a^{\dagger}_{n+1,m} e^{-im\phi} \right) \tag{5.1}$$

where t is the nearest neighbor tunneling rate, and $\phi = 2\pi P/Q$ is the magnetic flux per plaquette. It is clear that the new magnetic unit cell is Q lattice sites tall, as the exponential factor repeats ever Q lattice sites. The difficulty in implementing this Hamiltonian for uncharged particles, which thus do not respond directly to magnetic fields via a Lorentz force, is that $H_{\text{Hofstadter}}$ is not invariant under time reversal. This can be seen explicitly by verifying that the complex conjugate of $H_{\text{Hofstadter}}$ is not the same as $H_{\text{Hofstadter}}$ due to the complex exponential terms. Such a time-reversal asymmetric terms require something beyond inductors and capacitors (or equivalently, waveguides) to implement; possible approaches include periodic modulation [74, 83, 84, 91, 92] and coupling to materials with handed susceptibility induced by real magnetic fields [70].

5.1.2 Using Spin-Orbit coupling to recover Time-Reversal Symmetry

The simplest way to recover time-reversal symmetry is to add a second spin state that experiences the opposite magnetic field. Such physics typically arises due to Rashba or Dresselhaus spin-orbit coupling, after an appropriate gauge transformation and Peierls substitution [90]:

$$H_{\mathrm{SOC}} = -t \sum_{m,n} a_{n,m}(a^{\dagger}_{n,m+1} + a^{\dagger}_{n,m-1} + a^{\dagger}_{n-1,m} e^{im\phi S_z} + a^{\dagger}_{n+1,m} e^{-im\phi S_z}) \tag{5.2}$$

The key point is that in the spinor model, the anti-unitary time-reversal operator not only takes a complex conjugate of the Hamiltonian, but also flips spins. Under such an operation it is clear that H_{SOC} is time-reversal invariant.

What this does not yet tell us is how to engineer a spin that flips under time-reversal. It turns out that for any system of two degenerate energy levels, there is a basis $(0, 1)$ for which the basis-states are invariant under time-reversal, and a basis $(\uparrow, \downarrow)$ for which they swap.

The above can easily be seen using our experimentally realized system as an example: consider an excitation that may live in either of two resonant circuits A or B, as in the main text. In this case, reversing time certainly does not move the excitation from resonator A to resonator B. Thus the basis (0,1)=(A,B). By contrast, if we choose an excitation that is in a rotating superposition of the two resonators, $(A \pm iB)/\sqrt{2}$, reversing time corresponds to taking a complex conjugate or equivalently reversing the rotation direction, and thus swaps the excitation. Thus $(\uparrow, \downarrow) = (A \pm iB)/\sqrt{2}$. This may also be seen by noting that the time-reversal operator is a unitary matrix times a complex conjugation operator [93] .

What we have shown is that a pseudo-spin degree of freedom may be engineered using simple, time-reversal-invariant linear components; the spin "flips" under time-reversal in an appropriately chosen basis. What remains, then, is to engineer an effective magnetic field that acts oppositely on the two spin states. All we have shown so far is that this should be

possible without violating time-reversal symmetry, as the entire target system is time-reversal invariant.

Put another way- in the basis of the up- and down- pointing spins, the Hamiltonian will supply a time-reversal-symmetry breaking magnetic field to each spin state, corresponding to a Lorentz force. However, because the up- and down- pointing spin states themselves are time-reversal breaking quantities, the whole Hamiltonian does not violate time-reversal symmetry. This hints at the possibility perhaps such a Hamiltonian can be engineered from entirely linear, reciprocal components.

5.2 Topological Band Theory of Circuits

5.2.1 Dispersion Relation of 1D Transmission Line

The most simple and well known dispersion relation of microwave photons is the 1D transmission line. A lumped element model with only passive components (inductor and capacitor) can be used to simulate the light transport inside a coaxial cable with a pretty accurately prediction of the linear dispersion. This indicates the fact that information travels down the transmission line with a constant velocity $v = c/n$, where c is the speed of light in vacuum and n is the index of refraction of the transmission line. Fig. 5.2a depicts the circuit model of a lossless transmission line, where the capacitor value is the given capacitance per unit length of the transmission line, and the inductor value is given by the inductance per unit length of the transmission line. We consider the more familiar case of sites that are grounded on one side (Fig. 5.2a). To calculate the dispersion relation, we first work in the Fourier domain and apply the Kirchoff's current law at each node:

$$\frac{V_i - V_{i+1}}{Z_L} + \frac{V_i - V_{i-1}}{Z_L} + \frac{V_i}{Z_C} = 0, \tag{5.3}$$

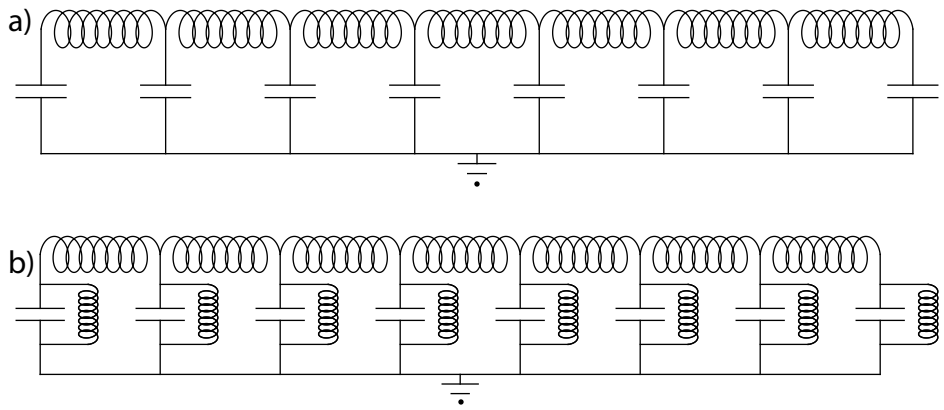

Figure 5.2: **Lumped Element Model for Transmission Line. (a)** A grounded lumped-element model of a transmission line, with light-like dispersion at low-momenta, and a cutoff at a quasi-momentum given by the inverse of the inter-site spacing. **(b)** A grounded lumped-element model of a tight-binding lattice.

where V_i is just the voltage at node i, with Z_L and Z_C being the impedance of the coupling inductor and on site capacitor. Since the periodic nature of the system, it is then straight forward to use the Bloch's theorem and substitute V_{i+1} (V_{i-1}) with $V_i e^{jk}$ ($V_i e^{-jk}$) and obtain the anticipating phonon like dispersion

$$\omega = \sqrt{\frac{2}{LC}}\sqrt{1-\cos k}. \tag{5.4}$$

This linear dispersion at low momentum, reflecting the behavior of its continuum counterpart. As the momentum approaches the wave-vector of the lumped elements, the dispersion levels off: $\omega = 2\omega_0 \sin(q/2)$, with $\omega_0^2 = 1/LC$, with L and C the lumped inductance and capacitance respectively, and q the quasi-momentum in units of inverse lumped element sites.

Massive vs Massless Photons

One way to recover the massive dispersion relation is to have an parallel inductor across the capacitor, forming a resonator on each site. In this case the system behaves not as a transmission line, but as a string of coupled resonators. These resonators have a "rest-mass"

of $\omega_{\text{res}}^2 = 1/(L_{\text{site}}C)$ that rounds out the dispersion at low quasi-momenta, imbuing the photons with a mass:

$$\begin{aligned}\omega &= 2\omega_0\sqrt{\frac{L}{4L_{\text{site}}} + \sin^2(q/2)} \\ &\approx 2\omega_0\left(\frac{L}{4L_{\text{site}}}\right)^{1/2}(1 + \frac{L_{\text{site}}}{L}\sin^2(q/2)).\end{aligned} \tag{5.5}$$

in the limit $L_{\text{site}} \ll L$.

The width of the band is then $4\omega_0(L_{\text{site}}/4L)^{1/2}$. In a tight binding lattice the bandwidth is $4t$, where t is the nearest-neighbor tunneling rate. Thus we can now identify the tunneling rate as $t \approx \omega_0(L_{\text{site}}/4L)^{1/2}$.

Right- vs Left- Handed Circuits

It is more preferable to use the capacitors for coupling between different site and inductors as the on-site component for few practical reasons: (1) The scheme we are going to use to generate the non-trivial topology requires more coupling components than the on-site ones, and the loss of an LC circuit is dominated by the resistive loss in the inductor. So the performance of circuit, particularly for the pulse transport described in section 5.6, will benefit from reducing the overall number of inductors. (2) The physical size of an inductor is much bigger than the capacitor, so by employing fewer inductors, we are able to have more sites per unit physical area. (3) We are driving/probing the circuit using coils that couples to the inductor which is easier than measuring the voltage across the capacitor.

In order to see how this subsitution affect the dispersion relation, we can first look at the general solution of Eq. 5.3:

$$\frac{Z_{couple}}{Z_{site}} = 4\sin^2\frac{k}{2}. \tag{5.6}$$

With this more general frequency-dependent expression in hand, it is clear that swapping inductors and capacitors in these circuit networks is equivalent to sending $\omega \to \omega_0^2/\omega$ in

the dispersion relation; such left handed transmission lines are well-studied [94], and their extension to two-dimension will be employed later in this work, in our discussion of the full topologically insulating circuit.

Grounded vs Symmetrical Networks

It also bears mentioning that up to this point we have treated the on-site impedance network as grounded on one side; Fig. 5.3 depicts the circuit symmetrically, without grounding, and indeed such a setup results in quantitatively identical behavior once Z_{site} is replaced by $Z_{\text{site}}/2$: The symmetrical case admits both even and odd solutions: the even solutions are all at zero frequency, corresponding to a DC shift at various quasi-momenta, and hence may be ignored, while the odd solutions are the same as those reached in the grounded circuit network. The symmetrical generalization will become important in the 2D system, where the sign of a site-to-site coupling may be reversed (made negative) by connecting the positive end of one site to the negative of the other, and vice-versa; in 1D such a choice can always be gauged away; not so in 2D: this is the origin of the spin-hall effect in our lattices.

5.3 Braiding the Gauge Field

5.3.1 Recap on Geometric Phase: Aharonov–Bohm effect

A crucial ingredient in a topological insulator is the non-trivial geometric phase. In a solid state system or 2DEG, this is realized by applying a external magnetic field or spin-orbit coupling. Obviously, such scheme does not apply to a photonic meta-material since photons are neutral particle and do not couple to the magnetic field. In the optical domain, we are able to engineer the topology following the map between Coriolis force in a rotating frame emerged from twisted cavity and Lorentz force in the two-dimensional plane. In a lattice system, I'd like to understand the effect of a magnetic field from a different perspective-the geometric phase, and its analogy to Aharonov-Bohm effect.

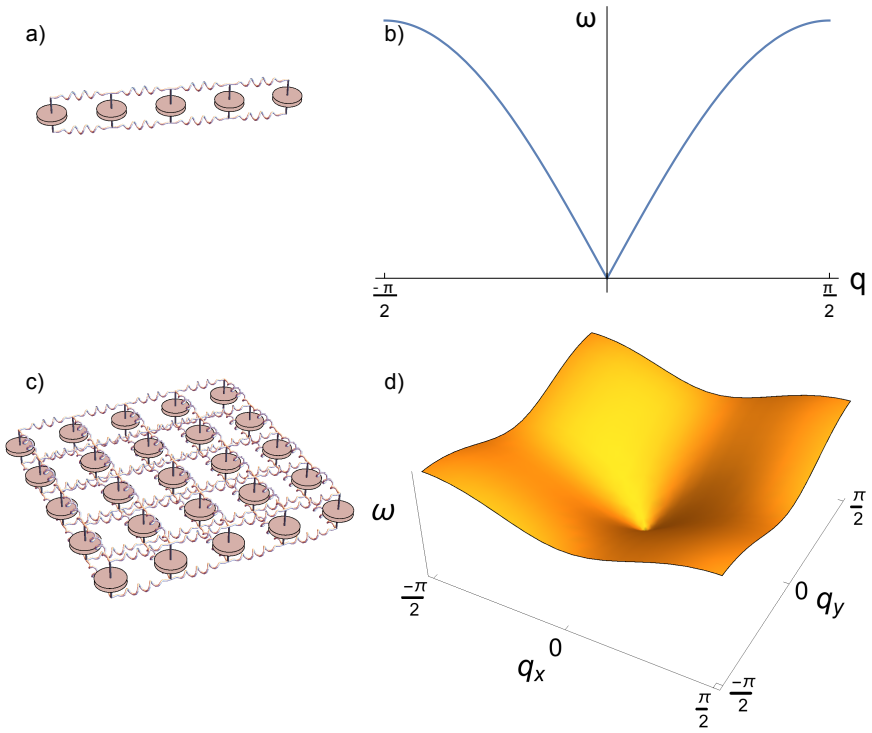

Figure 5.3: **A 2D Symmetric Circuit. (a)** In the lumped-element model of a transmission line, the capacitance per unit length is modeled with an actual capacitor, and the inductance with an actual inductor. **(b)** This system has a linear (light-like) dispersion at low momenta, rolling off at a momentum given by the spacing of the lumped-elements. This roll-off reflects the fact that a the lumped-element system behaves differently the continuous transmission line once the dynamics probe the discreteness of the lumped-element system (absent in the continuous system). **(c)** The two-dimensional extension of this model exhibits (conical) light-like 2D dispersion **(d)**. For symmetry with what follows, we draw double-ended connections between the capacitors; the calculations in this section assume that the lower-side of the capacitors are grounded.

In quantum mechanics, it is well known that the gauge field is an physical observable that can be measured by extra phase gained by a particle moving in a close loop with non-zero flux enclosed within it. In a lattice system, this is represented by modifying the transnational symmetry of the lattice: If one perform the transformation of moving the wave function along a single plaquette, instead of recovering to its original form, an extra phase shows up if the flux encircled by one plaquette is not a integer of 2π. By picking a particular gauge, one can rewrite the tunneling term in a tight binding Hamiltonian with a complex number saying that the particle going through that tunneling will acquire extra phase as mentioned in section 5.1. As for a spin-Hall system, the time-reversal-symmetry is restored by expanding the system with spin degree of freedom. The complex tunneling terms then should have the form of a spin-orbit coupling in which opposite spins experience opposite sign of geometric phase.

5.3.2 Adding the Spin Degree of Freedom

It is now For a spin-Hall system, the Z_2 symmetry requires the circuit to have the spin-degree of freedom. We simply make a second copy of the 2D lattice structure: now there are two capacitors on each site, which we will label A and B or red and blue, and initially A capacitors are coupled to A capacitors by inductors, and B capacitors to B capacitors by another set of inductors and no A-B couplings, as in Fig. 5.4. Because the A and B sublattices are uncoupled, the dispersion relation is the same as a single-spin-state 2D lattice, with a two-fold degeneracy. The excitation in the lattice can then be represented by a normalized two component complex vector (V_A, V_B), with V_A and V_B as the voltages across inductor A and B respectively, in the frequency domain. With this spinor-like object, any excitation localized on a lattice site can be projected onto this two-level system by

$$\mathbf{V_i} = \cos\theta \mathbf{V_{A,i}} + \mathbf{e}^{\mathbf{i}\phi} \sin\theta \mathbf{V_{B,i}}, \tag{5.7}$$

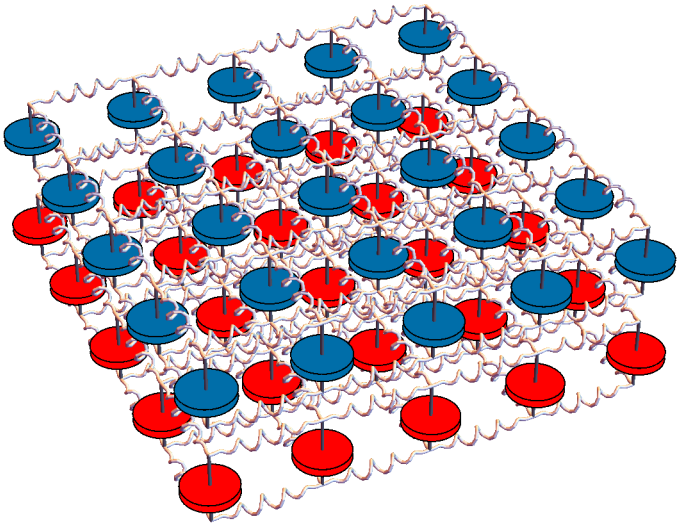

Figure 5.4: Two-spin 2D photonic waveguide realized with discrete components. A photon in state A lives in the red lattice of capacitors, and a photon in state B lives in the blue lattice. The A- and B- lattices are uncoupled from one another.

where $\mathbf{V_{A(B),i}}$ is the excitation in $A(B)$ inductor on lattice site i.

5.3.3 Braiding the Topology

In this subsection, I will show how the complex tunneling term can be realized by cross coupling between the A and B inductors, resulting in a rotation of the Bloch vector. As a simple example, I will track an excitation starting from the top left lattice site $\mathbf{V_0} = (\mathbf{1}, \mathbf{0})$ in Fig. 5.5 and following the path along the yellow arrows. Three of the four tunneling are zero phase trivial connection the same as in a transmission line described in the previous sections. The third tunneling, in the Landau gauge, will generate a $\pi/2$ phase. Here we first swap the connection between the A and B inductor so that $\mathbf{V_A} \rightarrow \mathbf{V_B}$. Further more, we cross the wire for the $B \rightarrow A$ connction, and $\mathbf{V_B}$ becomes $-\mathbf{V_A}$. After moving the signal around this close loop, the initial excitation in inductor A is transfered to inductor B with a negative sign.

To see how this transformation is equivalent to a $\pi/2$ phase shift, we can write the

operation as $-i\sigma_y$ applying to V_0, and the remaining operation for0, π and $3\pi/2$ tunneling can also be written as $(i\sigma_y)^0$, $(i\sigma_y)^2$ and $(i\sigma_y)^3$. Henceforth, if we redefine the base vector of the excitation as $\uparrow,\downarrow = (\mathbf{A} \pm \mathbf{iB})/\sqrt{\mathbf{2}}$, the eigen-vector of σ_y operator, then after the same loop, $\uparrow$ becomes $i\uparrow$ and $\downarrow$ becomes $-i\downarrow$. Then with a four-row period (as in the Hofstadter model with $p = 1$, $q = 4$), we ensure each plaquette encircles $\pi/2$ flux.

5.3.4 Band Structure

To compute the band-structure of the lattice, we consider a single "extended" (magnetic) unit cell containing a full flux quantum, which at a flux per plaquette of 1/4, is a 1×4 strip of sites. We employ a circuit analog of Bloch's theorem, which amounts to a wave-function ansatz which is identical from one extended unit cell to the next up to a factor of $e^{\pm iq_x}$ in the $\pm x$ direction, and $e^{\pm iq_y}$ in the $\pm y$ direction. We can then apply Kirchhoff's laws to generate an admittance matrix $Y_{ij}(\omega, q_x, q_y)$ as a function of frequency and quasi-momentum. The mode frequencies are the roots of the determinant of Y, but computing these is computationally taxing, and will not provide the mode functions, which we will require for computation of the Chern numbers of the bands. A more general approach is to generate the equations of motion from Y. To this end we write $i\omega Y$ as a Laurent series in ω: $Y_{ij} = (1/i\omega L)_{ij} + i\omega C_{ij}$ It should be apparent (from the fact that Y gives the admittance between sites, which for a capacitor is $i\omega C$, and for an inductor is $1/i\omega L$) that C parameterizes the capacitive couplings, and L the inductive couplings. We can thus write the equations of motion in the time domain as: $\sum_{j,k} L_{ij}C_{jk}\ddot{V}_k + V_j = 0$

The mode frequencies are thus the square roots of the eigenvalues of the matrix $(LC)^{-1}$, and the bloch wavefunctions are the corresponding eigenvectors. The numerically calculated band energies are plotted vs quasi-momenta q_x and q_y in Fig. 5.6.

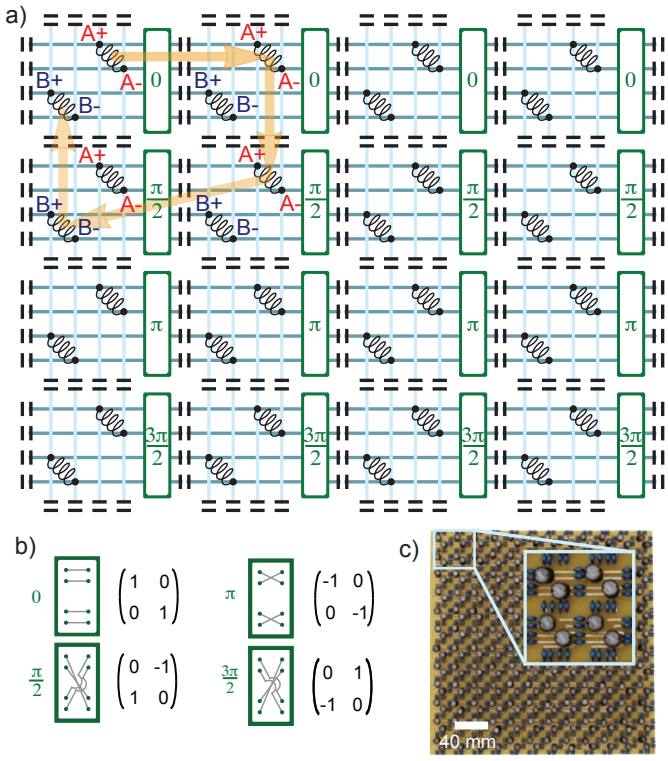

Figure 5.5: **Circuit Topological Insulator. a.** Circuit topological insulator schematic. The periodic structure is formed by onsite inductors and coupling capacitors, (black) that are connected via a latticework of wires (light and dark blue lines). At each lattice site, the two inductors "A" and "B" correspond to right and left circularly polarized spins. When a photon traverses a single plaquette (indicated in orange) it accumulates a Berry phase of $\pi/2$. The phase is induced by braiding (indicated by the green boxes and specified in b) of the capacitive couplings. **b.** Structure of the coupling elements between lattice sites. Each row shows one of the four rotation angles implemented by the capacitive coupling in the circuit. The rotation angle (left column) is induced by connecting inductors as shown (middle column). The corresponding rotation matrices (right column) indicate the inductors being coupled, as well as the signs of the couplings. **c.** Photograph of Circuit Topological Insulator. The inductors (black cylinders) are coupled via the capacitors (blue); circuit topology is determined by the trace layout on the printed circuit board (yellow). Inset: Zoom-in on a single plaquette consisting of four adjacent lattice sites.

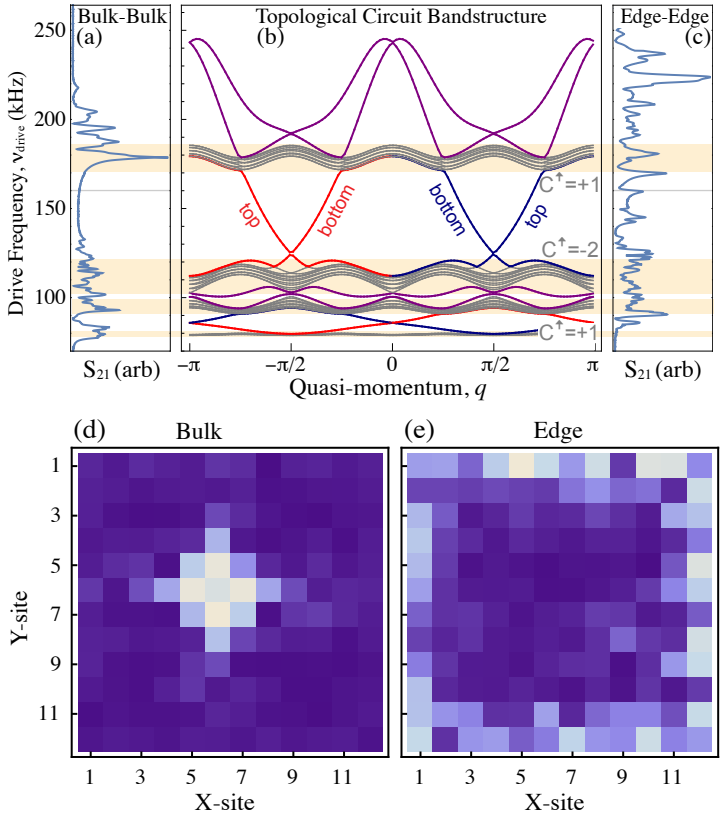

Figure 5.6: **Site-Resolved Measurement of Band-Structure and DOS. a.** The experimentally observed coupling (linear scale) between two points in the bulk of the circuit TI (blue) with the bulk states indicated (orange bands). **b.** Band Structure of a Circuit TI. A strip of circuit TI with fixed boundary conditions in the transverse direction is numerically diagonalized at finite longitudinal quasi-momentum q, yielding four massive bulk bands (gray), and spin-orbit-locked edge states (red=↑, blue=↓) that reside in the bulk gap. Labels of "top" and "bottom" denote the boundary that each edge mode propagates along (with opposing group velocities $d\omega/dk$). The spin-Chern numbers ($C^{\uparrow}$) of the spin-up bands are indicated next to each band ($C^{\downarrow} = -C^{\uparrow}$). The additional edge modes (indicated in purple) are not topologically protected. The highest energy edge-channel is localized to a single site along one direction, while the middle and lowest edge-channels are localized to two and three sites respectively. **c.** Experimentally observed coupling between two sites on the edge of the circuit, showing transmission through edge modes even within the bulk gaps. The structure within the gaps is to be expected, as the system is finite so the edge exhibits Fabry-Pérot resonances. **d.** Experimental site-resolved response to excitation at a central lattice site, within the band gap at 160kHz, showing bulk localization. e. Experimentally observed, site-resolved edge-mode structure at 160 kHz. The arrows in a. and c. reflect the frequency of excitation in b. and d.

Computing Band Chern Numbers

To numerically compute the Chern numbers of each of the up- and down- spin bands, we employ a gauge-independent definition of the Chern number:

$$C_b^{\uparrow,\downarrow} = \frac{1}{2\pi i}\int\int_{BZ} Tr\left(\rho^{\uparrow,\downarrow}\left[\frac{d\rho^{\uparrow,\downarrow}}{dq_x}, \frac{d\rho^{\uparrow,\downarrow}}{dq_y}\right]\right) d^2q$$

with $\rho^{\uparrow,\downarrow}(q) \equiv \sum_b \left(\psi_b^{\uparrow,\downarrow}(q)\right)^\dagger \left(\psi_b^{\uparrow,\downarrow}(q)\right)$.

Here the sum over b runs through the bands under consideration: For the top and bottom bands, we compute their Chern numbers C_1 and C_4 independently. Because the middle two bands (2 and 3) touch (at Dirac points), their Chern numbers cannot be computed independently, so we must compute $C_{2,3}$ as a single entity. The above definition of the Chern number follows from the standard definition in [95] after a bit of algebra.

The $\psi_b^{\uparrow,\downarrow}(q)$ are the eigenvectors extracted from the band structure calculation in the previous section, with the added complication that we must project onto a single-spin subspace. To this end we compute eigenvectors and eigenvalues of $P^{\uparrow,\downarrow}(LC)^{-1}P^{\uparrow,\downarrow}$, with $P^{\uparrow,\downarrow} \equiv \frac{1}{2}\sum_l (A_l \pm iB_l)(A_l^\dagger \mp iB_l^\dagger)$, the projector onto the up- (down-) spin subspace. Here the A_l (B_l) are the state vectors corresponding to a voltage exclusively at the A (B) sub-lattice of site l.

It is worth noting that we have intentionally avoided bra-ket notation, typically employed in defining and computing Chern numbers; this was done to emphasize that all of the topological properties of the bands studied here are classical- the physics applies equally well to individual particle quantum wave-functions as to classical fields.

Calculating the Mode Structure of an Infinite Strip

The full 2D band-structure of a 2D system cannot exhibit edge-states, as the system has no edges! To study the properties of the edge states, we investigate the mode-structure of a strip of finite width, but infinite length; the top and bottom of the strip will now support

edge modes, at the cost of projecting the resulting band-structure into one dimension.

To compute the spectrum of modes of our infinite strip, we employ the tools of the preceding section, but instead of diagonalizing a single magnetic unit cell with Bloch's theorem applied along both x and y, we only employ Bloch's theorem along x and consider a single strip of L unit cells along y with fixed boundary conditions at the top and bottom, defining the location of the edge. In practice this means that adjacent rows are assumed to be identical to the row under consideration, up to a factor of e^{iq_x}.

Fig. 5.6 shows a numerical diagonalization of the circuit modes of an infinite strip with 23 lattice sites in the transverse dimension, with definite spin and longitudinal quasi-momentum q. The four broad bands (gray curves in Fig. 5.6 correspond to the bulk response of the system, their breadth owing to the existence multiple transverse modes in the bulk. Spin-helicity coupled edge channels, characteristic of a topological band-structure, occupy the gaps between bulk bands. In the top-gap, $\uparrow$ excitations propagate leftward on the top edge and rightward on the bottom edge, while $\downarrow$ excitations propagate rightward on the top edge and leftward on the bottom edge. The direction of propagation may be ascertained from the slope of the energy-momentum dispersion. The locking of spin to propagation direction on each edge prevents backscattering in the absence of a spin flip disorder. As discussed in the SI, the topological character of each isolated spin-band may be formally characterized in terms of a spin-Chern number, which, for $\uparrow$ ($\downarrow$) bands is $+1(-1)$ for the top and bottom bands and $-2(+2)$ for the sum of the middle two bands, which touch at Dirac points and thus may not be characterized independently.

5.4 Making and Probing the Metamaterial

The topological meta-materials are composed of a room-temperature FR4 PCB, populated with 330pF capacitors with component-to-component scatter of $\pm 1\%$, and 3.3mH wire-wound inductors with scatter of $\pm 10\%$; this amounts to both spin-dependent and spin-

independent disorder, with the former arising primarily from differential variation between the two inductors at a lattice site, and the spin-independent disorder from common-mode variation between lattice-sites. All disorder may be decreased by employing stripline inductors and capacitor, and micro-fabrication technology. In this case inductors and capacitors may be swapped, to move from left- to right- handed transmission lines. Because of the reduced bandwidth in the massive model (see SI), the sensitivity of the meta-material to component-scatter would be worse for a model with resonators on each site rather than just inductors- this corresponds to the difference between massive- and light-like lattice photons.

To inject photons into a site, we inductively couple to a single inductor by placing a 5 turn, 8mm diameter drive coil over the onsite inductor that we wish to excite. This inserts photons in the A or B sites; to inject spin-polarized $\uparrow$ or $\downarrow$ photons for Fig 5.7, the two inductors on a site are simultaneously excited 90° out of phase by driving them with phase-locked synthesizers. Differential inductive in-coupling is compensated for by adjusting drive voltages on the two inductors. Spin-resolved detection is achieved by separate time-resolved detection of A and B sites, and transforming to the $\uparrow$ and $\downarrow$ states.

The Möbius topology is generated by employing a second PCB that provides the appropriate connections between the edges of the primary circuit TI PCB.

Numerical prediction of the steady-state frequency response is achieved by generating the admittance matrix of the circuit network and inverting it to compute the response to a drive. To calculate the band-structure, a coupled first-order system of differential equations representing the inductor-capacitor network was generated for a $1D$ strip 23 sites wide with fixed boundaries in the transverse direction, and periodic boundary conditions in the longitudinal direction, whose phase is set by the quasi-momentum q under consideration. The system of equations was numerically diagonalized with eigenvalues correspond to the system energies at the given quasi-momentum (see supplement for details).

5.5 Characeterizing the Metamaterial

5.5.1 Bulk and Edge excitation

The smoking gun of a topological band-structure is a gap in the bulk density of states within which spin-filtered edge-states reside [95, 96]. To probe this physics directly we excite the bulk of our meta-material (by driving an on-site inductor with a near-field coupled coil), and observe the response at other sites within the bulk (using a pickup coil). The resulting spectrum probes the RF density of states plus overlap factors reflecting the spatial mode profile at the drive- and measurement- locations. Fig. 5.6 shows a typical measurement, with the predicted locations of the bands overlaid in orange; a gap is clearly apparent in the data. In Fig. 5.6a, we excite a central site at an energy between the bands and perform site-resolved microscopy. The insulating nature of the bulk is revealed by the exponential localization of the response.

In Fig. 5.6c, we excite and probe the system on its edge. We observe a response within the energetic band gap, experimentally confirming the existence of mid-gap edge modes, and strongly suggesting their topological nature, which we confirm below. It bears mentioning that in spite of the absence of a Fermi sea (our excitations are photons, which are bosons), we still observe an RF- insulating bulk and a conducting edge; this is because we are directly probing the density of states of the system at the RF-drive frequency. Furthermore, the appearance of clear Fabry-Pérot resonances on the edge, rather than a continuous density of states, is indicative of the periodic boundary conditions imposed by the closed edge. Fig. 5.6e shows a site-resolved image of the edge mode at 160 kHz, demonstrating the persistence of the edge transport.

5.6 Topologically Protected Edge Propagation

Another important prediction of a topological insulator is the particles transported through the edge mode is protected against the non-magnetic defects. With Z_2 symmetry, the excitations in different spin will also propagates in opposite direction coming from the spin-orbit coupling.

5.6.1 Spin Resolved Pulse Measurement

To probe the transportation properties of the edge mode, instead of using a continues wave, we drive the circuit with pulses at particular edge mode frequencies residing in the bulk band gap. One advantage of this circuit approach is that injecting the pulse with definite spins very simple. This is done by driving both inductors in the same lattice site, but with $\pm 90^\circ$ phase lag, and fine adjusting the amplitude to compensate the differential coupling between the coil and the inductor. The reversed process is used to then perform the spin-resolved probe where we use two coil to probe both inductions on the edge site, and subtract the signal with one traces shifted in time for the appropriate phase.

5.6.2 Topologically Protected Edge Propagation

To demonstrate that the edge states are spin-orbit locked, we rapidly excite the A inductor on a single edge site at an energy within the highest energy gap, and perform a spin-resolved time-domain measurement of the propagating excitation. Because $A = (\uparrow + \downarrow)/\sqrt{2}$, the excitation splits, with the $\uparrow$ ($\downarrow$) component propagating left (right).

Fig. 5.7 shows the intensity at each lattice site around the system perimeter (yellow inset), as a function of time (increasing downwards), with red (blue) color channel indicating up (down) spin states. The splitting of the excitation, with red (blue) component moving left (right), demonstrates the spin-orbit locking of the edge states. The measured propa-

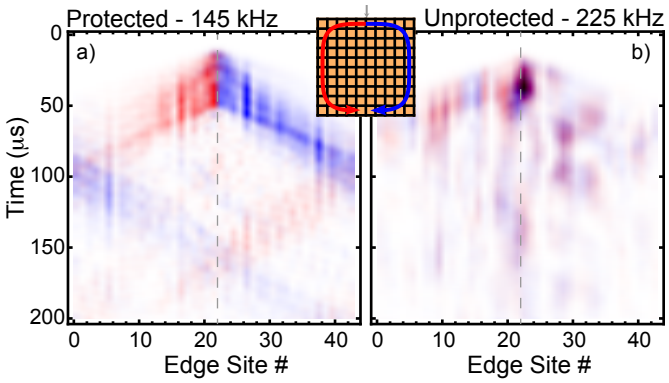

Figure 5.7: **Time-Resolved Transport Dynamics of the Edge Modes. a.** Spin-resolved detection of the splitting of a localized **A**-site = $(\uparrow + \downarrow)/\sqrt{2}$ excitation in the protected gap (at 145 kHz). The $\uparrow$ (red) and $\downarrow$ (blue) signals are overlaid, demonstrating spin-momentum locking. Two round-trips are visible; sites 0 and 42 are equivalent. **b.** Spin-resolved excitation after exciting the same site in the unprotected upper edge mode at 225 kHz, where disorder immediately leads to backscattering for both spin-states. Inset: Edge lattice-site numbering convention.

gation velocity of 4.3(3) sites/10μs is consistent with the predicted group velocity of 4.2(2) sites/10μs arising from the numerical band-structure calculation.

In contrast to the topologically protected edge modes between the third and fourth bands, the unprotected modes above the top band exhibit left- and right- propagating components for each of the top- and bottom- edges, for each spin state. Fig. 5.7b shows the same dynamics experiment as in Fig 5.7a, but this time exciting the unprotected edge modes. Not only do both up- and down- excitations propagate both left- and right-wards, but both are rapidly backscattered and localized by disorder. These unprotected, termination-dependent edge channels are similar to zig-zag edges of a graphene nano-ribbon [97].

CHAPTER 6

BREAKING TIME REVERSAL SYMMETRY

It is well known that time-reversal-symmetry (TRS) is not preserved in both the integer and fractional quantum hall system because of the externally applied magnetic field. In a synthetic material, the gauge field or the geometric phase is usually generated by a Rashba like spin-orbit coupling in which the symmetry between the forward and backward momentum state have opposite phase accumulation. In the non-planar cavity, the counter rotating manifold is associated with the backward propagating mode that has a geometric rotation with same helicity but opposite direction. However, this set of modes are being neglected for non-interacting photons since the mirror or air induced back-scattering is negligibly small, so as we only probe the cavity with a well defined direction, the two manifolds can be treated separately as two integer quantum hall system.

This picture might change when we couple the the cavity to the atomic sample because an atom-a single emitter- will couple to both forward and backward mode with equal strength and thus generate an atom induced back-scattering. This effect is dramatically suppressed when an ensemble of atoms with a length comparable to the wavelength is coupled to the cavity photon due to the phase matched collective excitation.

In the optical domain, Faraday effect is long been employed in optical isolators to break the time-reversal-symmetry, but the excessive single-pass loss makes it not suitable for being used in an optical cavity. In this chapter, I will show that with a polarized atomic sample, the Faraday rotation can be implemented for the cavity photon with low loss. Furthermore, this effect is preserved for dark polaritons even in which the linear susceptibility is cancelled.

The text of this chapter is based on the publication [98] which the author made the major contribution.

6.1 Symmetries in a Twisted Cavity

In a four mirror running wave cavity, even a single transverse mode of the resonator exhibits a four-fold degeneracy arising from the polarization-helicity degree of freedom, and the direction of propagation along the resonator axis (see Fig. 6.1). It will thus be necessary to break *two* symmetries to isolate precisely one of these modes: inversion symmetry and time-reversal symmetry.

To first break inversion symmetry we twist the resonator slightly (6°), resulting in a Pancharatnam polarization rotation of the intra-cavity field on each round-trip through the optical resonator (see Fig. 6.1). Similarly to a Dove prism or a periscope, the polarization rotation in a non-planar resonator results from the geometric rotation of any vector when parallel transported around a non-planar closed loop [99]. This rotation produces a splitting of 55.5 MHz between pairs of helicity modes H^+ and H^- which are nearly circularly polarized, with a small ellipticity arising from mirror-induced birefringence (see Fig. 6.1).

The key to breaking the remaining time-reversal symmetry is that helicity is defined with respect to the direction of light propagation, and not a fixed axis in space. Forward and backward propagating modes of the *same* helicity have *opposite* polarization, and thus may be split through the Faraday effect. In our experiment, this takes the form of coupling to an optically pumped atomic ensemble whose polarizability depends upon the incident light's polarization, *not* its helicity; the atoms are indifferent to the light's direction of propagation.

The symmetry breaking mechanisms employed by the atomic ensemble in the twisted the cavity can be understood by imagining a rod move into or out-of a hole in a plate (see Fig. 6.1c). A smooth rod respects helical symmetry since it can slide in and out without enforcing a specific rotation direction. Both movement directions are also allowed as result of preserved time reversal symmetry. Threading breaks the helical symmetry for the movement by forcing the rod to turn in a particular direction when moving longitudinally, just as the twisting does to cavity modes. Finally, the Faraday effect suppresses the back-propagating

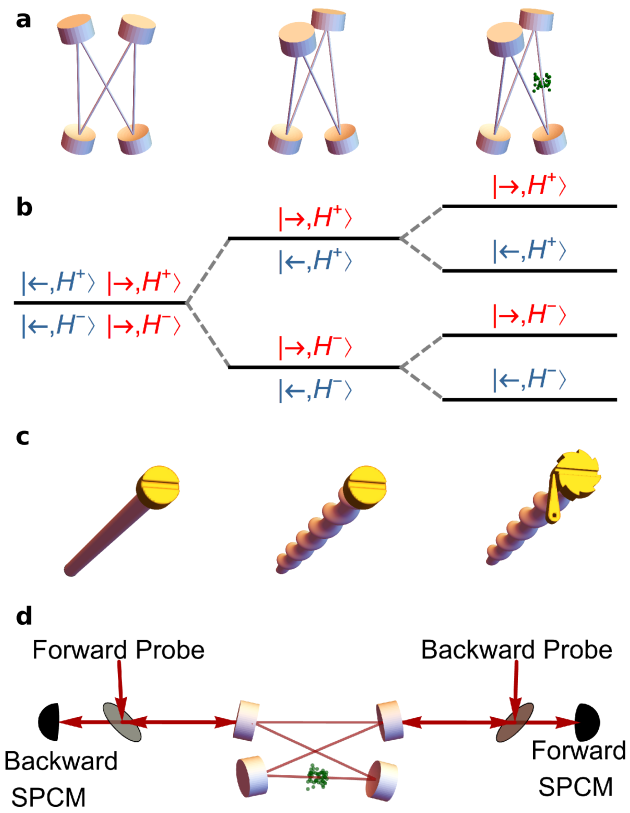

Figure 6.1: **T-Breaking in Twisted Resonators Coupled to Atoms**. In a birefringence-free planar resonator (**a**, left) each transverse mode exhibits a four-fold degeneracy that may be parametrized as forward (red right arrow) and backward (blue left arrow) propagation for each of positive and negative helicity (**b**, left): $\{\rightarrow, \leftarrow\} \otimes \{H^+, H^-\}$. Twisting the resonator breaks this four-fold degeneracy into two sub-manifolds of definite helicity (**a**,**b** middle). We couple the optical modes to spin-polarized atoms (a, right) to break the forward-backward symmetry (**b**, right): polarized atoms are sensitive not to the light's helicity (defined relative to the direction of propagation) but to its absolute polarization (defined relative to a fixed axis); the difference in oscillator strengths for σ^+ and σ^-, for ^{87}Rb atoms on the $|F_g = 2, m_F = 2\rangle \rightarrow |F_e = 3'\rangle$ transition of the D2 line, is a factor of 15 [100]. The Zeeman splitting of the magnetic sublevels does not directly contribute to T-breaking, except insofar as it is employed to optically pump the atoms. **(c)** A schematic of the particular symmetries broken in the various aspects of the experiment, using the analogy of moving a rod into/out-of a plate. **Left**: A smooth rod can move into- or out-of- the page. **Center**: a *threaded* rod must twist clock-wise to move into the page, and counter-clock-wise to move out of the page. **Right**: a *ratcheted threaded* rod may only rotate clockwise, and thus may only move into the page. **(d)** The experimental apparatus consists of a twisted resonator coupled to an ensemble of laser-cooled ^{87}Rb atoms (green spheres), and probed from both directions using laser fields injected through optical pickoffs (gray circles). The transmitted fields in both directions are detected through single photon counting modules (SPCMs) fiber-coupled to the light transmitted through the pickoffs.

mode with the same helicity, which is analogous to having a ratchet attached to a threaded rod to prevent backward motion.

6.2 A Narrow Band Optical Isolator

In this section, we demonstrate the time-reversal-symmetry breaking by probing the spectrum of the forward- and backward-propagating modes. Without the presense of the atoms, the non-planarity of the cavity breaks the four cavity modes into to helicity manifold. In the dispersive regime, the polarized sample further split the degenerate cavity modes with minimal transmission loss showing the breaking of remaining symmetry.

6.2.1 Experimental Setup

In this experiments, we load a cloud of ∼1000 ^{87}Rb atoms into the 12μm×11μm TEM$_{00}$ waist of a running wave optical resonator with a linewidth of $\kappa = 2\pi \times 1.5$ MHz and finesse of $F = 2500$. A bias field of ∼14 Gauss is then applied to the atoms along the resonator axis. The atoms are optically pumped into $\left|F_g = 2, m_F = 2\right\rangle$ using $\perp$ polarized light tuned to the $\left|F_g = 2\right\rangle \rightarrow \left|F_e = 2'\right\rangle$ transition of the Rubidium D_2 line detailed later. We achieve a maximal collective cooperativity $N\eta = 4G^2/(\kappa\Gamma) \approx 590$ and collective single-quantum Rabi frequency of $G_{\sigma^+} = 73$ MHz. Here N is the atom number, η is the single quantum cooperativity of the ^{87}Rb $\left|5S_{1/2}\right\rangle \rightarrow \left|5P_{3/2}\right\rangle$ transition [101], and Γ is the ^{87}Rb 5P$_{3/2}$ state spontaneous linewidth [100].

6.2.2 Optical Pumping

Our setup presents a unique optical pumping challenge: we would like to polarize our ^{87}Rb sample in the $\left|F_g = 2, m_F = 2\right\rangle$ magnetic sub-level, with the quantization axis defined along the resonator axis, a task that normally require sending resonant or near-resonant circularly-

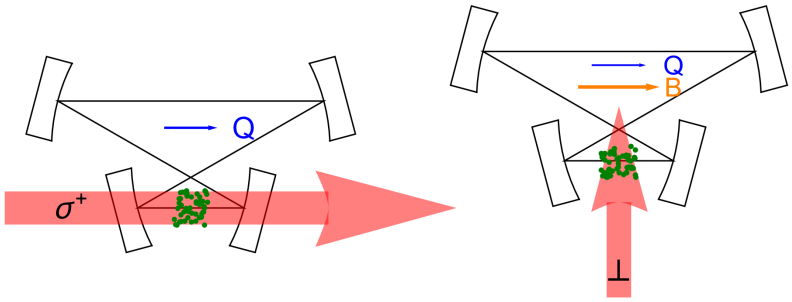

Figure 6.2: **Optical Pumping**. To break the degeneracy between helically polarized resonator manifolds, it is essential to achieve an atomic Faraday effect which presents a differential polarizability in the σ^+/σ^- basis relative to a quantization axis Q *parallel* to the resonator axis. This requires an optical pumping beam which preferentially drives $\Delta m_F = 1$ transitions, a feat which is typically achieved, as in (a), using an pumping beam which propagates propagating along Q, and distinguishes between $\Delta m_F = 1$ and $\Delta m_F = -1$ transitions by its circular polarization. This proves difficult in our experiment, as our resonator mirrors preclude such a beam. We have developed a new technique, shown in (b), wherein the optical pumping beam distinguishes between $\Delta m_F = 1$ and $\Delta m_F = -1$ transitions *energetically*, via a Zeeman magnetic field B parallel to Q, and may then propagate perpendicular to the quantization axis Q.

polarized light through the atomic sample, with a propagation direction *along the quantization axis*, as shown in Fig. 6.2. The propagation direction is crucial, as we are otherwise unable to create light which polarization-selectively drives $\Delta m_F = 1$ transitions. Unfortunately, we would then have to optically pump *through the cavity*, which we cannot do, as the sample is optically thick in this direction, and the transverse modes of the resonator are non-degenerate. To circumvent this issue, one option is to optically pump in a rotating frame and wait for the instantaneous quantization axis to align itself with the optical resonator axis, as in reference [102]. For this work we have developed a new continues wave approach that does not rely upon a rotating spatial frame, but instead upon spectrally isolating $\Delta m_F = 1$ transitions from $\Delta m_F = -1$ transitions using a Zeeman field.

We apply a magnetic bias-field along the resonator axis ($\hat{x}$) of strength 14 G, and illuminate the atoms with optical pumping and re-pumping light propagating orthogonal to the resonator axis, along the transport axis ($\hat{z}$), with orthogonal linear polarization along the $\hat{y}$ axis (see Fig. 6.2). The pumping light is tuned +20 MHz above the zero field

$\left|F_g = 2\right\rangle \rightarrow |F_e = 2\rangle$ transition, making it resonant with the average $\delta m_F = 1$ Zeeman resonance, and 40 MHz detuned from the $\delta m_F = -1$ Zeeman resonance. Atoms accumulate in the "dark" $\left|F_g = 2, m_F = 2\right\rangle$ Zeeman sub-level, with only a small scattering rate induced by the off-resonant $\delta m_F = -1$ laser field. The repumping field is tuned +17 MHz from the zero-field $\left|F_g = 1\right\rangle \rightarrow |F_e = 2\rangle$ transition frequency.

6.2.3 Spectroscopy

To demonstrate the broken symmetry and the ability to isolate particular cavity mode, we probe the transmission spectrum of both forward and backward mode with $\sigma^{+(-)}$ polarizations. Fig. 6.4a shows the accessible states of the system, consisting of four cavity modes and two atomic excitations, where the $\sigma^{+(-)}$ polarized cavity modes drive atoms to the $|e^{+(-)}\rangle = |F_e = 3, m_F = 3(1)\rangle$ levels of the $5P_{3/2}$ excited state. We write the detuning of the cavity modes with helicity h from the atomic transition of polarization σ as $\Delta_{h,\sigma}$ and define the reference cavity detuning as $\Delta = \Delta_{h^+,\sigma^+}$.

In Fig. 6.4b, we experimentally explore time-reversal symmetry breaking in the cavity/probe detuning (Δ/δ_p) plane. Without the atomic ensemble, there are two pairs of degenerate empty cavity modes (diagonal dashed lines) split by 55.5 MHz due to resonator twist. Within each pair, the forward (blue) and a backward (red) modes have the same helicity but opposite polarization relative to a fixed axis. When the atoms are transported into the cavity, they break time reversal symmetry through two independent effects: first, the two light polarizations are resonant with their respective atomic transitions at frequencies that differ by 26 MHz resulting from the differential Zeeman shift of the atomic levels of the excited state; second, the two atomic transitions have substantially different coupling strengths [100], leading to different vacuum Rabi splittings for the two polarizations. The observed spectra are in good agreement with theoretical expectations shown in Fig. 6.3.

In order to reduce the loss and enhance isolation (reverse transmission suppression at the

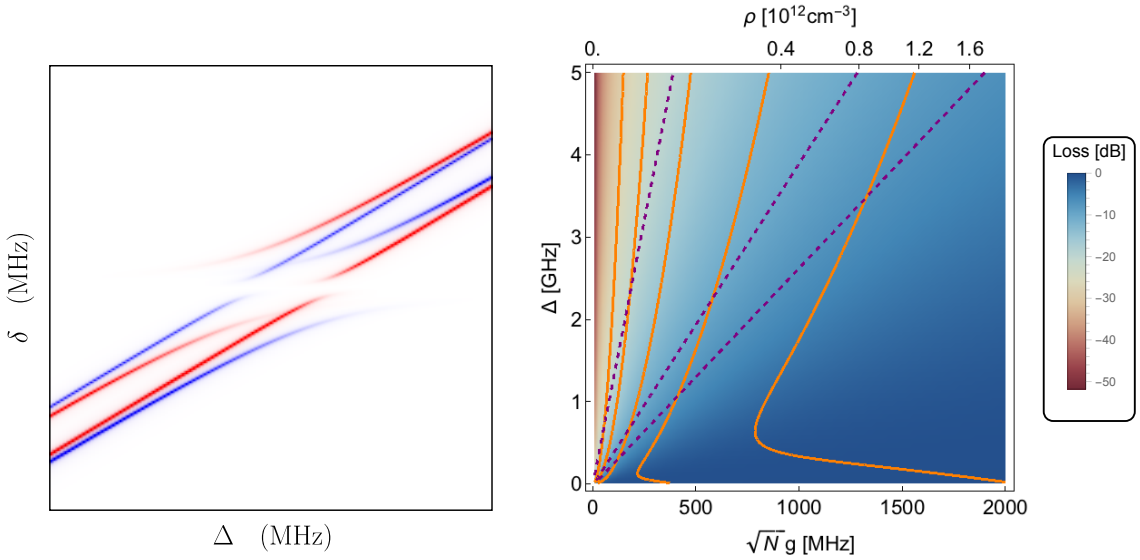

Figure 6.3: **Theory Spectrum of Time Reversal Breaking Cavity Transmission**. **(a)** The cavity transmission of forward (blue) and backward (red) modes are shown in the cavity-detuning/probe-detuning Δ/δ_p plane. When an atom ensemble is transported into the cavity waist, the cavity modes show four avoid crossings at distinct locations due to the Zeeman shift and cavity twist induced splitting. The difference in coupling strength between the two modes with the same helicity results in a splitting at large detuning, which is the source of the T-breaking mechanism. **(b)** We generate a model transmission spectrum by employing non-Hermitian perturbation theory [103], as described in [33], treating forward (blue) and backward (red) spectra separately, and injecting elliptically polarized light composed of σ^+ and σ^- polarizations, and detecting without polarization sensitivity. In practice, this means computing σ^+ and σ^- traces separately (with adjustable power to match the measured data) and then adding them together. We assume atoms are in $|F_g = 2, m_F = 2\rangle$, and that the quanziation axis is aligned with the cavity axis, and that the cavity modes themselves are circularly polarized.

forward resonance frequency), we operate the system at large detuning from $F_g = 2 \rightarrow F_e = 3$ transition (Fig. 6.4c). When $\Delta_{h,\sigma}$ is large compared with the collective light-matter single-excitation Rabi frequency $G_\sigma = \sqrt{N} g_\sigma$, the cavity resonances shift by $G_\sigma^2/\Delta_{h,\sigma}$, splitting the σ^+ and σ^- modes for a given helicity. Here g_σ is the effective single-atom vacuum Rabi coupling of the ensemble of N atoms. Splitting the forward and backward modes of a given helicity relies primarily upon the ratio $\alpha = g_{\sigma^-}/g_{\sigma^+}$ of the light-matter coupling strengths, arising from the differential polarizability of the atomic ensemble. For the states chosen above, the ratio is $\frac{1}{15}$ near the $F_g = 2 \rightarrow F_e = 3$ transition of the D_2 line, and $\frac{1}{3}$ at large detunings compared to the excited state hyperfine splitting. Meanwhile free-space scattering is substantially suppressed due to the large detuning $|\Delta_{h,\sigma}| \gg \Gamma$, where Γ is the linewidth of the excited atomic state.

In Fig. 6.4, we show the transmission spectrum with the cavity 86 MHz detuned from the Zeeman-shifted $\left|F_g = 2, m_F = 2\right\rangle \rightarrow |F_e = 3, m_F = 3\rangle$ transition. Without the atoms, respect for time-reversal symmetry is manifest in the absence of any difference between forward and backwards traces (blue and red dashed lines, respectively). With the addition of an optically pumped atomic ensemble, time-reversal symmetry is broken, as shown in the solid traces, where we observe a shift of 9.4 MHz for probing in one direction relative to the other, in agreement with $(1 - \alpha^2)\frac{G^2}{\Delta} = 13.8$ MHz from a simple first-principles theory. To demonstrate that the system behaves as a narrow-band optical isolator, we select a single isolated transmitting mode as the "forward" direction of our isolator, and measure both the reduction of transmission compared with the maximum transmission of the empty resonator, and the "reverse" transmission of the mode in the same helicity-manifold as the "worst-case" isolation. We observe an isolation of 20 dB for the backward-mode and a forward-mode transmission-reduction of only 17(1)%; the chosen detuning deviates from the theoretical optimum due to a breakdown of the approximation $G \ll \Delta$, mirror birefringence, and contributions from other excited hyperfine states.

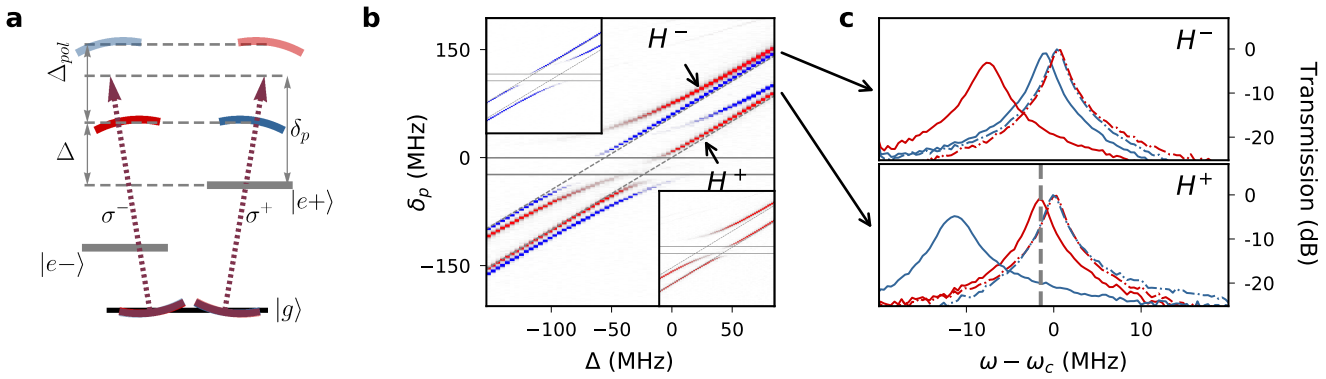

Figure 6.4: **Spectroscopy of a Time Reversal Broken Twisted Optical Resonator**. The relevant energy level is depicted in **(a)**. The four empty-cavity modes group into two helicity sub-manifolds separated by $\Delta_{pol} = 55.5$ MHz due to the cavity twisting. The dashed purple arrows show the energy of the incident probe photons which are injected in both the forward and backward directions, and have σ^- (left) and σ^+ (right) polarization components. In **(b)**, we show the cavity transmission (relative to the maximum empty-cavity transmission) versus the detuning δ_p of the probe from the σ^+ atomic transition and $\Delta = \Delta_{h^+,\sigma^+}$ of the H^+ cavity modes from the σ^+ atomic transition. With an atomic ensemble of laser cooled ^{87}Rb atoms that are optically pumped into $\left|5^2S_{1/2}, F = 2, m_F = 2\right\rangle$ state, the two forward (blue, top left inset) and two backward (red, bottom right inset) modes exhibit four avoided crossings as each becomes resonant with the appropriate atomic transition. In the far-detuned limit, the cavity-like modes show a frequency shift with little dissipation. The two modes within the same helicity manifold (upper two traces are H^-, lower two traces are H^+) split from one another due to the difference in atomic polarizability for σ^+ and σ^- polarized light on the $\left|F_g = 2, m_F = 2\right\rangle \rightarrow |F_e = 3, m_F = 1, 3\rangle$ transitions. Zoomed-in spectra at $\Delta = 86$ MHz from the Zeeman-shifted $\left|F_g = 2, m_F = 2\right\rangle \rightarrow |F_e = 3, m_F = 3\rangle$ transition for H^- (top) and H^+ (bottom) helicities are shown in **(c)**. The preservation of time-reversal symmetry for the empty cavity is manifest in the degeneracy of the two empty cavity modes propagating in opposite direction (blue and red dashed lines). The forward-σ^+ (left solid peak) and backward-σ^- (right solid peak) modes of the H^+ manifold are shifted from their bare-cavity frequencies by 11.3 MHz and 1.7 MHz, respectively, with an optical isolation (reverse transmission suppression at the forward resonance frequency) of 20.1(4) dB shown at the vertical dashed line. In the H^- manifold, the shifts are 8.1 MHz and 1.5 MHz for backward-σ^+ (left solid peak) and forward-σ^- (right solid peak) respectively. The absence of shoulders in the backward transmission spectra at the forward resonances (and vice- versa) indicates absence of backscattering.

6.2.4 Figure of Merit of the Isolator

Consider the time reversal doublet of modes $\left|F, H^+\right\rangle$,$\left|B, H^-\right\rangle$, each with a bare linewidth κ, coupled to atoms whose spontaneous linewidth is Γ and collective atom-light coupling strengths are G and αG for forward and backwards modes, respectively (for a ^{87}Rb atomic ensemble optically pumped into $\left|F_g = 2, m_F = 2\right\rangle$, $\alpha^2 = \frac{1}{3}$ for the large detunings from D_2 excited state hyperfine structure, and $\frac{1}{15}$ for detunings close to the $F_e = 3$ hyperfine feature [100]). Here we assume that the coupling strength is not detuning dependent– that is, that we are either at a small detuning compared with the hyperfine structure, or a large one, but not in-between, and similarly for the atomic fine structure. We would like to know how much the two modes may be spectrally separated by atom-induced dispersion, while maintaining at least $(1-\epsilon)$ of the empty-cavity transmission in each mode.

A detuning Δ between the cavity modes and the atomic line induces mode frequency shifts of $\frac{G^2}{\Delta}$ and $\frac{\alpha^2 G^2}{\Delta}$, neglecting the differential Zeeman shifts of the σ^+ and σ^- atomic lines; the differential resonance shift is thus $\delta_{cav} \equiv (1-\alpha^2) \times \frac{G^2}{\Delta} = (1-\alpha^2) N\eta \frac{\Gamma}{4\Delta}\kappa$, where $N\eta \equiv \frac{4G^2}{\kappa\Gamma}$ is the resonator-enhanced collective cooperativity.

The atom-induced broadening of each cavity mode is at most $\Gamma_{sc} \equiv \frac{G^2}{\Delta^2}\Gamma = N\eta\frac{\Gamma^2}{4\Delta^2}\kappa$ (assuming $\alpha \leq 1$). The reduction in resonant cavity transmission, from the empty-cavity value, is $T = \left[\frac{\kappa}{\kappa+\Gamma_{sc}}\right]^2$, and so maintaining $T \geq 1-\epsilon$ requires $\Gamma_{sc} \leq \frac{1}{2}\epsilon\kappa$.

The transmission constraint imposes a lower-limit on the atom-cavity detuning of $\Delta_{min} = \Gamma\sqrt{\frac{N\eta}{2\epsilon}}$, and thus an upper limit on the T-breaking cavity shift of $\delta_{cav}^{max} = (1-\alpha^2)\sqrt{\frac{\epsilon N\eta}{8}}\kappa$, corresponding to a suppression of backwards-mode transmission, at the frequency of the forwards-mode resonance, of approximately $\left(\frac{\kappa/2}{\delta_{cav}^{max}}\right)^2 = \frac{1}{(1-\alpha^2)^2}\frac{2}{\epsilon N\eta}$.

On the other hand, if the only quantity of interest is the *ratio* of forward transmission to backwards transmission, the optimum is different: under these circumstances, the differential shift, in linewidths, is $\beta = \frac{(1-\alpha^2)N\eta\frac{\Gamma}{4\Delta}\kappa}{\kappa+N\eta\frac{\Gamma^2}{4\Delta^2}\kappa}$, providing a transmission ratio on the forward

resonance of $R = \frac{T_f}{T_b} = \beta^2 = \left[\frac{(1-\alpha^2)N\eta\frac{\Gamma}{4\Delta}}{1+N\eta\frac{\Gamma^2}{4\Delta^2}}\right]^2$. It is apparently favorable to employ as many atoms as possible ($N\eta \to \infty$), in which case $R \to \frac{4\Delta}{\Gamma}$; thus we see that insofar as the differential cavity shift falls off only inversely with the detuning, it is favorable to go to arbitrarily large detuning. This scaling saturates at $\Delta = \Delta_{FS}$, the fine-structure splitting. At fixed optical depth $N\eta$, the optimal detuning is $\Delta = \sqrt{N\eta}\frac{\Gamma}{2}$, and the optimal ratio $\beta = \frac{1-\alpha^2}{4}\sqrt{N\eta}$.

For engineering a synthetic material, the quantity of importance is the number of *linewidths* of time-reversal symmetry breaking, as this provides the available dynamic range for interactions and single-photon physics - any interaction or single-photon process which is *larger* than the TRS-breaking can potentially scatter into the T-broken Hamiltonian manifold.

Numerical Simulation

We generate a model transmission spectrum by employing non-Hermitian perturbation theory [103], as described in [33], treating forward (blue) and backward (red) spectra separately, and injecting elliptically polarized light composed of σ^+ and σ^- polarizations, and detecting without polarization sensitivity. In practice, this means computing σ^+ and σ^- traces separately (with adjustable power to match the measured data) and then adding them together. We assume atoms are in $|F_g = 2, m_F = 2\rangle$, and that the quanziation axis is aligned with the cavity axis, and that the cavity modes themselves are circularly polarized. The resulting theory spectrum is shown in Fig. 6.3.

For cavity mode $\left|\rightarrow (\leftarrow), H^+(H^-)\right\rangle$, the coupling of the photon and atomic excited state is described by 2×2 matrices

$$H = \begin{pmatrix} \Delta + \Delta_{pol} - i\frac{\kappa}{2} & G/2 \\ G/2 & \delta_B - i\frac{\Gamma}{2} \end{pmatrix} \tag{6.1}$$

where Δ_{pol} is the splitting between different helicity manifolds generated by the cavity

twist, δ_B is the Zeemann shift of the atomic state, and $G = \sqrt{N}g$ is the collective coupling constant. For the frequency definition in this paper, we choose the detuning to be zero at $\left|F_g = 2, m_F = 2\right\rangle \rightarrow |F_e = 3, m_F = 3\rangle$ transition, and thus $\Delta_{pol} = 0$ MHz for H^+ and 55.5 MHz for H^- manifold.

Using the same method, we can calculate the loss and isolation for a time-reversal-broken resonator. Here, we propose a cavity with a finesse of 100,000 and atomic sample with RMS size of 300 μm. In Fig. 6.3, we plot the loss (density plot) in the coupling strength (atomic density)/detuning plane, and overlay the contour lines (solid orange) for -20 dB to -60 dB (left to right) isolation. With a peak atomic density of $\sim 9 \times 10^{11}$ /cm^{-3} and cavity detuning of $\sim$3.5 GHz, one can achieve an isolation of 60 dB and 80% transmission (red circle in Fig. 6.3). A high transmission (99%) and moderate isolation ($\sim$30 dB) can also be achieved with $\sqrt{N}g \approx 200$ MHz and $\Delta \approx 2.5$ GHz.

6.3 TRS Breaking for Dark Polaritons

It is now interesting to examine the impact of backscattering and TRS-breaking on Rydberg polaritons, crucial ingredients of both photonic quantum information processors and quantum materials. While Rydberg polariton collisions should be protected from backscattering by the translational symmetry of the atomic cloud, finite size and imperfect uniformity of the cloud violate this symmetry, and so it is worthwhile to explore the density of backwards propagating polariton modes, along with their character.

The linear susceptibility vanishes on EIT resonance [45], so it is natural to anticipate that the Faraday effect that we have so fruitfully exploited for TRS-breaking will also vanish on EIT resonance. We find this to be true, up to T-breaking shifts from other hyperfine states; furthermore, there is no requirement that the behavior *near* EIT resonance must respect timer reversal symmetry, and so residual TRS-breaking in EIT takes the form of different polariton properties: a change in the dark-state rotation angle and polariton loss.

The relevant transitions for the experimental investigation are depicted in Fig. 6.5a. The forward (thick) and backward (thin) modes couple to different atomic P-state magnetic sub-levels, and different Rydberg states (with different m_I); they *must* couple to the same $m_j(=\frac{1}{2})$ in the Rydberg manifold, as the large magnetic field tunes the other $m_j(=-\frac{1}{2})$ state away by many MHz. The result is that forward mode forms a closed three-level system due to the fully polarized- electron and nuclear- spins ($|F=3, m_F=3\rangle$ in the P-manifold can only couple to $\left|m_J=\frac{1}{2}, m_I=\frac{3}{2}\right\rangle$ in the Rydberg manifold), while the Rydberg state in the backward mode is coupled through the control field to other $|5P, m_F\rangle$ states which behave as loss channels and provide additional shifts and loss for the dark polariton.

Fig. 6.5b shows the experimentally observed forward (left) and backward (right) EIT spectra versus both probe frequency δ_p and resonator frequency Δ; the most prominent feature is the shift of the vacuum Rabi (bright polariton) peaks due to the atomic Faraday effect, akin to the two-level case explored in Fig. 6.5b. The dominant feature induced by the control-field coupling to the third (Rydberg) manifold is the appearance of *dark* polariton resonances for $m_J=\pm\frac{1}{2}$ Rydberg states, Zeeman shifted with respect to one another; the $m_J=\frac{1}{2}$ polariton is most visible in the forward spectrum, with the $m_J=-\frac{1}{2}$ polariton clearer in the backward spectrum. Nonetheless, as anticipated, *both* polaritons are visible in both spectra: as shown in Fig. 6.5c, there is a weak Fano-like feature in the backwards cavity spectrum near frequency of the $m_J=\frac{1}{2}$ dark polariton, resulting from the control field coupling between $\left|40S_{1/2}, m_j=1/2\right\rangle$ and $\left|5P_{3/2}, m_F=1\right\rangle$.

This Fano feature is the backward channel into which forward polaritons may scatter, and it is apparent that the backward polaritons are more weakly coupled, arising from a light-matter coupling of $G=10$ MHz (versus $G=18$ MHz in the forward direction, determined by the Clebsch-Gordon coefficients [100] and reflected in the vacuum Rabi splittings of Fig. 6.5 and a 480 nm coupling field Rabi frequency of $\Omega=4.2$ MHz (versus $\Omega=9.6$ MHz in the forward direction); this difference is visible in the width of the EIT windows, manifested

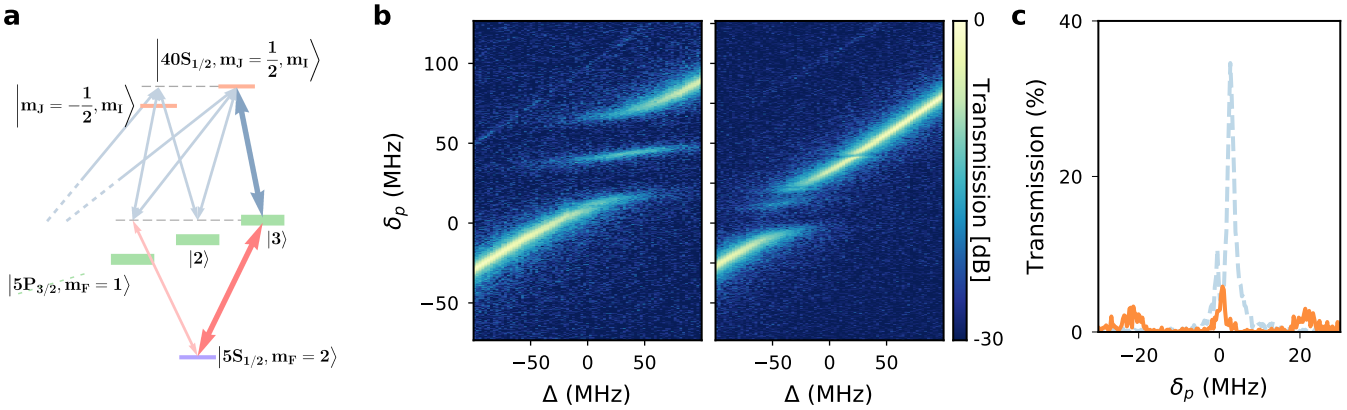

Figure 6.5: **Time Reversal Breaking in Cavity Rydberg EIT**. (a) The atomic level structure and relevant atomic transitions for cavity Rydberg Electromagnetically Induced Transparency. An ensemble of optically pumped ^{87}Rb atoms are coupled to the cavity modes on the $5S_{1/2} \leftrightarrow 5P_{3/2}$ transition in the presence of a control field which further couples the atoms to the $4S$ Rydberg manifold. The small hyperfine structure <MHz of the Rydberg manifold places it in the Paschen-Back regime (with m_J a good quantum number), while the ground- and P-state manifolds, with their larger hyperfine structure of $\sim$ 6.8GHz and $\sim$ 500MHz respectively [100], reside in the Zeeman regime (with m_F a good quantum number). In the forward mode, both electron and nuclei spins are polarized so only stretched states couplings are allowed, and the system forms a standard 3-level EIT diagram. The backward mode is more complicated due to the non vanishing coupling between $40S, m_J = 1/2 \leftrightarrow 5P_{3/2}, F = 3, m_F = 0, 1, 2$ P-states with only $m_F = 1$ strongly coupled to the cavity field. (b) Normalized cavity transmission vs probe (δ_p) and cavity (Δ) detunings. When the cavity is on resonance with the σ^+ mode, probing in the forward direction (left panel) reveals a standard EIT spectrum [104]; probing backwards reveals only a weak Fano feature for this cavity tuning. The coupling of the backwards cavity field to the $m_J = -1/2$ Rydberg manifold is apparent from the prominent Zeeman shifted EIT feature in that spectrum, and the corresponding Fano feature in the forward spectrum. A slice at $\Delta = 0$ is shown in (c), exhibiting vacuum Rabi splittings and an EIT feature in the forward spectrum (orange solid), and only a single Fano resonance in the reverse spectrum (blue dashed).

as the cavity detuning range over which the EIT and Fano features persist: 40 MHz in the forward direction, and 10 MHz in the backward direction.

REFERENCES

1. Birnbaum, K. M. *et al.* Photon blockade in an optical cavity with one trapped atom. *Nature* **436,** 87–90 (2005).

2. Hartmann, M. J., Brandao, F. G. & Plenio, M. B. Strongly interacting polaritons in coupled arrays of cavities. *Nature Physics* **2,** 849–855 (2006).

3. Greentree, A. D., Tahan, C., Cole, J. H. & Hollenberg, L. C. Quantum phase transitions of light. *Nature Physics* **2,** 856–861 (2006).

4. Angelakis, D. G., Santos, M. F. & Bose, S. Photon-blockade-induced Mott transitions and X Y spin models in coupled cavity arrays. *Physical Review A* **76,** 031805 (2007).

5. Hartmann, M. J., Brandao, F. G. & Plenio, M. B. Quantum many-body phenomena in coupled cavity arrays. *Laser & Photonics Reviews* **2,** 527–556 (2008).

6. Guerlin, C., Brion, E., Esslinger, T. & Mølmer, K. Cavity quantum electrodynamics with a Rydberg-blocked atomic ensemble. *Phys. Rev. A* **82,** 053832 (2010).

7. Georgakopoulos, A., Sommer, A. & Simon, J. Theory of Interacting Cavity Rydberg Polaritons. *arXiv preprint arXiv:1805.07315* (2018).

8. Balili, R., Hartwell, V., Snoke, D., Pfeiffer, L. & West, K. Bose-Einstein Condensation of Microcavity Polaritons in a Trap. en. *Science* **316,** 1007–1010. ISSN: 0036-8075, 1095-9203 (2007).

9. Deng, H., Haug, H. & Yamamoto, Y. Exciton-polariton Bose-Einstein condensation. *Rev. Mod. Phys.* **82,** 1489–1537 (2010).

10. Carusotto, I. & Ciuti, C. Quantum fluids of light. *Rev. Mod. Phys.* **85,** 299–366 (2013).

11. Chou, C. W., Polyakov, S. V., Kuzmich, A. & Kimble, H. J. Single-photon generation from stored excitation in an atomic ensemble. *Phys. Rev. Lett.* **92,** 213601 (2004).

12. Chaneliere, T. *et al.* Storage and retrieval of single photons transmitted between remote quantum memories. *Nature* **438,** 833–836 (2005).

13. Simon, J., Tanji, H., Thompson, J. K. & Vuletić, V. Interfacing Collective Atomic Excitations and Single Photons. *Phys. Rev. Lett.* **98,** 183601 (2007).

14. Akimov, A. *et al.* Generation of single optical plasmons in metallic nanowires coupled to quantum dots. *Nature* **450,** 402–406 (2007).

15. Lukin, M. D. *et al.* Dipole Blockade and Quantum Information Processing in Mesoscopic Atomic Ensembles. *Physical Review Letters* **87,** 037901 (2001).

16. Lukin, M. D. Colloquium : Trapping and manipulating photon states in atomic ensembles. *Reviews of Modern Physics* **75,** 457–472 (2003).

17. Pritchard, J. D. *et al.* Cooperative Atom-Light Interaction in a Blockaded Rydberg Ensemble. *Phys. Rev. Lett.* **105,** 193603 (2010).

18. Gorshkov, A. V., Otterbach, J., Fleischhauer, M., Pohl, T. & Lukin, M. D. Photon-Photon Interactions via Rydberg Blockade. *Physical Review Letters* **107,** 133602 (2011).

19. Peyronel, T. *et al.* Quantum nonlinear optics with single photons enabled by strongly interacting atoms. *Nature* **488,** 57–60 (2012).

20. Parigi, V. *et al.* Observation and Measurement of Interaction-Induced Dispersive Optical Nonlinearities in an Ensemble of Cold Rydberg Atoms. *Phys. Rev. Lett.* **109,** 233602 (2012).

21. Stanojevic, J., Parigi, V., Bimbard, E., Ourjoumtsev, A. & Grangier, P. Dispersive optical nonlinearities in a Rydberg electromagnetically-induced-transparency medium. *Phys. Rev. A* **88,** 053845 (2013).

22. Maxwell, D. *et al.* Storage and Control of Optical Photons Using Rydberg Polaritons. *Phys. Rev. Lett.* **110** (2013).

23. Hofmann, C. S. *et al.* Sub-Poissonian Statistics of Rydberg-Interacting Dark-State Polaritons. *Phys. Rev. Lett.* **110,** 203601 (2013).

24. Firstenberg, O. *et al.* Attractive photons in a quantum nonlinear medium. *Nature* **502,** 71–75 (2013).

25. Bienias, P. *et al.* Scattering resonances and bound states for strongly interacting Rydberg polaritons. *Phys. Rev. A* **90,** 053804 (2014).

26. Gorniaczyk, H., Tresp, C., Schmidt, J., Fedder, H. & Hofferberth, S. Single-Photon Transistor Mediated by Interstate Rydberg Interactions. *Phys. Rev. Lett.* **113,** 053601 (2014).

27. Baur, S., Tiarks, D., Rempe, G. & Dürr, S. Single-Photon Switch Based on Rydberg Blockade. *Phys. Rev. Lett.* **112,** 073901 (2014).

28. Tiarks, D., Baur, S., Schneider, K., Dürr, S. & Rempe, G. Single-Photon Transistor Using a Förster Resonance. *Phys. Rev. Lett.* **113,** 053602 (2014).

29. Duan, L.-M., Lukin, M. D., Cirac, J. I. & Zoller, P. Long-distance quantum communication with atomic ensembles and linear optics. *Nature* **414,** 413–418. ISSN: 0028-0836 (2001).

30. Boddeda, R. *et al.* Rydberg-induced optical nonlinearities from a cold atomic ensemble trapped inside a cavity. *arXiv:1512.08480 [cond-mat, physics:physics, physics:quant-ph].* arXiv: 1512.08480. (2015) (2015).

31. Sommer, A. & Simon, J. Engineering Photonic Floquet Hamiltonians through Fabry Pérot Resonators. *arXiv:1511.00595 [cond-mat, physics:physics, physics:quant-ph].* (2015) (2015).

32. Klaers, J., Schmitt, J., Vewinger, F. & Weitz, M. Bose-Einstein condensation of photons in an optical microcavity. *Nature* **468,** 545–548 (2010).

33. Sommer, A., Büchler, H. P. & Simon, J. Quantum Crystals and Laughlin Droplets of Cavity Rydberg Polaritons. *arXiv:1506.00341 [cond-mat.quant-gas]* (2015).

34. Chang, D. E. *et al.* Crystallization of strongly interacting photons in a nonlinear optical fibre. en. *Nature Phys.* **4,** 884–889. ISSN: 1745-2473 (2008).

35. Gopalakrishnan, S., Lev, B. L. & Goldbart, P. M. Emergent crystallinity and frustration with Bose-Einstein condensates in multimode cavities. *Nature Phys.* **5,** 845–850 (2009).

36. Otterbach, J., Moos, M., Muth, D. & Fleischhauer, M. Wigner Crystallization of Single Photons in Cold Rydberg Ensembles. *Phys. Rev. Lett.* **111,** 113001 (2013).

37. Kollár, A. J., Papageorge, A. T., Baumann, K., Armen, M. A. & Lev, B. L. An adjustable-length cavity and Bose-Einstein condensate apparatus for multimode cavity QED. *New. J Phys.* **17,** 043012 (2015).

38. Schine, N., Ryou, A., Gromov, A., Sommer, A. & Simon, J. Synthetic Landau levels for photons. *arXiv:1511.07381 [cond-mat.quant-gas].* (2015) (2015).

39. Hafezi, M., Lukin, M. D. & Taylor, J. M. Non-equilibrium fractional quantum Hall state of light. *New J. Phys.* **15,** 063001 (2013).

40. Maghrebi, M. F. *et al.* Fractional quantum Hall states of Rydberg polaritons. *Phys. Rev. A* **91,** 033838 (2015).

41. Grusdt, F. & Fleischhauer, M. Fractional quantum Hall physics with ultracold Rydberg gases in artificial gauge fields. *Phys. Rev. A* **87,** 043628 (2013).

42. Umucalılar, R. O., Wouters, M. & Carusotto, I. Probing few-particle Laughlin states of photons via correlation measurements. *Phys. Rev. A* **89,** 023803 (2014).

43. Ningyuan, J. *et al.* Observation and characterization of cavity Rydberg polaritons. *Physical Review A* **93,** 041802 (2016).

44. Simon, J., Tanji, H., Thompson, J. K. & Vuletić, V. Interfacing collective atomic excitations and single photons. *Physical review letters* **98,** 183601 (2007).

45. Fleischhauer, M. & Lukin, M. D. Dark-State Polaritons in Electromagnetically Induced Transparency. *Phys. Rev. Lett.* **84,** 5094–5097 (2000).

46. Lukin, M. D., Fleischhauer, M., Scully, M. O. & Velichansky, V. L. Intracavity electromagnetically induced transparency. en. *Opt. Lett* **23,** 295. ISSN: 0146-9592, 1539-4794 (1998).

47. Hernandez, G., Zhang, J. & Zhu, Y. Vacuum Rabi splitting and intracavity dark state in a cavity-atom system. *Physical Review A* **76,** 053814 (2007).

48. Honer, J., Löw, R., Weimer, H., Pfau, T. & Büchler, H. P. Artificial Atoms Can Do More Than Atoms: Deterministic Single Photon Subtraction from Arbitrary Light Fields. *Phys. Rev. Lett.* **107,** 093601 (2011).

49. Yuan, Z.-S. *et al.* Experimental demonstration of a BDCZ quantum repeater node. *Nature* **454,** 1098–1101. ISSN: 0028-0836 (2008).

50. Grodecka-Grad, A., Zeuthen, E. & Sørensen, A. S. High-Capacity Spatial Multimode Quantum Memories Based on Atomic Ensembles. *Phys. Rev. Lett.* **109,** 133601 (2012).

51. Gorshkov, A. V., Otterbach, J., Fleischhauer, M., Pohl, T. & Lukin, M. D. Photon-photon interactions via Rydberg blockade. *Physical review letters* **107,** 133602 (2011).

52. Jia, N. *et al.* A Strongly Interacting Polaritonic Quantum Dot. *arXiv preprint arXiv:1705.07475* (2017).

53. Sommer, A., Büchler, H. P. & Simon, J. Quantum Crystals and Laughlin Droplets of Cavity Rydberg Polaritons. *arXiv preprint arXiv:1506.00341* (2015).

54. Shore, B. W. & Knight, P. L. The jaynes-cummings model. *Journal of Modern Optics* **40,** 1195–1238 (1993).

55. Verger, A., Ciuti, C. & Carusotto, I. Polariton quantum blockade in a photonic dot. *Physical Review B* **73,** 193306 (2006).

56. Günter, G. *et al.* Interaction enhanced imaging of individual Rydberg atoms in dense gases. *Physical review letters* **108,** 013002 (2012).

57. Kleckner, D. & Irvine, W. T. M. Creation and dynamics of knotted vortices. *Nat Phys* **9,** 253–258. ISSN: 1745-2473 (Apr. 2013).

58. Ikegami, H., Tsutsumi, Y. & Kono, K. Chiral Symmetry Breaking in Superfluid 3He-A. *Sci.* **341,** 59–62 (July 2013).

59. Wilczek, F. Quantum Mechanics of Fractional-Spin Particles. *Phys. Rev. Lett.* **49,** 957–959 (Oct. 1982).

60. Kitaev, A. Y. Unpaired Majorana fermions in quantum wires. *Physics-Uspekhi* **44,** 131 (2001).

61. Fu, L. & Kane, C. Superconducting Proximity Effect and Majorana Fermions at the Surface of a Topological Insulator. *Phys. Rev. Lett.* **100,** 96407 (Mar. 2008).

62. Arovas, D., Schrieffer, J. & Wilczek, F. Fractional Statistics and the Quantum Hall Effect. *Phys. Rev. Lett.* **53,** 722–723 (Aug. 1984).

63. Lin, Y. J., Compton, R. L., Jiménez-García, K., Porto, J. V. & Spielman, I. B. Synthetic magnetic fields for ultracold neutral atoms. en. *Nature* **462,** 628–632 (2009).

64. Beeler, M. C. *et al.* The spin Hall effect in a quantum gas. *Nature* **498,** 201–204. ISSN: 0028-0836 (June 2013).

65. Wang, P. *et al.* Spin-Orbit Coupled Degenerate Fermi Gases. *Phys. Rev. Lett.* **109,** 95301 (Aug. 2012).

66. Cheuk, L. *et al.* Spin-Injection Spectroscopy of a Spin-Orbit Coupled Fermi Gas. *Phys. Rev. Lett.* **109,** 95302 (Aug. 2012).

67. Cooper, N. Optical Flux Lattices for Ultracold Atomic Gases. *Phys. Rev. Lett.* **106,** 175301 (Apr. 2011).

68. Miyake, H., Siviloglou, G. A., Kennedy, C. J., Burton, W. C. & Ketterle, W. Realizing the Harper Hamiltonian with Laser-Assisted Tunneling in Optical Lattices. *Phys. Rev. Lett.* **111.** doi:10.1103/PhysRevLett.111.185302. http://link.aps.org/doi/10.1103/PhysRevLett.111.185302%20http://journals.aps.org/prl/abstract/10.1103/PhysRevLett.111.185302 (2013).

69. Aidelsburger, M. *et al.* Experimental Realization of Strong Effective Magnetic Fields in an Optical Lattice. *Phys. Rev. Lett.* **107,** 255301 (Dec. 2011).

70. Wang, Z., Chong, Y. D., Joannopoulos, J. D. & Soljačić, M. Reflection-Free One-Way Edge Modes in a Gyromagnetic Photonic Crystal. *Phys. Rev. Lett.* **100.** doi:10.1103/PhysRevLett.100.013905. http://link.aps.org/doi/10.1103/PhysRevLett.100.013905 (2008).

71. Wang, Z., Chong, Y., Joannopoulos, J. D. & Soljacic, M. Observation of unidirectional backscattering-immune topological electromagnetic states. *Nature* **461,** 772–775. ISSN: 0028-0836 (Oct. 2009).

72. Umucal\ifmmode \imath \else \i \filar, R. O. & Carusotto, I. Artificial gauge field for photons in coupled cavity arrays. *Phys. Rev. A* **84,** 43804 (Oct. 2011).

73. Haldane, F. & Raghu, S. Possible Realization of Directional Optical Waveguides in Photonic Crystals with Broken Time-Reversal Symmetry. *Phys. Rev. Lett.* **100,** 13904 (Jan. 2008).

74. Rechtsman, M. C. *et al.* Photonic Floquet topological insulators. *Nature* **496,** 196–200 (2013).

75. Hafezi, M., Demler, E. A., Lukin, M. D. & Taylor, J. M. Robust optical delay lines with topological protection. *Nat Phys* **7,** 907–912. ISSN: 1745-2473 (Nov. 2011).

76. Hafezi, M., Mittal, S., Fan, J., Migdall, A. & Taylor, J. M. Imaging topological edge states in silicon photonics. en. *Nat. Photonics* **7,** 1001–1005 (2013).

77. Khanikaev, A. B. *et al.* Photonic topological insulators. *Nat Mater* **12,** 233–239. ISSN: 1476-1122 (Mar. 2013).

78. Koch, J., Houck, A., Hur, K. L. & Girvin, S. Time-reversal-symmetry breaking in circuit-QED-based photon lattices. *Phys. Rev. A* **82,** 1–18. ISSN: 1050-2947 (Oct. 2010).

79. Mittal, S. *et al.* Topologically Robust Transport of Photons in a Synthetic Gauge Field. *Phys. Rev. Lett.* **113,** 87403 (Aug. 2014).

80. Jotzu, G. *et al.* Experimental realization of the topological Haldane model with ultracold fermions. *Nature* **515,** 237–240. ISSN: 0028-0836 (Nov. 2014).

81. Aidelsburger, M. *et al.* Realization of the Hofstadter Hamiltonian with Ultracold Atoms in Optical Lattices. *Phys. Rev. Lett.* **111.** doi:10.1103/PhysRevLett.111.185301. http://link.aps.org/doi/10.1103/PhysRevLett.111.185301%20http://journals.aps.org/prl/abstract/10.1103/PhysRevLett.111.185301 (2013).

82. Rechtsman, M. C. *et al.* Strain-induced pseudomagnetic field and photonic Landau levels in dielectric structures. *Nat Phot.* **7,** 153–158. ISSN: 1749-4885 (Feb. 2013).

83. Kitagawa, T., Berg, E., Rudner, M. & Demler, E. Topological characterization of periodically driven quantum systems. *Phys. Rev. B* **82.** doi:10.1103/PhysRevB.82.235114. http://link.aps.org/doi/10.1103/PhysRevB.82.235114%20http://journals.aps.org/prb/abstract/10.1103/PhysRevB.82.235114 (2010).

84. Lindner, N. H., Refael, G. & Galitski, V. Floquet topological insulator in semiconductor quantum wells. en. *Nat. Phys.* **7,** 490–495 (2011).

85. Schroer M.\, D. *et al.* Measuring a Topological Transition in an Artificial Spin-1/2 System. *Phys. Rev. Lett.* **113,** 50402 (July 2014).

86. Roushan, P. *et al.* Observation of topological transitions in interacting quantum circuits. *arXiv:1407.1585 [quant-ph].* http://arxiv.org/abs/1407.1585 (2014).

87. Hu, W. *et al.* Measurement of a Topological Edge Invariant in a Microwave Network. *Phys. Rev. X* **5,** 11012 (Feb. 2015).

88. Wallraff, a. *et al.* Strong coupling of a single photon to a superconducting qubit using circuit quantum electrodynamics. *Nature* **431,** 162–7. ISSN: 1476-4687 (Sept. 2004).

89. Ningyuan, J., Sommer, A., Schuster, D. & Simon, J. Time Reversal Invariant Topologically Insulating Circuits. *arXiv:1309.0878 [cond-mat.mes-hall]* (2013).

90. Hofstadter, D. R. Energy levels and wave functions of Bloch electrons in rational and irrational magnetic fields. *Phys. Rev. B* **14,** 2239–2249 (1976).

91. Jotzu, G. *et al.* Experimental realisation of the topological Haldane model. *arXiv:1406.7874 [cond-mat, physics:quant-ph].* http://arxiv.org/abs/1406.7874 (2014).

92. Wang, Y. H., Steinberg, H., Jarillo-Herrero, P. & Gedik, N. Observation of Floquet-Bloch States on the Surface of a Topological Insulator. en. *Science (80-.).* **342,** 453–457 (2013).

93. Shankar, R. *Principles of Quantum Mechanics* 1994. Corr. English, 700. ISBN: 9780306447907. http://www.amazon.co.uk/Principles-Quantum-Mechanics-R-Shankar/dp/0306447908 (Springer, New York, 2008).

94. Caloz, C. & Itoh, T. Transmission line approach of left-handed (LH) materials and microstrip implementation of an artificial LH transmission line. *IEEE Trans. Antennas Propag.* **52,** 1159–1166 (2004).

95. Hasan, M. & Kane, C. Topological insulators. *Rev. Mod. Phys.* **82,** 3045–3067 (2010).

96. Kane, C. L. & Mele, E. J. Quantum Spin Hall Effect in Graphene. *Phys. Rev. Lett.* **95,** 226801 (Nov. 2005).

97. Nakada, K., Fujita, M., Dresselhaus, G. & Dresselhaus, M. S. Edge state in graphene ribbons: Nanometer size effect and edge shape dependence. *Phys. Rev. B* **54,** 17954–17961 (24 Dec. 1996).

98. Jia, N. *et al.* Photons and polaritons in a broken-time-reversal nonplanar resonator. *Physical Review A* **97,** 013802 (2018).

99. Sommer, A. & Simon, J. Engineering photonic Floquet Hamiltonians through Fabry-Pérot resonators. *New Journal of Physics* **18,** 35008. ISSN: 13672630 (2016).

100. Steck, D. A. *Rubidium 87 D line data* 2001. http://www.steck.us/alkalidata/rubidium87numbers.pdf.

101. Tanji-Suzuki, H. *et al. Interaction between Atomic Ensembles and Optical Resonators: Classical Description* Nov. 2011. arXiv: 1104.3594. http://arxiv.org/abs/1104.3594.

102. Tanji, H., Ghosh, S., Simon, J., Bloom, B. & Vuletić, V. Heralded single-magnon quantum memory for photon polarization states. *Physical review letters* **103,** 043601 (2009).

103. Cohen-Tannoudji, Claude, Dupont-Roc, Jacques & Grynberg, Gilbert. *Atom - Photon Interactions: Basic Processes and Applications* (Wiley, 2004).

104. Ningyuan, J. *et al.* Observation and characterization of cavity Rydberg polaritons. *Phys. Rev. A* **93,** 041802 (4 Apr. 2016).